UNIVERSITAT POLITÈCNICA DE CATALUNYA
BARCELONA**TECH**
UPC

**Departament de Teoria del Senyal
i Comunicacions**

Orbital Differential SAR Interferometry with Polarimetric Data

Author
Dani Monells Miralles

Thesis Advisor
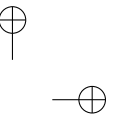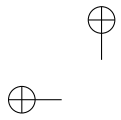## Jordi J. Mallorqui Franquet

Thesis written by Dani Monells Miralles

Orbital Differential SAR Interferometry with Polarimetric Data

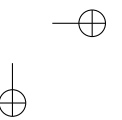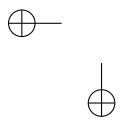Ph.D. program on Signal Theory and Communications

I am the eye in the sky
Looking at you
I can read your mind

The Alan Parsons Project

ABSTRACT

Space-borne Synthetic Aperture Radar (SAR) systems have demonstrated great effectiveness to survey wide areas, independently of the weather conditions and the day/night cycle. One of the most exploited applications is Differential SAR Interferometry (DInSAR), and by extension, advanced multi-temporal techniques addressed as Persistent Scatterers Interferometry (PSI). These techniques provide the means to retrieve the displacement on the observed terrain surface. Taking advantage of the high coverage provided by this technology, natural and human induced phenomena may be monitored and detected in order to avoid and prevent hazardous or even catastrophic situations.

A good characterization of such events is often related to the density and quality of the information delivered. In many cases, the success in the interpretation of localized surface motion phenomena relies on having as much measurements as possible. Conventional insitu techniques, when used properly, are able to provide reliable measurements. However, they are limited to their localization, and deploy a high number of instruments is not cost effective.

The good characterization provided by PSI measurements is limited by the acquisition parameters. SAR images sensitivity over the scene depends strongly on the geometric shape and distribution of targets. Historically, satellite SAR sensors had single polarimetric capabilities, so sensitivity over the scene was restricted to a certain antenna configuration. On the contrary, polarimetric acquisitions emit an receive with different antenna configurations, providing sensitivity to different geometries in the scenario. The launch in these later years of several satellites with polarimetric capabilities has triggered its use in several fields of application.

The objective of this thesis is to evaluate the use of Polarimetric SAR (PolSAR) data for its application in the DInSAR framework. The extra information contained in PolSAR datasets is bound to improve the effectiveness of PSI techniques. Obtaining a higher density and quality of motion measurements will ease the detection and interpretation of terrain displacement phenomena.

ACKNOWLEDGEMENTS

Contents

1

CHAPTER 1

INTRODUCTION

1.1   Motivation

During the late twentieth century, the environment and specially the human impact on it have grown to a major concern. Then, monitoring and control of the events taking place inside and even outside of our planet have become a necessary and popular activity. The fast evolution of technology during this later period of mankind has allowed for the appearance of a myriad range of devices and techniques able to carry out this monitoring.

In this context, the main framework of this thesis lies on the so-called *Remote Sensing* field. From its strict definition, this concept comprises any kind of measurement which avoids direct physical contact with the scene under monitoring. This is generally done through any kind of propagated signal, usually electromagnetic radiation. The emitted energy interacts with the scene, or even the proper scene emits its own radiation, and this energy is recovered afterwards for its analysis. The electromagnetic energy emission

source divides Remote Sensing into two main disciplines:

- **_Passive Remote Sensing_:** Electromagnetic energy comes from natural sources. A typical example is the electromagnetic radiation coming from the Sun. This also includes the self emission of energy by the scene under monitoring.

- **_Active Remote Sensing_:** Electromagnetic energy is self generated by an artificial device, which illuminates the scene to retrieve its backscattering.

This thesis focuses on the latter case, in particular on an advanced radar system known as Synthetic Aperture Radar (SAR). These instruments have many interesting capabilities for its application in Remote Sensing. They are characterized to operate on moving platforms, so usual deployments are:

- **_Ground-based_:** The platform is a rail or similar, anchored on the ground, where the instrument moves along. These kind of deployments have a restricted coverage but are extremely versatile in terms of measurement schedule. For instance, they allow continuous monitoring.

- **_Airborne_:** The platform is any flying vehicle, for instance a plane or helicopter. The coverage in this case is better and it is still versatile, but the operative costs increases drastically.

- **_Orbital_:** The platform is a satellite in orbit. This option lacks of the versatility provided by the former ones, but it provides the better coverage and it is a quite cost effective solution.

These last years have seen the launch of many spatial missions including a SAR system as a payload. This fact has triggered the development of many techniques which allow for the monitoring of the status of the Earth surface. Information retrieved by these sensors has proven to be very useful in a wide range of applications, such as disaster monitoring, land cover classification, risk management, and many more. The specific framework of this thesis is focused on the exploitation of orbital SAR data-sets.

One of the first and most relevant applications for SAR imaging is SAR Interferometry (InSAR), able to retrieve the topography of a scene from two SAR images taken from slightly different positions [1, 2]. Many Digital Elevation Model (DEM) archives are generated with this technique, such as the Shuttle Radar Topographic Mission (SRTM) database [3] or more recently, the database retrieved by the TanDEM-X mission [4].

The key orbital SAR application is undoubtedly Differential SAR Interferometry (DInSAR). This technique is able to measure terrain displacement between two acquisitions taken at different times. It reaches its highest potential when applied along with multi-temporal data-sets, addressed then as Persistent Scatterers Interferometry (PSI), able to retrieve motion evolution with millimetric sensitivity. Along with the high coverage provided or-

Satellite	Ownership	Pol. mode	Band	Life span
Envisat	ESA	Dual-pol	C	2002 - 2012
ALOS	JAXA	Quad-Pol	L	2006 - 2011
TerraSAR-X	DLR/EADS Astrium	Dual-Pol	X	2007 - present
Radarsat-2	CSA	Quad-Pol	C	2007 - present
Cosmo-Skymed	ASI	Dual-Pol	X	2007 - present
TanDEM-X	DLR/EADS Astrium	Dual-Pol	X	2010 - present
Sentinel-1A	ESA	Dual-Pol	C	2014 - present
ALOS-2	JAXA	Quad-Pol	L	2014 - present
Sentinel-1B	ESA	Dual-Pol	C	2016 - present
PAZ	HisdeSAT	Dual-Pol	X	Launch unknown
Radarsat constellation	CSA	Quad-Pol	C	Launch in 2018

Table 1.1: Past, present and future of polarimetric satellites, in launch order.

bital SAR deployments, it becomes an excellent tool for the precise monitoring of wide areas of terrain with high spatial resolution.

Another interesting SAR discipline is the so-called SAR Polarimetry. It deals with the study of the polarimetric state of the electromagnetic waves retrieved after its interaction with the monitored scene. Interaction is done by emitting and receiving electromagnetic waves in different polarimetric configurations. This generates an upgraded source of SAR information known as Polarimetric SAR (PolSAR) data.

PolSAR acquisitions consist of several conventional SAR acquisitions, usually addressed as channels. Since different polarimetric configurations are used, each channel is sensitive to different characteristics of the scene. This additional redundancy over the scene may allow to increase both quality and density of the measurements.

Historically, SAR sensors on-board satellites had only single-polarimetric capabilities, i.e., emitting with only one polarimetric state. However, since the beginning of the 21st century several orbital SAR missions with polarimetric capabilities have become a reality. Table 1.1 and Fig. 1.1 summarize the history of all SAR satellites. Note that since 2002, PolSAR data-sets have been generated without interruption. Moreover, they are operating at different frequency bands, which allows to analyze and exploit many kinds of land cover.

The access to this consistent PolSAR data-set has triggered the development of many techniques in the SAR Polarimetry field: Change detection, classification, biomass estimation, and many more. The main objective of this thesis is to study the benefits of PolSAR data over the single polarimetric one for orbital PSI analysis.
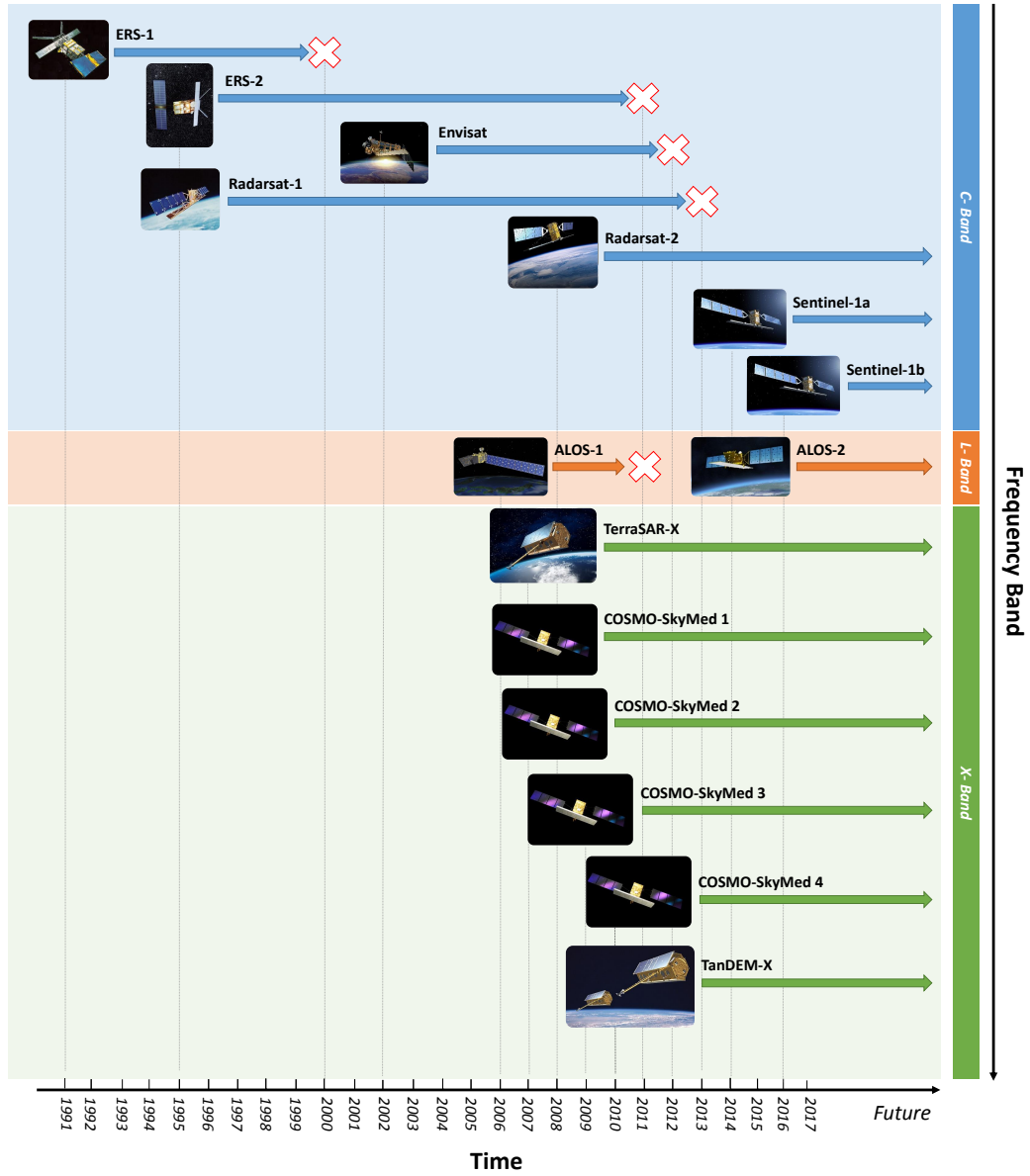
Figure 1.1: Main SAR sensors timeline. Form 2002 onwards, they all present polarimetric capabilities.

1.2   Objectives of the thesis

The main objective of this thesis, as stated in the motivation, is to assess the benefits of PolSAR data for its use in PSI, in the specific case of orbital acquisitions. In the following, a detailed enumeration of all the specific objectives is listed.

- Review SAR, InSAR, DInSAR, PSI and SAR Polarimetry to provide the theoretical basis of the thesis framework.

- Study combination strategies of PSI measurements obtained from each polarimetric channel.

- Review and establish the necessary theoretical framework on phase quality optimization, for its specific use in a PSI analysis.

- Analyze the performance and viability of phase quality optimization, comparing the PSI results from single polatrimetric channels and the optimized ones.

- Asses the comparison between fully and dual polarimetric data, in the specific case of phase quality optimization.

- Corroborate the actual improvement in quality of the phase after the optimization to asses its effectiveness.

- Analyze the implications of polarimetric transformations and its physical meaning.

Obviously, an improvement in the PSI measurements obtained from the use of PolSAR acquisitions is expected. Specifically, the final objectives in terms of performance and capabilities are to:

- Increase the final density of PSI measurement points, to provide a better characterization of the phenomena under monitoring.

- Increase the overall quality of measurements, to improve the precision in the detection of motion events.

- Detect more than one scatterer inside the same resolution cell, thanks to the different sensitivities over the scene using PolSAR data-sets. This will allow to distinguish different motion behaviors in different targets.

1.3 Structure of the thesis

The objectives established are addressed in the following structure. The document is divided into 6 main chapters, which are enumerated in the following:

1. The present chapter, **Chapter 1**, consists of the thesis introduction. It includes the motivation for the work done, as well as the list of objectives and the present structure.

2. **Chapter 2** provides the general theoretical for the understanding of this thesis. It first reviews the basics in SAR processing and characteristics, in particular for the orbital deployment. Then, the description of the basic SAR applications, InSAR and DInSAR are presented. As a consequence, the advanced PSI techniques are put forward. Finally, some basics in SAR Polarimetry are included.

3. **Chapter 3** presents the PolSAR data-set acquired by Radarsat-2, a fully polarimetric satellite, over the city of Barcelona in Spain and used during this thesis. The main areas of interest are described, along with the technical characteristics of the data.

4. **Chapter 4** is devoted to the first approach of PolSAR data exploitation proposed in this thesis. It focuses on applying the PSI analysis to each polarimetric channel and consider different combination strategies of the final measurements. Also, results over some areas described in Chapter 3 are presented and discussed.

5. **Chapter 5** may be considered the core chapter of this thesis. It describes the phase quality optimization approach applied to the PSI analysis. Several criteria are proposed and tested, in order to asses the benefits and performances of each. The application on this criteria is tested using two well known phase quality estimators: the coherence stability and the amplitude dispersion. This chapter presents also results obtained in the areas of interest described in Chapter 3. Finally, a comparison with dual an fully polarimetric data-sets is carried out, in terms of phase quality optimization.

6. **Chapter 6** is devoted to analyze more in detail the implications, benefits and possible drawbacks of the use of phase quality optimization in a PSI analysis. Several examples of its performance are shown and discussed.

7. **Appendix A**: This appendix is devoted to further analyze the results obtained in chapter 5, to provide the wider view of the performance in additional areas of interest.

2

Theoretical basis

I N this chapter, the basic concepts about the system and the techniques used and developed in this thesis are described. It will be divided as follows:

- **Orbital SAR**: Description of the basic properties of the acquisition system, such as geometry, pre-processing and data characteristics.

- **SAR Interferometry and Differential SAR Interferometry**: Review of the techniques for topography and displacement retrieval, to highlight the fundamental basis of this thesis.

- **Persistent Scatterers Interferometry**: Description of the advanced techniques to retrieve the temporal evolution of displacement phenomena.

- **SAR Polarimetry**: Basic concepts in order to understand the treatment of PolSAR data in the framework of PSI carried out in this thesis.

2.1 Orbital SAR

A SAR is an active and coherent microwave radar system. As any radar instrument, it emits an electromagnetic pulse which interacts with the illuminated scene. Then, the back-scattered signal produced is retrieved by the system in order to be analyzed.

SAR systems have demonstrated to be a great asset in the remote sensing field, due to its suitable characteristics. In particular, when on orbital platforms, they stand out for several reasons:

- **Independent of the day/night cycle:** As an active system, since it emits its own energy, does not need any further source of radiation to operate.

- **Minimal impact of meteorologic artifacts:** Since the frequencies of operation are in the microwave spectrum, it is possible to go through atmospheric artifacts, such as clouds or rain.

- **Wide area coverage:** The orbital deployment allows to monitor a wide extension of terrain over the Earth.

- **Long term monitoring:** Considering the duration of past orbital missions, the life span of a satellite is of several years.

- **High spatial resolution:** As it will be described in the following, SAR satellites are able to provide much higher resolution than conventional radars.

The following sections describe the principal characteristics of a SAR system, focusing on the particularities of the orbital deployment. First, the basics of a radar system are put forward to finally describe the different technical improvements which lead to a SAR.

2.1.1 Orbital radar acquisition characteristics

The acquisition geometry of a any radar system, in general terms, is the same for all deployments, either terrestrial, airborne or orbital. The orbital approach provides a very stable measurement, ensuring a regular revisit time over the same area.

Fig. 2.1 is a representation of the acquisition geometry. The satellite advances at a certain velocity v_s along the orbit track, known as azimuth direction as the radar emits electromagnetic pulses in the orthogonal direction, known as range direction. Usually, the antenna is not pointing exactly in its broadsight direction, but with a certain squint angle φ in order to compensate the Earth rotation. In order to avoid distance ambiguities, the antenna also has a certain elevation angle θ_e, defined respect to the nadir direction. The
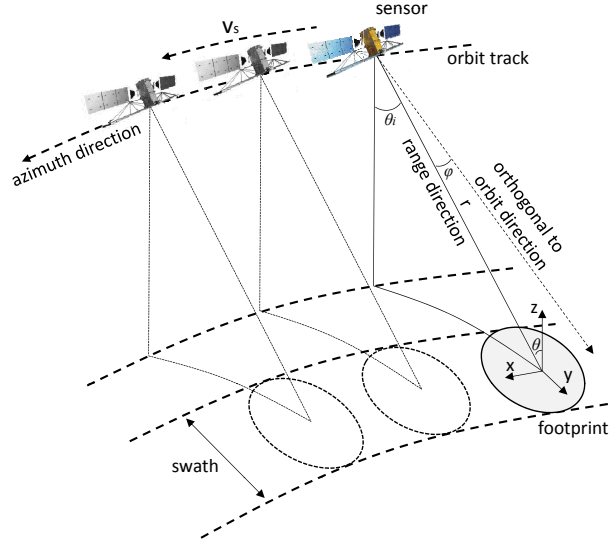
Figure 2.1: Orbital SAR system acquisition geometry

antenna illumination covers a certain area in the ground, known as *footprint*. Each point inside the footprint is associated with an incidence angle θ, defined between the normal to the ground direction z and the range direction. The angle θ is slightly bigger than θ_e due to the Earth curvature. The area scanned by the footprint as the sensor advances on the orbit track is known as *swath*.

In this context, two main orthogonal directions may be defined: *azimuth* and *range*. Azimuth is defined by the path followed by the satellite in the orbit. Range is defined by the Line of Sight (LOS) direction, i.e., the direction in which the electromagnetic pulses are emitted.

Let's first considering a static position of the instrument in the orbit. The radar system resolution in the azimuth direction, Δx, may be defined as [5]

$$\Delta x \approx r \frac{\lambda}{L} \tag{2.1}$$

where r is the distance between the satellite and the scene, λ is the signal wavelength and L is the length of the antenna in azimuth. Considering realistic antenna sizes (in the order of meters) and usual target to sensor distances (hundreds of kilometers), the achieved azimuth resolution is of a few kilometers.

The radar resolution in the range direction may be defined as [5]

$$\Delta r = \frac{c\tau}{2} \approx \frac{c}{2B} \tag{2.2}$$

where c is the speed of light, τ is the electromagnetic pulse duration and B is the pulse
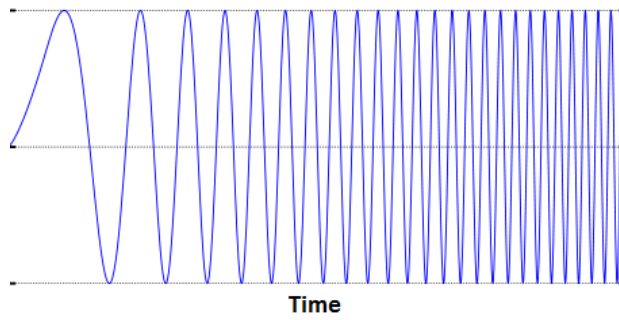
Figure 2.2: Chirp representation

bandwidth. In this configuration, achieving resolutions in the order of meters needs values of τ down to nanoseconds.

Thus a short pulse, which implies a wide spectrum, provides the wanted resolution. However, for technical issues, is convenient to employ longer pulses in order to spread the total energy transmitted along time. The ideal case would be design a pulse long both in time and spectrum. Fortunately, this pulses exist and are know as *chirp* pulses. A chirp is characterized by a long temporal duration, but the frequency is modulated as time passes in order to cover the desired bandwidth. Their mathematical expression is

$$s\left(t\right) = rect\left(\frac{t}{\tau}\right) e^{j\left(\omega t + \frac{\alpha t^2}{2}\right)} \tag{2.3}$$

where $rect(.)$ stands for a rectangular window in time, $\omega = 2\pi f$ is the angular frequency, f is the carrier frequency and α is the chirp rate, which defines the frequency variation rate of the signal. Fig. 2.2 is a graphical representation of the pulse shape. Chirp pulses are characterized by a sharp autocorrelation, which provides the needed resolution, as it will be shown in the following.

At this point, the pulse compression concept arises. This processing step is performed through a matched filter after receiving the backscattered signal [6]. It is based in the convolution of the received pulse with a conjugated and time-reversed version of the original one. This simple operation delivers sharp pulses which allow for a precise resolution in range, thanks to the aforementioned autocorrelation characteristics. For this particular pulse the bandwidth may be defined as $B = \alpha\tau$, so applying it in (2.2), the range resolution of the compressed pulse is

$$\Delta r \approx \frac{c}{2\alpha\tau} \tag{2.4}$$

Therefore, the range resolution can be easily tuned by the chirp rate, using affordable technology for orbital platforms.

2.1.2 Real Aperture Radar

Now a conventional radar system is fully defined. When scanning an area, for instance by means of a moving platform, this system is usually addressed a Real Aperture Radar (RAR). Taking advantage of the displacement of the sensor along the trajectory, the RAR instrument monitors the area covered by its footprint. In the orbital case, while advancing through the orbit it emits pulses with a cadence given by a certain Pulse Repetition Frequency (PRF). This pulses are sampled in reception, to obtain a data vector characterizing the swath in each particular azimuth position.

The satellite velocity is several orders of magnitude lower than the pulse transmission velocity, which is the speed of light. It is reasonable to consider the acquisition as an stop-and-go approach, i.e., the point in the orbit of emission and reception is the same. This allows for a 2D representation of the data acquired by the RAR instrument, simply concatenating each data vector in each azimuth position. This new image is the so-called *Raw data* acquisition. Its dimensions are azimuth and range, defining the reference system known as *slant-range*.

Each one of the range data vectors may be now improved in resolution applying the pulse compression algorithm, usually addressed as range focusing. Then, the final RAR image is characterized by a much higher resolution in range than in azimuth. This is not usually a desirable outcome, since many applications require similar resolutions in both dimensions. In the following section, the strategy to improve the resolution in azimuth is put forward.

2.1.3 Synthetic Aperture principle

The concept of synthetic aperture is fundamentally based on the well-known principle of antenna array. It states that a group of low directive antennas with identical characteristics and with the proper feeding are equivalent to a more directive antenna [7]. In this case, the array is not physically generated with different instruments. Instead, it is "synthetically" formed as a coherent combination of acquisitions at different positions of the instrument along the orbit track.

Fig. 2.3 depicts the idea behind the synthetic aperture principle. The antenna beam width in azimuth can be approximated by $\frac{\lambda}{L}$. To easily understand the idea, let's first consider a reference ground target. As the satellite advances in the orbit track, its footprint reaches the target at a certain time $t = t_i$. The target remains inside the beam until $t = t_f$. During this time lapse t_{obs}, which is equivalent to a orbital distance L_{SA}, the pulses may be combined coherently considering the array principle. An equivalent antenna is simulated with azimuth size L_{SA}, which is calculated as

$$L_{SA} = v_s \cdot t_{obs} = \frac{2r\lambda}{L}.$$

(2.5)

11
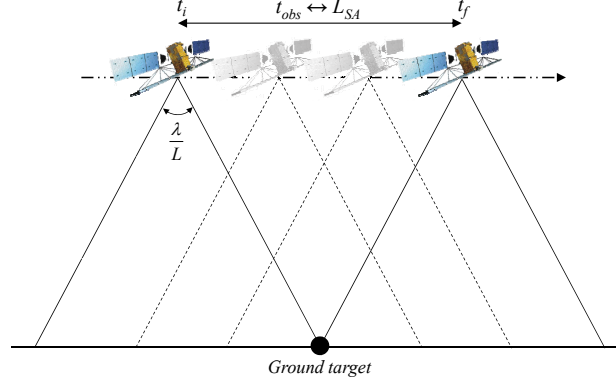
Figure 2.3: Graphic of the synthetic apperture principle

Using this new antenna size in (2.1) the resulting azimuth resolution is defined as

$$\Delta x \approx \frac{L}{2} \tag{2.6}$$

Notice how Δx does not depend on neither r nor λ. This is equivalent to say that the resolution is independent of the orbital height. This is quite intuitive since, considering a certain beam width, the observation time over the target decreases for lower heights and vice versa. The wavelength or frequency band independence represents a convenient degree of freedom for orbital missions design.

Thus, azimuth resolution depends only on the physical antenna size, achieving better resolutions using smaller antennas. Considering usual antenna sizes, the final azimuth resolution is in the order of meters.

The application of the synthtetic aperture principle over the RAR image is also known as azimuth focusing. After this process, the final SAR image is obtained, whose resolutions in range and azimuth are both in the order of meters. Notice that the sampling in azimuth is automatically defined by the PRF used during the pulse acquisition.

2.1.4 SAR image characteristics

The resulting SAR image after both range and azimuth focusing is usually addressed as Single Look Complex (SLC). This data is the basic source of information used in most techniques derived from SAR acquisitions.

As was the case for RAR images, SLCs are also represented in the slant-range reference system. They are divided in resolution cells or pixels defined by the sampling in both range and azimuth. As a general nomenclature, the azimuth direction is divided in lines and the range direction is divided in samples. Each pixel is defined by a complex value,

(a)　　　　　　**(b)**　　　　　　**(c)**
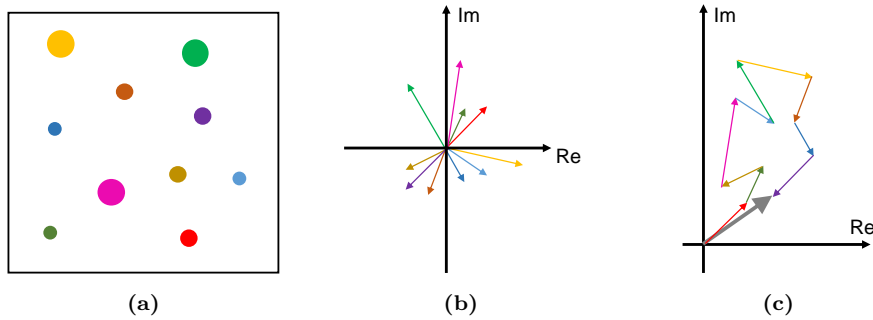
Figure 2.4: Resolution cell contributions. (a) Targets distribution inside the cell, (b) targets representation in the complex plane and (c) total contribution of the pixel.

where its amplitude is related to the cell back-scattering and its phase is related to path delay of the electromagnetic pulse. The latter parameter is the one carrying the useful information for interferometric purposes. A general expression of the SLC phase ψ is

$$\psi = \psi_{rtd} + \psi_{scat} + \psi_{aps} + \psi_{noise}. \tag{2.7}$$

The first term ψ_{rtd} is related to the round trip real distance between target and sensor. It may be defined as

$$\psi_{rtd} = -\frac{4\pi}{\lambda}r \tag{2.8}$$

The term ψ_{scat} accounts for the intrinsic characteristics of the scene illuminated. Contributions related to the internal geometry of the pixel, the local surface conditions, or the acquisition characteristics are included here. ψ_{aps} is related to the path delay suffered when crossing the atmosphere. Finally, ψ_{noise} accounts for the intrinsic noise in the radar system.

Fig. 2.4 describes how the backscattering in a pixel is generated. The resolution cell of a SLC image is about 2 orders of magnitude bigger than the wavelength. Then the retrieved back-scattering from a pixel is related to a cluster of targets, according to the sensitivity of the sensor, with its own amplitude and phase. Fig. 2.4a depicts a distribution of targets in a cell, with different geometric characteristics. Fig. 2.4b shows the backscattering of each target, represented in the complex plane with its own amplitude (length) and phase (angle with respect real axis). Fig. 2.4c shows how the total contribution of the pixel is obtained, as the addition of each individual target response.

This fact causes that neighboring pixels in an homogeneous area present different levels of total back-scattering, making the amplitude image look grainy. This phenomenon is known as *speckle* [5]. It can be modeled as a multiplicative random noise, an so it may be reduced by spatial averaging of pixels. A common approach is the boxcar filtering or *multi-look*. If several SLC images are available, speckle may be reduced with a temporal averaging as well. Fig. 2.5 depicts a comparison between a single SLC and a speckle free version obtained with a temporal averaging.

Phase is wrapped by definition, i.e, its values are defined between 0 and 2π. Then,

(a)   **(b)**

Figure 2.5: SLC image speckle example. (a) Original SLC amplitude and (b) time averaged amplitude from an SLC stack.

(a)   **(b)**   **(c)**
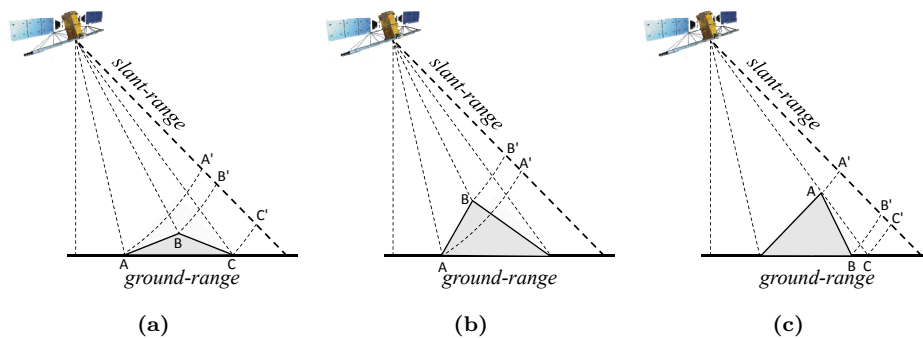
Figure 2.6: SAR acquisition distortions. (a) Foreshortening, (b) Layover and (c) Shadowing

any range distance is ultimately transformed into a phase value between these limits. The range distance increase between neighboring pixels is in the order of meters. This is equivalent to a great many cycles in phase. Then, the phase information between neighboring pixels does not make any sense. The phase of a SAR image look like random noise and it is useless by itself. In the following sections, the proper approach to exploit this phase will be put forward.

Due to the acquisition characteristics used by radar systems, SLC images are affected by distortions with respect to the actual geometric distribution of the scene monitored. This is mainly related to the incidence angle in which the radar is acquiring, see 2.1.1. Fig. 2.6 presents a graphical representation of each distortions, which are described in the following.

- **Foreshortening**: Compression of the slopes facing the sensor along the range direction. In Fig. 2.6a example, points A and B get closer in slant range coordinates. The target compression is stronger as the slope angle approaches the incidence angle.

- **Layover**: Change in the ordering of the slant-range samples respect to the scene, in slopes facing the sensor. This distortion appears when the slope angle is larger than the incidence angle. In Fig. 2.6b, points A and B are affected by layover. A typical example are buildings, where the slope angle is 90 degrees.

- **Shadowing**: Missing data due to non-illuminated areas, in slopes not facing the sensor. This effect appears when the slope angle is larger than the incidence angle. In Fig. 2.6c example, the area between point A and point C is not illuminated, so it is not possible to retrieve backscattered signal. In this case, point B is affected by shadowing and thus no response is retrieved from it.

2.1.5 SAR geocoding

SLC images are given in the slant-range coordinate system. This reference is completely related to the particular acquisition characteristics of side-looking radars. Therefore, it is necessary to project the slant-range coordinates over a geographic coordinate system, such as latitude and longitude or the Universal Transverse Mercator (UTM) projection. This is the objective of the geocoding algorithms [8].

Geographic coordinate systems can be easily related to the three dimensional Cartesian reference system, centered on the Earth. Consider at this point that the Earth surface is modeled as an ellipsoid. in this particular reference system, any point P on this surface may be defined as

$$\frac{x^2}{a^2} + \frac{y^2}{a^2} + \frac{z^2}{b^2} = 1 \tag{2.9}$$

where $P = [x, y, z]$ are the coordinates of the point and $[a, b]$ are the semi-major and the semi-minor axis of the ellipsoid.

Since it is a very simplistic model, it adapts better to the actual geoid in certain parts of the Earth depending on its parameters. Due to this, several collections of ellipsoid parameters are available, usually addressed as *datums*, which are more suited for particular locations. This thesis refers always to the World Geodetic System 84 (WGS-84) datum, which is usually taken as a global Earth reference.

Then, a relation between the slant range coordinate system and the Earth model must be defined. Fig. 2.7 displays the basic parameters involved in the geocoding algorithm. As mentioned above, an ellipsoid modeling the Earth is centered in the reference Cartesian axis. A point over the surface $\overrightarrow{\mathbf{P}}$ and a satellite location $\overrightarrow{\mathbf{S}}$ are defined as

$$\overrightarrow{\mathbf{P}} = [P_x, P_y, P_z] \tag{2.10}$$

15
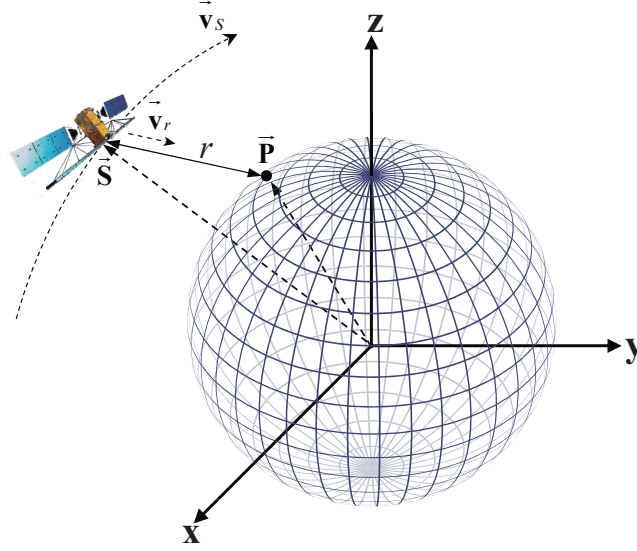
Figure 2.7: Geocoding parameters depiction

$$\overrightarrow{\mathbf{S}} = [S_x, S_y, S_z] \tag{2.11}$$

Point $\overrightarrow{\mathbf{P}}$ in the SLC image is found in a certain $[range, azimuth]$ in the slant range coordinate system. The azimuth coordinate is related to a particular $\overrightarrow{\mathbf{S}}$. Then, the distance between $\overrightarrow{\mathbf{P}}$ and $\overrightarrow{\mathbf{S}}$ is r, which is related to the range coordinate. These relations are defined by the next equations.

- **Range equation**: It represents all the possible range positions from the satellite. It is defined by a sphere centered at $\overrightarrow{\mathbf{S}}$ of radius r.

$$\left|\overrightarrow{\mathbf{S}} - \overrightarrow{\mathbf{P}}\right|^2 = (S_x - P_x)^2 + (S_y - P_y)^2 + (S_z - P_z)^2 = r_1^2 \tag{2.12}$$

- **Doppler equation**: This equation accounts for the relation between relative velocities of the satellite and the point on the ground in the LOS direction, and the Doppler frequency f_D. Since an Earth Centered Earth Fixed (ECEF) model is assumed, i.e., the cartesian axis follow the earth rotation, the velocity of $\overrightarrow{\mathbf{P}}$ is 0. Then, f_D depends only on the relative velocity of the satellite in the LOS direction $\overrightarrow{\mathbf{v}}_r$,

$$f_D = \frac{2}{\lambda}\left|\overrightarrow{\mathbf{v}}_{r1}\right| = \frac{2}{\lambda}\left\langle\overrightarrow{\mathbf{v}}_S, \widehat{\mathbf{r}}\right\rangle, \tag{2.13}$$

where $\widehat{\mathbf{r}}$ is the normalized range vector, defined as

$$\widehat{\mathbf{r}} = \frac{\overrightarrow{\mathbf{P}} - \overrightarrow{\mathbf{S}}}{\left|\overrightarrow{\mathbf{P}} - \overrightarrow{\mathbf{S}}\right|}. \tag{2.14}$$

The images are generally given in zero doppler, i.e., $f_D = 0$. In this case, this equation defines a plane which is perpendicular to the orbit.

- **Earth model equation**: This equation is the ellipsoid defined in (2.9), but taking into account the height h of the point $\overrightarrow{\mathbf{P}}$ over the Earth surface. This can be modeled by simply increasing the ellipsoid axis with this value, and evaluating the model at $\overrightarrow{\mathbf{P}}$.

$$\frac{P_x{}^2}{\left(a + h\left(\overrightarrow{\mathbf{P}}\right)\right)^2} + \frac{P_y{}^2}{\left(a + h\left(\overrightarrow{\mathbf{P}}\right)\right)^2} + \frac{P_z{}^2}{\left(b + h\left(\overrightarrow{\mathbf{P}}\right)\right)^2} = 1 \qquad (2.15)$$

Notice that h is defined as a function of the point on the ground, which can be easily obtained using an external DEM as a reference. This way, a more complex model is used, which takes into account the topography over the base ellipsoid.

Considering a certain satellite position $\overrightarrow{\mathbf{S}}$ and its velocity $\overrightarrow{\mathbf{v}}_r$, its relative point $\overrightarrow{\mathbf{P}}$ may be derived from the intersection of the aforementioned surfaces described in (2.12), (2.13) and (2.15). In fact, two possible solutions exist but one may be easily discarded knowing the looking-side of the satellite. The solution to this equation system, which is non-linear, may be carried out through a numerical approach such as the Newton-Raphson method.

2.2 SAR Interferometry and Differential SAR Interferometry

This section first describes the concept of inteferogram, which is the way to extract information from SLC phases. Then, two classic applications which use interferograms are put forward: InSAR for DEM generation and DInSAR for terrain displacement retrieval. This two simple techniques will set up the basis to understand more advanced approaches to phase exploitation such as PSI.

2.2.1 Concept of interferogram

Considering a pair of SLC images, the pixel-wise complex product known as *interferogram* is defined as

$$I = S_1 \cdot S_2^* \tag{2.16}$$

where S_i stands for the complex value of a certain pixel in each image respectively. In general, S_1 is addressed as *master* and S_2 as *slave* of the interferogram. From the definition of SLC phase ψ in (2.7), The *interferometric phase* ϕ may be defined as

$$\phi = \psi_1 - \psi_2 = \frac{4\pi}{\lambda} \left(r_2 - r_1 \right) + \Delta\psi_{scat} + \Delta\psi_{aps} + \Delta\psi_{noise} \tag{2.17}$$

where r_1 and r_2 stand for the target to sensor distance of master and slave SLCs respectively. The other interferometric phase components are related to the phase difference due scattering changes, atmospheric artifacts and the system noise. $\Delta\psi_{scat}$ is generally considered negligible, since the main aim of this techniques are stationary targets. Thus, the scattering characteristics of the scene should remain stable. This is not generally the case for the other components. Specially, $\Delta\psi_{aps}$ is on of the main concerns in all interferometric techniques, since it is hard to model and be compensated for. In any case, to understand the rationale behind each interferometric technique, these components are not considered in the following. Then, (2.17) simplifies as

$$\phi = \frac{4\pi}{\lambda} \left(r_2 - r_1 \right) = \frac{4\pi}{\lambda} \Delta r, \tag{2.18}$$

where, apart from the wavelength, the interferometric phase is related only to the target to sensor distance difference Δr.

2.2.2 SAR Interferometry for Digital Elevation Map generation

This section is devoted to explain how the phase difference is related to the underlying topography of the scene. This was one of the first applications developed which exploited the interferometric phase.
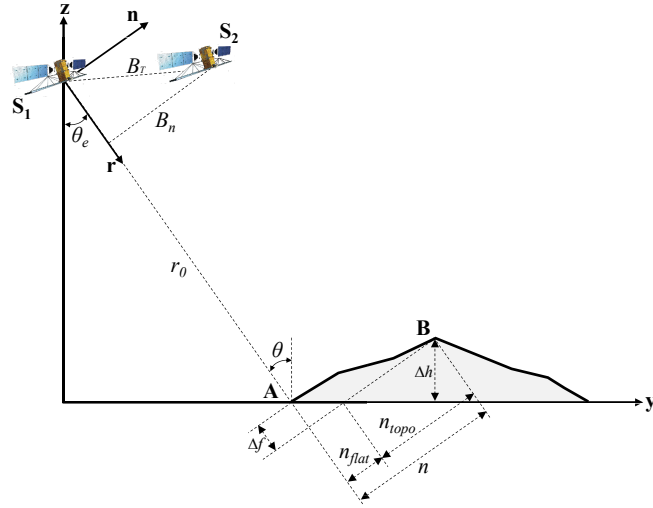
Figure 2.8: InSAR concept depiction

From an intuitive point of view, the mechanism works is the same as the eye. The interferogram from two acquisitions taken from slightly different positions or perspectives contains depth information, in this case, the variation in height in the observed scene. It is worth remembering that ideally both acquisitions should be taken at the same time, in order to minimize unwanted phase components.

The relation between interferometric phase and the observed topography is derived geometrically. It is demonstrated that an increment in height between two points can be related to an increment in the interferometric phase [9].

Fig. 2.8 serves as a reference to understand the InSAR concept. The axis $\mathbf{z}$ and $\mathbf{y}$ are the direction perpendicular to the ground and the LOS direction projected to the ground, respectively. The orthogonal axis $\mathbf{x}$, which is not represented, accounts for the azimuth direction. Two satellite acquisitions with the same $\mathbf{x}$ coordinate, but taken from different positions over the $\mathbf{yz}$ plane are considered, $\mathbf{S_1}$ and $\mathbf{S_2}$, addressed in the following as *master* and *slave*. An auxiliary reference axis is set in $\mathbf{S_1}$, defined by the dimensions $\mathbf{r}$ and $\mathbf{n}$, which are the master slant-range dimension and its perpendicular dimension respectively. The physical separation between $\mathbf{S_1}$ and $\mathbf{S_2}$ in either of the two reference systems defined, B_T, is known as *baseline*. The component of B_T in the $\mathbf{n}$ direction, B_n, which is called *perpendicular baseline*, is of particular interest in the following. The master sensor is observing the scene with an elevation angle θ_e. For the sake of simplicity, the Earth curvature is neglected so the incidence angle θ is equal to θ_e.

Two points $\mathbf{A}$ and $\mathbf{B}$ on the Earth surface, at different positions in the $\mathbf{yz}$ plane are considered. The height difference between $\mathbf{A}$ and $\mathbf{B}$, i.e., the distance in $\mathbf{z}$ is defined as Δh. Consider Δr_A and Δr_B as the difference in distance between each satellite and

target A and B, respectively. An increment in this difference may be is equivalent to [9]

$$\Delta(\Delta r) = \Delta r_A - \Delta r_B = \frac{nB_n}{r_0}. \tag{2.19}$$

where n is the distance between $\mathbf{A}$ and $\mathbf{B}$ in the $\mathbf{n}$ dimension and r_0 is the distance between $\mathbf{S_1}$ and $\mathbf{A}$. Applying (2.19) to (2.18), the increment of interferometric phase between $\mathbf{A}$ and $\mathbf{B}$ is

$$\Delta\phi_{AB} = \frac{4\pi}{\lambda}\Delta\left(\Delta r\right) = \frac{4\pi}{\lambda}\frac{B_n}{r_0}n. \tag{2.20}$$

A relation between an increment in the interferometric phase and n has been established, with the perpendicular baseline B_n acting as a proportionality constant. Note that B_n is related to the sensitivity of the measurement, being more sensitive as B_n increases.

In order to obtain the relation with the height difference, first a distinction must be made. The distance n has in fact two components,

$$n = n_{flat} + n_{topo}. \tag{2.21}$$

On the one hand, the distance n_{flat} is not related to height difference. In fact, it is proportional to the slant-range distance difference. On the other hand, n_{topo} can be directly related to the height difference Δh between $\mathbf{A}$ and $\mathbf{B}$. By simple trigonometry, both components can be related to Δf and Δh as follows,

$$n_{flat} = \frac{\Delta f}{\tan\theta} \tag{2.22}$$

$$n_{topo} = \frac{\Delta h}{\sin\theta}. \tag{2.23}$$

Applying this two terms separately to (2.20), the interferometric phase increment between $\mathbf{A}$ and $\mathbf{B}$ is divided in two components, one related to the flat earth and the other to topography, defined as

$$\Delta\phi_{AB,flat} = \frac{4\pi}{\lambda}\frac{B_n}{r_0}\frac{\Delta f}{\tan\theta} \tag{2.24}$$

$$\Delta\phi_{AB,topo} = \frac{4\pi}{\lambda}\frac{B_n}{r_0}\frac{\Delta h}{\sin\theta}. \tag{2.25}$$

Since the variation in Δf is linear, ideally the flat earth component of the interferometric phase follows a linear pattern in the range dimension. In the real case, a certain azimuth component is present due to non perfectly parallel orbits tracks between acquisitions. Nonetheless, this term is easily estimated and compensated for.

The topographic component of the phase is then proportional to a relative height measure. However, the phase is wrapped, i.e., it is defined only in the interval $[-\pi, \pi]$. It must undergo a phase unwrapping process in order to obtain its full cycles [10–16], which are directly related to topography. At this point, a reference point of known height must be fixed to go from relative to absolute heights. Finally, the resulting DEM is obtained applying the geocoding techniques described in 2.1.5 in order to obtain the height information in geographical map coordinates.
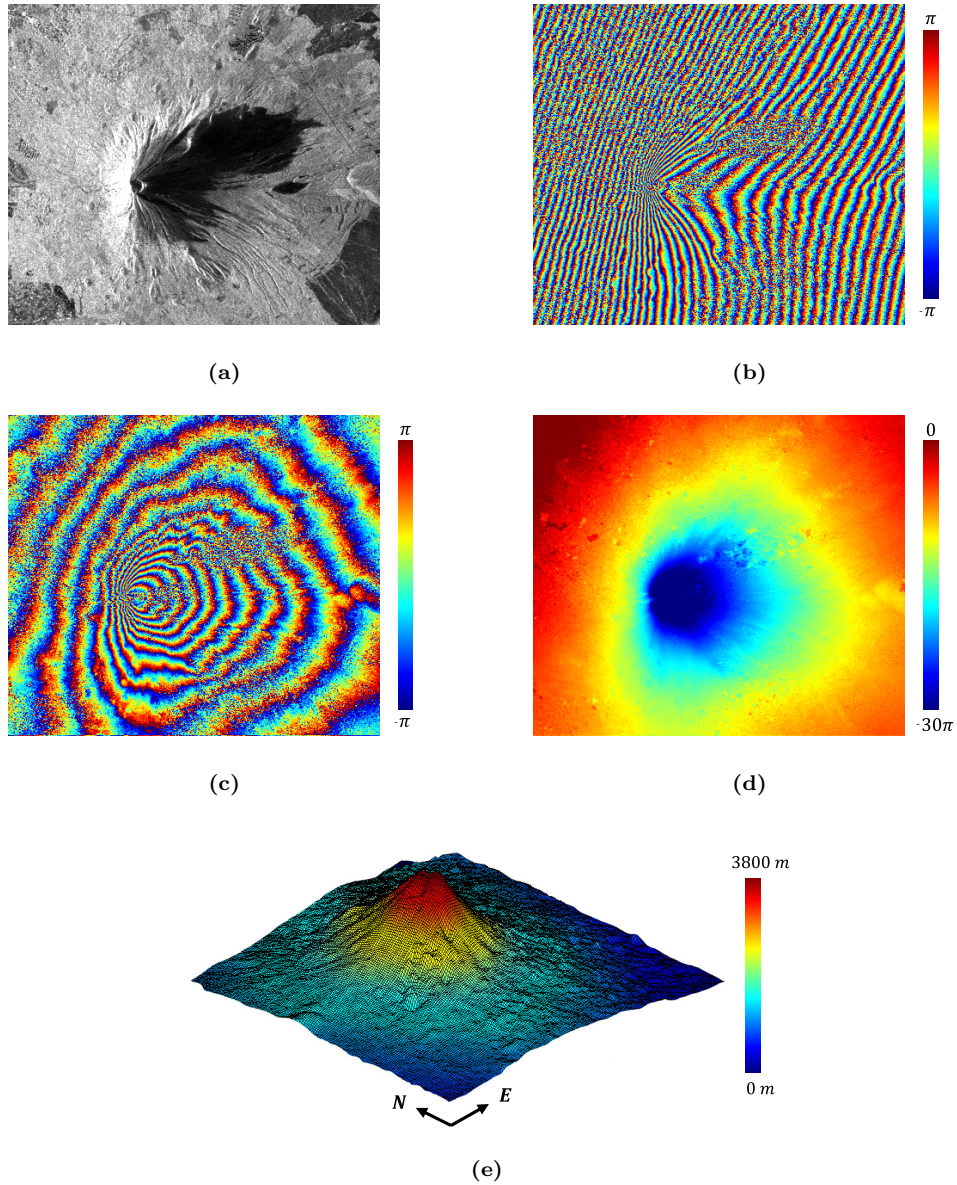
Figure 2.9: DEM generation in Mount Fuji (Japan), using ALOS PALSAR data. (a) Mean amplitude SLC image. (b) Interferometric phase, containing the flat earth and the topographic component. (c) Topographic phase, after removing the flat earth component. (d) Unwrapped topographic phase. (e) Geocoded DEM.

The DEM generation process is summarized in Fig. 2.9, using ALOS PALSAR data from the mount Fuji, in Japan. Two SLC acquisitions with a perpendicular baseline of 278 meters have been selected. Fig. 2.9a represents the averaged amplitude between the
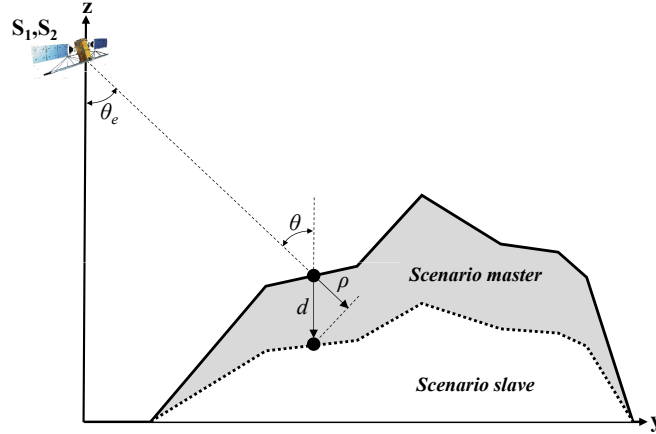
Figure 2.10: DInSAR depiction

master and slave SLCs. Fig. 2.9b shows the raw interferometric phase, where the flat earth component, consisting of a slightly tilted linear phase pattern in range is clearly identifiable. In general, if the topography is not too steep, the flat earth component of the phase is the most noticeable. In this case, due to the presence of Mount Fuji, the underlying distortions due to the topographic component can also be appreciated. Fig. 2.9c is the extracted topographic phase, after subtracting the flat earth component. In this case, the phase patterns already follow the topography, but it is wrapped in the $[-\pi, \pi]$ interval. They may be interpreted as height isolines, i.e., each color inside a particular fringe presents the same height. Fig. 2.9d shows the resulting phase once the unwrapping process is applied. For this purpose, an implementation called SNAPHU of the statistical-cost network-flow algorithm proposed in [17] has been used. This phase is directly related to the height, save for a unknown offset, through (2.25). The shift is corrected using an a priori known height over a location in the scene. Finally, Fig. 2.9e shows 3D representation of the geocoded DEM of mount Fuji.

2.2.3 Differential SAR Interferometry for terrain displacement retrieval

The InSAR technique assumes an stable scenario, i.e., the topography of the scene remains constant in the time lapse between the master and slave acquisitions. Let's consider the case where the topography suffers a displacement between acquisitions. Fig. 2.10 illustrates the situation.

To easily understand the concept, let's assume that the the spatial baseline of the interferogram B_n is equal to 0, i.e., master and slave acquisitions are taken from exactly the same point of view. In this configuration, the flat Earth and the topographic component of the interferometric phase are canceled. In this example, the ground point under study is

affected by a subsidence phenomenon, suffering a vertical displacement d between master and slave acquisitions. Since the SAR sensitivity is in the LOS direction, the measured component of the total displacement is ρ. The interferometric phase associated to this displacement is defined as

$$\phi_{disp} = \frac{4\pi}{\lambda}\rho. \qquad (2.26)$$

Now let's assume the generic case where B_n is not equal to 0, which is always true for the orbital case. In this case, the flat Earth and the topographic components are present. To preserve the consistency between chapters, the same approach as in 2.2.2 is followed, where the relative interferometric phase between two points A and B is considered instead of the phase itself. then, a the general expression of the relative interferometric phase, accounting also for displacement component, may be defined as

$$\Delta\phi_{AB} = \Delta\phi_{AB,flat} + \Delta\phi_{AB,topo} + \Delta\phi_{AB,disp} = \frac{4\pi}{\lambda}\frac{B_n}{r_0}\frac{\Delta f}{\tan\theta} + \frac{4\pi}{\lambda}\frac{B_n}{r_0}\frac{\Delta h}{\sin\theta} + \frac{4\pi}{\lambda}\Delta\rho \quad (2.27)$$

where $\Delta\rho$ stands for the displacement increment between the points **A** and **B**. The final objective is to extract the displacement component, trying to cancel the other components.

Among the different possibilities available, the most common choice is to use an external DEM as a reference. As seen in 2.1.5, the Earth model can be obtained refining the reference ellipsoid with the DEM information. Through geocoding techniques (see 2.1.5), and assuming that the orbital parameters are known, it is possible to synthesize the flat earth and the topographic component, since they only depend on the geometry of the master and slave acquisitions. This synthetic phase can be subtracted for the interferogram phase, isolating the component associated to displacement. This way, the so-called *differential interferogram* is obtained, including only the displacement component of the phase. Notice that due to inaccuracies in the reference DEM employed, a certain residual topographic component is also present in the final differential phase, leading to the following general expression,

$$\Delta\phi_{AB} = \Delta\phi_{AB,\varepsilon} + \Delta\phi_{AB,disp} = \frac{4\pi}{\lambda}\frac{B_n}{r_0}\frac{\Delta\varepsilon}{\sin\theta} + \frac{4\pi}{\lambda}\Delta\rho \qquad (2.28)$$

where $\Delta\phi_{AB,\varepsilon}$ is the residual topographic phase component and $\Delta\varepsilon$ is the residual topographic error, both relative values between points A and B. This may be an issue when analyzing single differential interferograms to extract its displacement information. In further section it will be seen how PSI techniques, using a multi-temporal dataset of SAR acquisitions, are able to estimate the residual topographic component as well as the displacement.

Let's assume that the residual topographic component is negligible. After applying an unwrapping process over the differential interferogram, this phase can be directly related to the displacement in the LOS direction occurred between master and slave acquisitions, through (2.26). As in the InSAR case, a seed point of known displacement, usually for an area which remains stable between the acquisitions, must be introduced to solve the phase uncertainty.

(a)

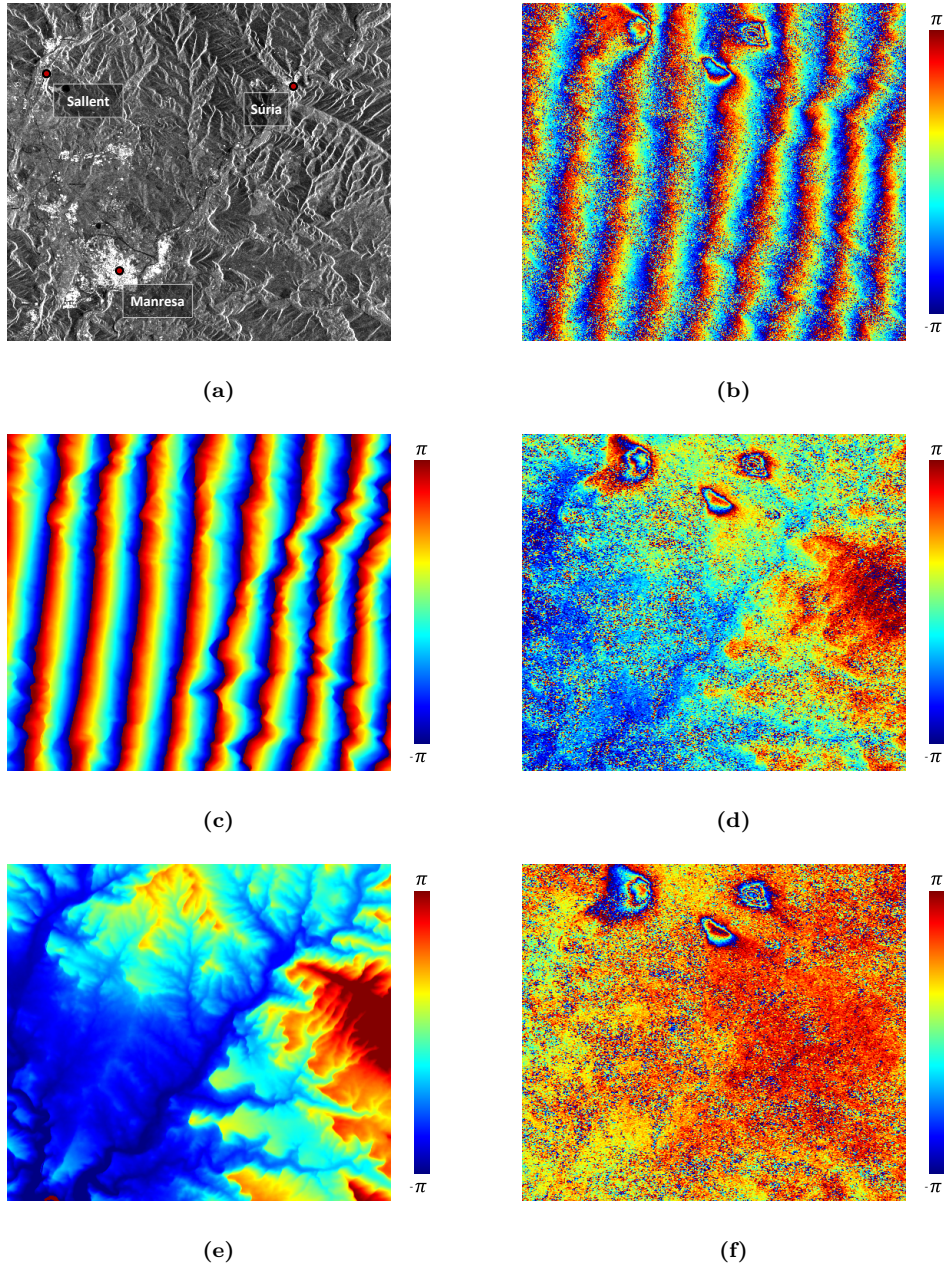**(b)**

(c)

(d)

(e)

(f)

Figure 2.11: DInSAR example in the central part of Catalonia (Spain). (a) SLC mean amplitude image. (b) Inteferometric phase. (c) Synthetic interferometric phase. (d) Interferometric phase after subtracting the flat earth component. (e) Topographic component of the synthetic interferometric phase. (f) Differential interferometric phase.

24

Fig. 2.11 serves as an example of the different steps to obtain a differential interferogram. Fig. 2.11a shows a mean amplitude image of the studied area, located in the central part of Catalonia (Spain), where several underground mining activities are taking place. These works caused severe subsidence phenomena on the surface over the mining area. Fig. 2.11b represents the interferometric phase, where three subsidence bowls can be clearly seen over the flat-earth component. Fig. 2.11c shows the synthetic interferometric phase obtained using an external DEM of the area and the orbital information. The correlation with 2.11b is clearly appreciated, except for the displacement patterns. The synthetic phase can be divided into the flat earth contribution and the topographic component. Fig. 2.11d represents the original interferometric phase after extracting only the flat earth component. Fig. 2.11e stands for the synthetic interferometric phase, after extracting also the flat earth. When ignoring the displacement component in the former, Fig. 2.11d and Fig. 2.11e both represent the topographic component of the phase. Fig. 2.11f is the phase difference between the two previous components, the differential interferogram, containing only the displacement information.

2.2.4   Interferometric phase quality

SLC acquisitions are affected by different noise or decorrelation sources which degrade the quality of the interferometric phase. Thus, a estimation of this phase quality is mandatory in order to assess the goodness of the information retrieved. A common approach for this purpose is the inteferometric coherence estimator [18], defined as

$$\gamma = \frac{E\left\{S_1 S_2^*\right\}}{\sqrt{E\left\{|S_1|^2\right\} E\left\{|S_2|^2\right\}}} \tag{2.29}$$

where S_1 and S_2 are pixels in the master and slave SLCs respectively and $E\left\{.\right\}$ stands for the expectation operator. The phase quality is directly related to the inteferometric coherence magnitude $|\gamma|$, which can be related to the Signal to Noise Ratio (SNR) as

$$|\gamma| = \frac{\text{SNR}}{\text{SNR} + 1}. \tag{2.30}$$

The $|\gamma|$ estimation is defined in the $[0, 1]$ interval, ranging from total decorrelation to perfect correlation. Unfortunately, only one realization for each pixel is available, so the application of the expectation estimator through ensemble averaging is not possible. An spatial averaging is used instead, assuming ergodicity, which lead to a reformulation of the coherence as [19]

$$\hat{\gamma} = \frac{\sum\limits_{n=1}^{N} S_1\left(n\right) S_2^*\left(n\right)}{\sqrt{\sum\limits_{n=1}^{N} |S_1\left(n\right)|^2 \sum\limits_{n=1}^{N} |S_2\left(n\right)|^2}} \tag{2.31}$$

where N is the size of the averaging window. On the one hand, the amplitude $|\hat{\gamma}|$ is in fact the maximum likelihood estimator of the coherence magnitude $|\gamma|$ [20]. On the other
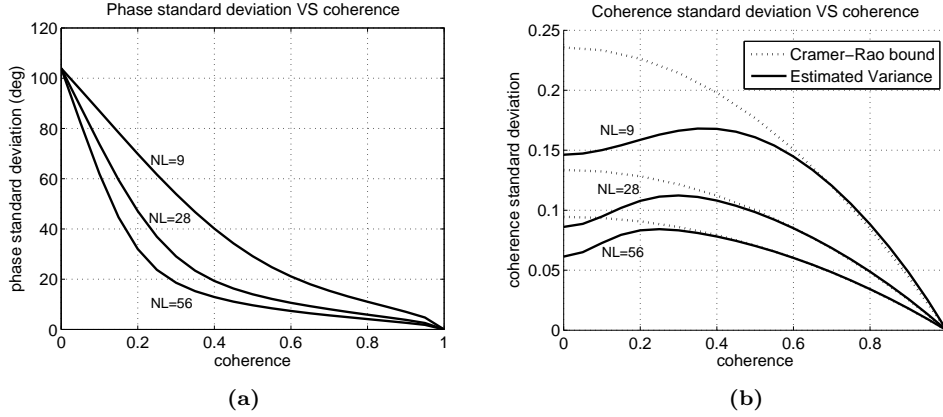
Figure 2.12: Relation between (a) coherence and phase standard deviation and (b) coherence estimator standard deviation. NL is the number of looks.

hand, the phase of $\hat{\gamma}$ is equivalent to the interferometric phase of the combined pixels in the averaging.

The spatial averaging, in the context of SAR, is usually addressed as *multi-look*, where N is the *number of looks*. Since SLC images are usually over-sampled, N must account for the effective number of looks, considering the relation between the image resolution and the final pixel spacing.

The coherence estimation is related to the phase standard deviation, as shown in Fig. 2.12a [18]. There are different relation curves depending on the effective number of looks NL. The relation between real and effective looks is given by the relation between resolution and pixel spacing, i.e., the oversampling factors both in range and azimuth. The values employed in this work are the ones shown in Fig. 2.12, corresponding the 5x3, 9x5 and 13x7 multi-look windows, in lines per samples notation. Fig. 2.12b shows the standard deviation of the coherence estimator related to the actual coherence values.

There are several agents which degrade the coherence, and thus the phase quality. The following decorrelation factors may be defined:

- **Misregistration decorrelation**: In order to be combined, SLC acquisitions must be precisely registered to the same reference (see 2.2.5). In general, a minimum accuracy of 1/16 pixels is required to ensure enough interferometric phase quality [18]. All inaccuracies in this step lead to decorrelation.

- **Spatial decorrelation**: Term due to the different incidence angles between acquisitions. From a spectral point of view, this is equivalent to consider different parts of the range spectrum. Non overlapping parts lead to decorrelation [21]. This effect is related to the perpendicular baseline B_n which characterizes the interferogram, leading to higher spatial decorrelation as B_n increases. In fact, there exists a crit-
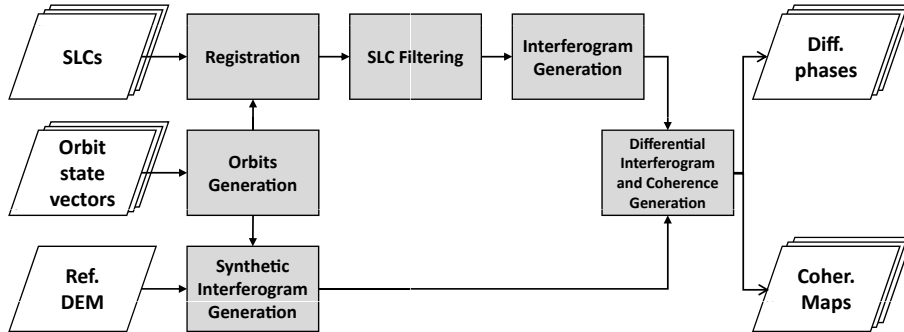
Figure 2.13: DInSAR chain flowchart

ical baseline, where the range spectra of master and slave do not overlap, which is equivalent to total decorrelation. This source or decorrelation may be reduced applying range filtering to only consider the overlapping parts of the spectra.

- **Doppler decorrelation**: This is the equivalent case of the spatial decorrelation but in the azimuth direction, caused by different squint angles, i.e., different Doppler centroids for each acquisition. This leads to the decorrelation of the azimuth spectra. As for the spatial decorrelation, filtering to keep only the azimuth common spectra may be applied to minimize this degradation of the phase.

- **Volumetric decorrelation**: This term is related to the penetration of the radar waves into the illuminated scene. In fact, it analyzes the similarity between the backscattering target responses in the vertical direction between the images of the interferogram. Consequently it will strongly depend on the height target distribution within the resolution cell as well as the radar wavelength and the scattering medium.

- **Temporal decorrelation**: This term is due to changes in the scene in the time lapse between the two acquisitions. It is closely related to the scattering term in the interferometric phase described in (2.17). It is very hard to characterize, since it depends on may factors.

- **Thermal decorrelation**: This term accounts for all the noise introduced by all the measuring system.

2.2.5 Interferometric processing chain

This subsection is devoted to describe the different steps in order to set up the SAR dataset, departing from the SLC acquisitions until obtaining the differential interferograms. Fig. 2.13 represents a flowchart of this process.

The inputs are the SLCs, the orbital data and a reference DEM. The different blocks of the process are briefly described in the following.

- **Orbit generation**: This step obtains the information regarding the sensor position and the timing parameters. Generally the orbital positioning is given in state vectors, at time intervals much larger than the azimuth spacing of SLCs. This poor sampling is enlough, since the advance over the orbit track is extremely smooth and predictable. Each state vector provides its position and velocity in Cartesian coordinates. An interpolation using a third order polynomial is applied to retrieve the orbit information at each azimuth position.

  Usually, the orbital state vectors are extremely precise. On the contrary, the timing parameters both in azimuth and range may be inaccurate. Nevertheless, they can be corrected using ground control points, which relate the slant-range and the ground-range plane, by applying the geocoding techniques described in 2.1.5).

- **Registration**: This step resamples the slave SLC to match the geometry of a reference master SLC. The objective is that correlative pixels map the same area in the scene monitored. This is necessary, since the particular geometries of the acquisitions lead to different geometric distortions, as described in 2.1.1. Registration is carried out in a two steps approach: a *coarse registration*, which finds a global offset between acquisitions and a *fine registration*, that corrects particular offsets due to the local distortions. The later is carried out with sub-pixel precision, generally 1/16 pixels, since the interferometric phase is highly sensitive to misregistration errors. Both steps are based on geocoding techniques [22], using the reference DEM as an input.

- **SLC filtering**: SLC images may be filtered, both in range and azimuth, in order to minimize the spatial and Doppler Centroid decorrelation described in 2.2.4. The filtering is performed over the images, previously to the creation of the interferograms, to remove the non overlapping parts of the spectra in each dimension. Mind that this is step is done if working with distributed scatterers. When dealing with point targets, due to its wide spectrum, it is not advisable to apply any kind of filtering.

- **Inteferogram generation**: This step simply applies the complex product between master and slave seen in (2.16) in order to obtain the interferogram.

- **Synthetic interferogram generation**: This step generates the synthesized topographic phase using the orbital information and an external DEM as topographic reference. This process is done through the geocoding techniques, as shown in 2.2.3.

- **Differential interferogram and Coherence generation**: This step subtracts the synthetic topographic component from the interferogram in order to obtain the differential interferometric phase. In addition, the coherence estimation map may be obtained, with its related multi-looked differential phase.

2.3 Persistent Scatterers Interferometry: The Coherent Pixels Technique

In section 2.2.3, the basic technique to extract the terrain displacement between a pair of SLC acquisitions has been put forward. This section describes the advanced techniques able to deal with a multitemporal SAR dataset, composed by a stack of SLC acquisitions covering a certain time span. The objective is to retrieve the temporal evolution of terrain displacement during this period.

The first step is to apply the interferometric chain described in 2.2.5 to the whole data-set of SLC images to obtain the interferograms data-set. Two additional considerations must be taken into account:

- A single reference SLC is selected to co-register all the acquisitions, in order to map every image to the same geometry. This image is addressed in the following as *master-master*. The optimum candidate is usually the center of mass of the SLC space/time/doppler 3D representation. Space values are defined as the spatial baseline of each SLC respect to an arbitrary one. Then, ideal master-master image is the one that globally minimizes the separation to the rest in this 3D space.

- Considering N acquisitions, the total number of interferograms M that may be obtained is

$$M = \binom{N}{2} = \frac{N(N-1)}{2}. \tag{2.32}$$

For a large set of images the number of possible interferograms is overwhelming. Moreover, due to the decorrelation factors described in 2.2.4, not all the interferograms provide enough phase quality, so an interferogram selection may be carried out. This selection is done considering as features the spatial and temporal baselines and the Doppler Centroid difference of each interferogram. The discrimination can be done by thresholding this parameters or by more sophisticated approaches, such as a Delaunay triangulation in the 3D space formed by the selected features [23,24].

Once the interferometric chain is applied, a collection of differential interferograms is available. Also the multi-looked versions are generated, with the associated coherence maps. In the following, the particular approach followed in this thesis to perform the PSI analysis, the so-called Coherent Pixel Technique (CPT) [25,26], is described.

The final objective of any PSI analysis is to extract the displacement evolution along the time period covered by the interferogram stack. In the ideal case, the information contained in the stack refers only to displacement phenomena, since all the other geometric components are canceled. This is hardly the case, for different reasons:

- The orbital information accuracy affects both in the precision of the geocoding algorithms and the geometric components phase calculation, which involves the

spatial baseline, see (2.24) and (2.25).

- The atmospheric component is still present in the interferograms phase. It is not easy to compensate for, since existing atmospheric models are usually not able to characterize it with enough accuracy.

- The reference DEM used to extract the flat earth and topographic components of the phase does not model accurately enough the real topography. This may happen for different reasons, such as the lack of resolution, incomplete characterization (buildings, vegetation, ...) or its intrinsic accuracy.

Errors in orbital data are mostly systematic, leaving clear linear phase patterns in the differential phase. Then, they can be estimated from the actual phase and compensated for. This is a particular issue in the data-set employed in this thesis, since the accuracy of Radarsat-2 state vectors is rather poor and this residual orbital component is always present.

The atmospheric component in the interferograms is estimated at the very end of the PSI processing, based on statistical criteria.

Errors introduced by the reference DEM basically leave behind a residual topographic component in the differential phase. This component is addressed as *topographic error*. In the following, the methodology to estimate this component along with the displacement rate is put forward.

The stack of interferograms is characterized by two baseline distributions, the temporal and the spatial baselines. This distributions provide sensitivity in both in topography and displacement. Both measurement are in fact independent, since they are related only to one of the baselines. This fact allows the PSI analysis to estimate and separate them.

Fig. 2.14 shows the flowchart of the CPT algorithm. The following subsections are devoted to describe each one of the steps carried out to obtain reliable displacement and topographic error estimations.

2.3.1 Pixel candidates selection

When dealing with multi-temporal SAR data-sets in the framework of PSI, the relevant information is found in the so-called Persistent Scatterers (PS). This is a general term to describe targets that have an stable response along the monitoring time span, since it implies a good interferometric phase quality.

Thus, a pre-selection of Persistent Scatterers Candidates (PSC) is carried out in order to avoid a-priori low quality data. This selection is based on a estimation of the phase quality
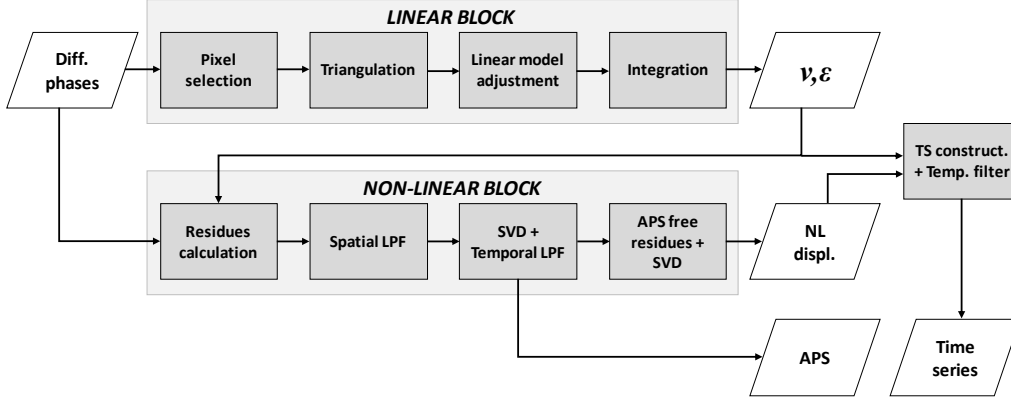
Figure 2.14: CPT flowchart

which considers the whole data-set. In the following, the different estimators available in the literature are described.

- **Coherence stability**: In 2.2.4, the coherence estimator which obtains a measurement of the interferometric phase quality has been described. The temporal sensitivity of this estimation is limited to the two acquisitions involved in the interferogram. The coherence stability estimator, which aims to provide a general measure of quality for the whole data-set, is the average of the modulus of all the individual coherence estimations [25]. The estimator is defined as

$$|\bar{\gamma}| = \frac{1}{M} \sum_{m=1}^{M} |\hat{\gamma}_m| \qquad (2.33)$$

where M is the number of interferograms involved in the estimation and $\hat{\gamma}_m$ its individual complex coherence. The pixel selection is carried out applying a threshold to the values of the estimation. The relation between phase standard deviation and coherence is non-linear, as it can be seen in Fig. 2.12a. Then, the mean coherence is not directly related to the mean phase standard deviation of each element involved. However, in this case it is a good approximation, since the meaningful pixels are supposed to be temporally stable, and thus keep similar values of coherence, where the function is approximately linear. Then, Fig. 2.12a may be used as a reference to set the coherence quality threshold.

The main drawback of this approach is the resolution loss due to the multi-look, which may difficult the detection of localized phenomena. On the contrary, the main advantage is that the phase quality estimation is good even when the number of interferograms is low.

- **Amplitude Dispersion (dA)**: This pixel selection method aims for the so-called Permanent Scatterers [27], high reflectivity targets which remain stable along the temporal span of the acquisitions. This kind of scatterers exhibit a low dA, defined
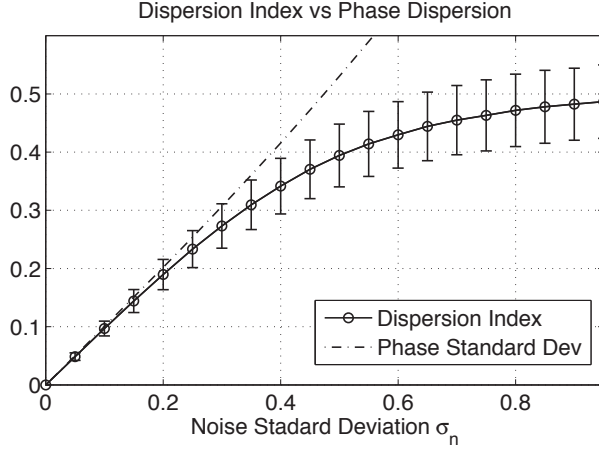
Figure 2.15: Relation between dA and phase standard deviation, based on numerical simulation.

as

$$dA = \frac{\sigma_A}{m_A} \tag{2.34}$$

where σ_A is the amplitude standard deviation and m_A is the mean amplitude, both along the temporal domain. Pixels with low values of D_A are associated with a low phase standard deviation, as demonstrated in [27] through a numerical simulation. Fig. 2.15 shows the result of this simulation, relating the phase standard deviation with the dA. The goodness of the estimation, reflected in the error bars, is directly related to the number of acquisitions N considered. It is assumed that a minimum of 25 SLCs is necessary to obtain a reliable estimation [27]. The main drawback of this method is the fact that SLC amplitudes must be radiometrically calibrated, to eliminate the intrinsic acquisition dependencies. The main advantage is the preservation of the original resolution.

- **Temporal Sublook Coherence (TSC)**: As in the dA case, this estimator also aims for point-like scatterers, but its detection is based on its spectral properties, specifically in its wide band flat spectrum [28]. SLCs spectrum is divided in two *sublooks*, and the preservation of the flat spectrum is assessed applying the coherence estimator between sublooks along time. For each pixel, the time series in the first and second sublook stacks are taken as master and slave for the coherence estimation. This approach is summarized as

$$TSC\,(i,j) = \frac{\left| \sum\limits_{t=1}^{N} SL_1\,(i,j,t) \cdot SL_2^*\,(i,j,t) \right|}{\sum\limits_{t=1}^{N} |SL_1\,(i,j,t)|^2 \cdot \sum\limits_{t=1}^{N} |SL_2\,(i,j,t)|^2} \tag{2.35}$$

where SL_1 and SL_2 are the sublook stacks, indexed by the spatial dimensions i and j and the temporal dimension t. Notice how the TSC represents only the modulus
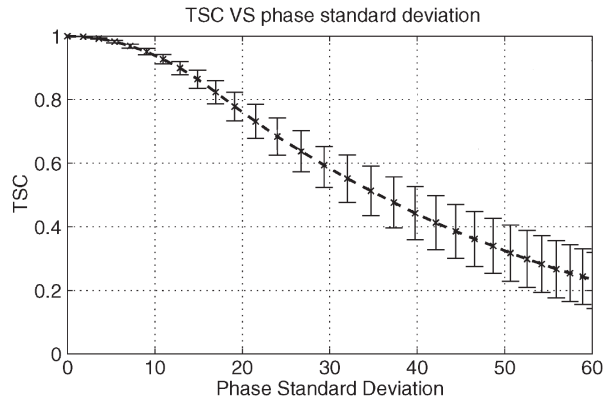
Figure 2.16: Relation between TSC and the phase standard deviation, based on a numerical simulation.

of the estimation, while the phase is rejected. As in the dA, the relation between the TSC and the phase standard deviation has been derived through numeric simulation [28], obtaining the relation shown in Fig. 2.16.

The main drawback of this method is the factor of two loss in range resolution due to the sublooks generation. The main advantages are than no radiometric calibration is necessary and the number of images to obtain a reliable estimation is lower than in the dA case [28]. Moreover, since the amplitude plays no role, it allows the detection of phase stable targets with fluctuating amplitude, such as highly directive scatterers.

2.3.2 Linear estimation

Once a pixel selection is obtained, the CPT algorithm proceeds to the so-called *Linear block*, which retrieves the displacement rate and topographic error for each pixel candidate. Note that both measurements are global, so this step does not still deliver the temporal evolution but only the displacement velocity. The linear block consists of the following steps:

- **Phase links generation**: As mentioned before, the interferometric phase of each interferogram contains a random constant phase term. In order to cancel this component, the CPT approach deals with relative phases instead of absolute ones, taking into account the phase increment among neighboring pixels. Since the unknown phase offset is constant for the whole interferogram, the random phase term is thus canceled. In general, two different strategies are followed to relate neighboring pixels:

– *Delaunay triangulation*: This is an efficient approach to connect every pixel in the scene. It creates a network of non-overlapped triangles formed by the links among pixels [23].

– *Spiderweb triangulation*: This approach aims to connect each an every pixel within a certain distance. It is more inefficient than the Delaunay triangulation, but gives more redundancy to the network. It may be very useful when the overall quality of the interferometric phase is low or the pixel distribution is sparse.

Working with phase links entail additional benefits. Since the links are among neighboring pixels, the phase increments are supposed to be small. This fact minimizes the phase wrapping events, making it possible to process the interferometric data without applying any phase unwrapping techniques. Phase unwrapping is one of the most difficult steps in the interferometric process, so to be able to avoid it is a very positive trait. As it will be shown in the following, even if some links are wrapped, it is possible to overcome this issue if a good distribution of interferograms is at disposal. Moreover, phase linking is also able to deal with unwanted phase contributions which evolve smoothly in space, such as the atmospheric artifacts or baseline errors, which are also minimized.

- **Linear model adjustment**: This step obtains the displacement rate and the topographic error increments associated to each link set during the phase link generation. In order to do so, a linear phase model is defined as [25, 26]

$$\Delta\phi_{lin,i} = \frac{4\pi}{\lambda}T_i\Delta\upsilon + \frac{4\pi}{\lambda}\frac{B_{n,i}}{r_0\sin\theta}\Delta\varepsilon \qquad (2.36)$$

where i is the interferogram index, T_i and $B_{n,i}$ are the temporal and spatial baselines, λ is the wavelength, r_0 is the range distance, θ is the incidence angle and finally, $\Delta\upsilon$ is the displacement rate increment and $\Delta\varepsilon$ is the topographic error increment. Considering a particular link, a Model Adjustment Function (MAF) is defined as

$$\Gamma = \frac{1}{M}\sum_{i=1}^{M}\left|e^{-j\Delta\phi_i} - e^{-j\Delta\phi_{lin,i}}\right|^2 \qquad (2.37)$$

where $\Delta\phi_i$ is the real phase increment and M is the number of interferograms. Γ is a 2D function, where its variables are the mean displacement and the topographic error increments. Its minimization, which may be understood as a fitting of the model defined in (2.36) to the real data $\Delta\phi_i$, provides the optimum values for $\Delta\upsilon$ and $\Delta\varepsilon$. Due to a restriction in one of the minimization algorithm used, the Conjugate Gradient Method (CGM), which only works with real functions, an alternative MAF is defined as

$$\Gamma = 1 - \frac{1}{M}\sum_{i=1}^{M}Re\left\{e^{-j(\Delta\phi_i-\Delta\phi_{lin,i})}\right\}. \qquad (2.38)$$

Fig. 2.17 is a 3D representation of a MAF. In this case, the optimum values of mean displacement and topographic error are 0. Any MAF function has the next characteristics:
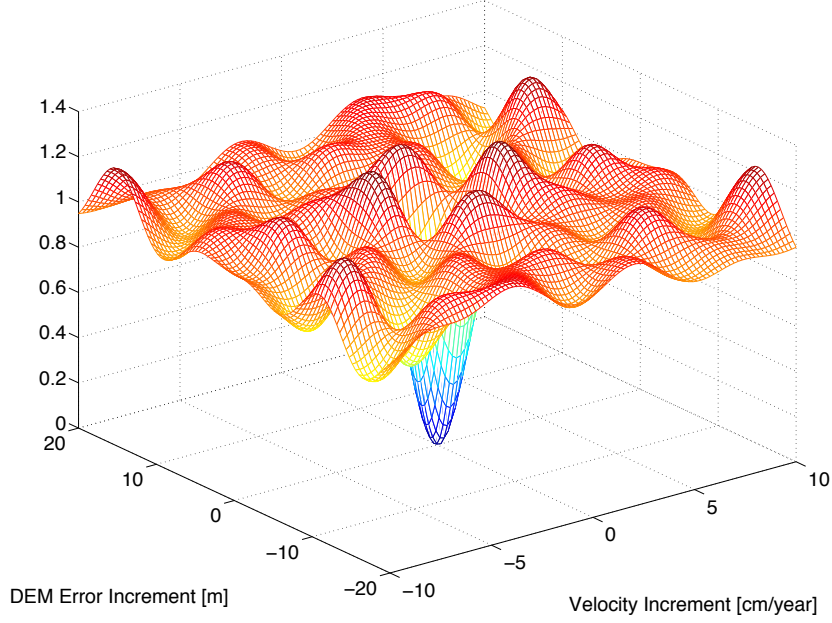
Figure 2.17: Model adjustment function example.

— The shape of the function to minimize depends of the temporal and spatial baselines distribution. The width of the main valley depends on the maximum temporal baseline for the mean displacement dimension and the maximum spatial baseline for the topographic error dimension. Consequently, working with higher baselines trigger narrower valleys in the minimization function. This entails better estimates of the parameters. However, working with high baselines increase the decorrelation effects described in 2.2.4. Hence, a trade of between robustness of the minimization and noise is always present.

— The mean displacement dimension is bound to a periodicity. This is due to the fact that the temporal baselines have a regular sampling, i.e., any temporal baseline is a multiple of a minimum spatial baseline. In fact, the periodicity depends on the minimum temporal baseline difference, ΔT_{min}, as follows

$$\Delta v = \frac{\lambda}{2\Delta T_{min}}. \tag{2.39}$$

Considering this, the maximum mean velocity increment which is free of any ambiguity is

$$v_{max} = \frac{\lambda}{4\Delta T_{min}}. \tag{2.40}$$

Note that this issue is unlikely for the topographic error case, since the spatial

baselines are in principle not linked to any regular sampling. Therefore, replicas are found towards very high values.

As shown both in (2.37) and (2.38), minimization inputs are phases in complex form. Considering this fact, it is possible to obtain good estimates of Δv and $\Delta \varepsilon$ even working with wrapped phases while good distributions of spatial and temporal baselines are available.

The minimization is usually carried out through a two steps approach, which provides a faster and more precise solution:

1. *Brute force minimization*: A coarse sampling of the possible solutions is set a priori, setting certain maximum search values and search steps for both the mean displacement and topographic error increments. A good choice for the mean displacement case is set its maximum considering the value provided by (2.40).

2. *CGM minimization*: The previous step provides a coarse solution. In order to reach the exact solution, the CGM algorithm is applied [29], departing from the solution provided by the brute force minimization. CGM is an efficient way to solve huge linear systems of equations. However, it may also be applied to minimize functions. Locally, the minimum of a bi-dimensional function may be locally approximated by a quadratic function. Then, its gradient may be interpreted as a linear system and thus, solved using the CGM algorithm. The only limitation is to be close enough to the true minimum to avoid local minima. This is achieved through the previous coarse minimization.

After the minimization process, estimates of the mean displacement Δv and the topographic error $\Delta \varepsilon$ for each link in the network are obtained.

At this point, a measurement of the quality of the estimates may be derived. the so-called Linear Model Coherence (LMC) may be defined as

$$\gamma_{lin} = \frac{1}{M} \left| \sum_{i=1}^{M} e^{-j(\Delta \phi_i - \Delta \phi_{lin,i})} \right|. \tag{2.41}$$

This parameter is defined in the interval $[0, 1]$, being 1 when the model perfectly fits the real phase, and tending to zero in the opposite case. The fitting of the model is driven by different factors:

– *Phase noise*: The quality of the estimates depends on the quality of the phase information in the links. This in turn is related to the quality of the pixels candidates selected. Then, this measurement should be heavily correlated to the phase quality estimator used during the pixel candidates selection step. In other words, many of these links should be filtered out previously.

– *Displacement non-linearities*: The model defined in (2.36) accounts only for a linear behavior of the mean displacement, for any acceleration or deceleration in the time domain reduces the fitting of the data to the model.

– *Atmospheric Phase Screen (APS)*: Atmospheric artifacts represent a phase component which in principle does not depend neither on the spatial nor the temporal baselines. Then, from the model fitting point of view, APS acts as a distortion in the data which reduces the linear fitting.

This measurement is useful to reject unreliable links which may compromise the goodness of the further results, as it will be seen in the following.

- **Integration**: The mean displacement rate and topographic error increments obtained in the minimization represent only a relative measurement. It must be integrated in order to retrieve the absolute values for each pixel.

However, previous to any integration, it is advisable to perform a pre-filtering of the links. The objective is to reject the low quality estimations which may lead to bad integrated absolute values. In order to do so, the LMC defined in (2.41) is used. It is hard to quantify the quality value of the LMC, since it depends on may factors. Then, the figure of merit in this case is more related in reduce the number of unreliable links while preserving a certain degree of connectivity.

The integration process is carried out separately for $\Delta \upsilon$ and $\Delta \varepsilon$. It leads to a floating solution, which must be fixed with one or more seed pixels of known values. This seeds must be obtained using external sources of information, such in situ measurements. The use of several seeds is of special interest in the presence of several isolated areas or *clusters*. In this case, each cluster may be treated separately considering its own seed.

The setup of this approach is a linear system, where the solutions are the link increments and the unknowns are the absolute values in each pixel, either for the mean displacement or the topographic error cases. The linear system matrix defines the relation between pixels and increments. Then, it is possible to retrieve the pixel absolute values by inverting the system. This step is done through a CGM approach [29], which provides a very fast and reliable solution, and also is extremely efficient in terms of memory usage.

Finally, it is worth pointing out that during the links pre-filtering process some pixels may be isolated, i.e., they are not connected to any cluster containing a seed. It is advisable to either anchor this pixels with additional seeds or discard them. In the later case, some of the original pixel candidates are filtered out, leading to the final selection of pixels.

2.3.3 Non-linear estimation

After the linear block, estimations of the displacement rate υ and topographic error ε for each pixel selected are obtained. The next part of the PSI processing chain is the so-called *non-linear block*. It aims to estimate the possible remaining non-linear displacement behavior, to obtain the complete displacement time series. It consists of the following steps:

- **Residues calculation**: Considering (2.36) but using absolute values υ and ε instead of the relative ones $\Delta\upsilon$ and $\Delta\varepsilon$, a linear model of the phase of each interferogram $\phi_{lin,i}$ may be defined. By substracting the model from each interferometric phase, the following residual phase may be defined,

$$\phi_{res,i} = \phi_i - \phi_{lin,i} = \phi_{NL,i} + \phi_{APS,i} + \phi_{noise,i} \qquad (2.42)$$

  where i is the interferogram index. The residue may be divided in the next three components:

  - Non-linear component, $\phi_{NL,i}$: Contains the desired information, consisting of the displacements behaviors which do not fit the linear model.

  - APS component, $\phi_{APS,i}$: Contains the principal undesired information, which is related to distortion in the phase caused by atmospheric artifacts.

  - Noise component, $\phi_{noise,i}$: Accounts for any other sources of decorrelation.

  Considering that the later component is totally uncorrelated, the main objective of the non-linear block is to estimate APS component and subtract it form the residues to retrieve the non-linear component.

- **APS estimation**: This step aims to estimate the undesired component in the residuals related to the atmospheric artifacts. The approach followed is based on exploiting the different statistical behavior, in the spatial and the temporal domain, of the non-linear and the APS components [18]. Fig. 2.18 is a graphical depiction of the behavior of both components. As it may be seen, this behavior may be summarized as:

  - Non-linear component: On the one hand, considering a good temporal sampling, the temporal behavior of the ground motion is assumed to be smooth, i.e., without sharp displacement events between correlative acquisitions. On the other hand, the spatial behavior of ground motion has no a priori restriction, and it is assumed that may be characterized by fast gradients in the spatial domain. In other words, the non-linear phase component can be assumed to present a low-pass behavior in time and a certain high-pass behavior in space.
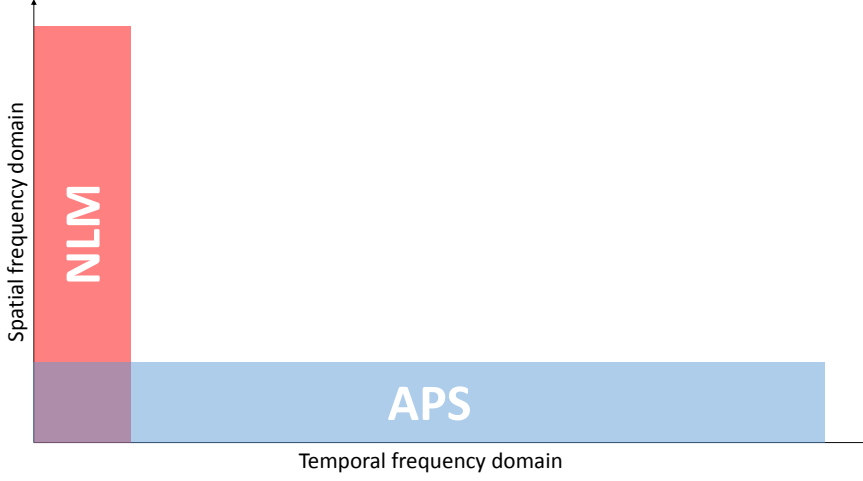
Figure 2.18: Espectral distibution of Non-linear motion and APS.

  – APS component: Atmospheric artifacts are assumed to present a totally random behavior in the temporal domain, since the atmospheric conditions during each acquisition are totally uncorrelated. Meanwhile, the spatial behavior is assumed to be smooth, since close locations are bound to have similar atmospheric conditions. In general, a correlation window of 1 km is assumed to give a good characterization of the APS component [18]. Summarizing, it presents a certain high-pass behavior in time and a low-pass behavior in space.

Considering the previous statistical behavior, the APS component estimation is carried out using an spatio-temporal filtering strategy. The procedure is described in the following steps:

1. *Spatial Low-Pass (SLP) filtering of the residues*: A low pass filtering or smoothing of the phase residue in each interferogram is carried out. An averaging sliding window size according to the spatial correlation is considered, in general 1 km. The objective is to minimize the non-linear component in the resulting filtered phase. Obviously, non-linear motion behaviors wider than the expected APS spatial correlation are also included in the resulting phase. Then, the SLP residues may be described as

$$\phi_{res-SLP,i} = \phi_{NL-SLP,i} + \phi_{APS,i} \qquad (2.43)$$

   where $\phi_{NL-SLP,i}$ accounts for the non-linear component with low pass behavior and $\phi_{APS,i}$ should contain all the atmospheric component considering its spatial statistics. Then, in the presence of wide area non-linear motion, the spatial filtering is not able to totally separate the APS from the non-linear component. The next steps try to tackle this issue.

39

2. *Phase temporal decomposition*: In order to go on with the statistical separation of the APS and the non-linear components, a temporal filtering of the SLP residues must be carried out. Unfortunately, the data-set to filter is interferometric, i.e., the phase information is a relation between temporal acquisitions, and not the acquisitions themselves. In order to be able to apply a temporal filter, a temporal decomposition and ordering of the interferometric information is mandatory. To do so, the Singular Value Decomposition (SVD) algorithm [30] may be applied to obtain the equivalent SLP residue for each acquisition.

   The first step, in order to preserve the temporal consistence of the phase information, is to unwrap each SLP residue. This step should be easily done by any simple 2D phase unwrapping algorithm, since the SLP filtering also reduces the original phase noise component. Moreover, each interferogram is bound to a certain unknown global phase offset which must be estimated and compensated for. The offset estimation is done, assuming a general stability of the area under monitoring, detecting the main contribution in the phase histograms. After this setup, the SLP residue for each acquisition may be accurately retrieved using the SVD algorithm.

3. *Temporal Low-Pass (TLP) filtering of the SLP residues*: Once the SVD is applied, the temporal ordered dataset of SLP residues is ready to be filtered in the temporal domain. The TLP filtering followed by CPT is based on a triangular window approach. This way, samples farther in time are less significant in the averaging. The temporal sensitivity provided by the triangular filter is a positive feature, since the temporal sampling in SAR data-sets might not be regular.

   The TLP filtering of the SLP residues provides with a general low-pass estimation, both in the temporal and the spatial domains, of the non-linear displacement. Subtracting this component it is possible to isolate the APS component for each acquisition, which has a low-pass behavior in time and a high pass behavior in space.

4. *Interferometric APS reconstruction*: This step simply obtains the APS component for each interferogram, combining the APS available for each acquisition.

- **Displacement time series generation**: Once the APS is removed from the residues, the non-linear component is obtained applying again the SVD approach. Finally, the full deformation time series is obtained adding the linear and the non-linear component for each pixel selected.

2.3.4   Post-processing

The output of the CPT algorithm consists of the displacement time series related to each selected pixel. All this information is given in the SAR coordinate system, related to a certain range and azimuth position. Moreover, the displacement measure is given in the LOS direction. In order to adequate this information in a more suitable delivery form, the next post-processing steps are followed

- **Geocoding**: This step applies the process described in 2.1.5, in order to transform the SAR reference system to any standard geographical coordinates system. Usual choices are angular reference (Latitude, Longitude) or planar reference (UTM coordinates) systems. It is important to mention that the topographic error obtained during the linear estimation step (see 2.3.2) is used to refine the geolocalization of each PS.

- **Projection**: Since the radar sensitivity is in LOS, the displacement information is initially given in this direction. In terms of meaningfulness, LOS is an arbitrary direction, so it almost never represents the real displacement direction. In any case, it can be easily characterized since the orbital deployment is perfectly known. In many cases, the real displacement direction may be known or at least assumed a priori. For instance, when observing a subsidence phenomenon, the real displacement is supposed to be in vertical direction. In those cases, assuming that the LOS measurement ρ_{LOS} is just a component of the total displacement ρ_{tot}, the later may be derived as

$$\rho_{tot} = \frac{\rho_{LOS}}{\cos\left(\delta_{proj}\right)} \tag{2.44}$$

  where δ_{proj} is the angular difference between the LOS direction and the assumed real direction of the displacement. This angle can be easily derived from the incidence angle θ. Typical cases of real orientation are vertical, horizontal or down-slope, when monitoring landslides.

2.4   SAR Polarimetry

This section reviews some basics in SAR polarimetry, in order to understand the treatment of PolSAR data in the framework of PSI carried out in this thesis.

All the theory behind this discipline is based on the concept of wave polarization, which defines the electromagnetic state of the propagated wave. PolSAR systems are able to retrieve different combinations of emitted/received configurations, known as polarimetric channels. Each channel turns to be sensitive to different characteristics of the illuminated area. The following sections will briefly describe the most important concepts and algorithms which are used in this work.

2.4.1 Wave polarization

Considering a monochromatic plane wave, its electric field propagating in the $\overrightarrow{\mathbf{z}}$ direction of a Cartesian system may be defined as

$$\overrightarrow{\mathbf{E}}\left(z,t\right) = \left[\begin{array}{c} E_x \\ E_y \end{array}\right] = \left[\begin{array}{c} E_{0x}\cos\left(\omega t - kz + \delta_x\right) \\ E_{0y}\cos\left(\omega t - kz + \delta_y\right) \end{array}\right] \tag{2.45}$$

where E_{0x} and E_{0y} are the amplitude of the electric field in $\overrightarrow{\mathbf{x}}$ and $\overrightarrow{\mathbf{y}}$ respectively, k is the wave number and δ_x and δ_y are parameters which define the polarization state. Different polarization states may be defined by the shape that follows the tip of the electric field in the **xy** plane as the wave propagates. In fact, the polarization state depends only on $\delta = \delta_x - \delta_y$, which lead to three different generic states:

- **Linear polarization**: The particular case when $\delta = 0$. The wave is defined by a sinusoidal function, propagating in a plane tilted a certain angle ϕ with respect to $\overrightarrow{\mathbf{x}}$. In the propagation axis, the tip of the electric field defines a line confined in the plane.

- **Circular polarization**: The case when $\delta = \frac{\pi}{2} + n\pi$ and $E_{0x} = E_{0y}$, where n is any integer number. The wave describes a perfect circumference in the **xy** plane as it propagates.

- **Elliptic polarization**: This is the general case, where any of the previous conditions are accomplished. The wave describes an ellipse as it propagates.

Fig. 2.19 represents the polarization ellipse, an intuitive way to depict the curve described by the electric field. This geometric form is defined by the next parameters:

- A: The ellipse amplitude, which depends on the electric field amplitudes as

$$A = \sqrt{E_{0x}^2 + E_{0y}^2} \tag{2.46}$$

- ϕ: The ellipse orientation, which is the angle between $\overrightarrow{\mathbf{x}}$ and the ellipse major axis. The range of possible values is defined in the interval $[-\pi/2, \pi/2]$. A relation with the electric field parameters may be established through

$$\tan 2\phi = 2\frac{E_{0x}E_{0y}}{E_{0x}^2 - E_{0y}^2}\cos\delta \tag{2.47}$$

- τ: The ellipse aperture or ellipticity, which is defined in the interval $[0, \pi/4]$. This parameter is strongly related to the generic polarization states, since $\tau = 0$ provides a linear polarization and $\tau = \pi/4$ becomes a circular polarization. It relates with the electric field parameters through

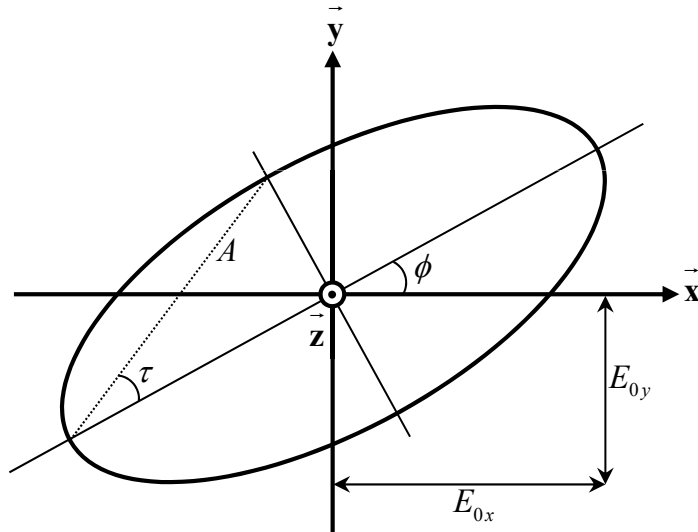$$|\sin 2\tau| = 2\frac{E_{0x}E_{0y}}{E_{0x}^2 + E_{0y}^2}|\sin\delta| \tag{2.48}$$

Figure 2.19: Polarization ellipse.

At this point arises the definition of the *Jones vector*, which aims to describe the wave polarization in a simplified expression. The Jones vector, expressed both in the electric field and the polarization ellipse parameters, is defined as

$$\underline{\mathbf{E}} = \left[\begin{array}{c} E_{0x}e^{j\delta_x} \\ E_{0y}e^{j\delta_y} \end{array} \right] = Ae^{j\alpha} \left[\begin{array}{cc} \cos\phi & -\sin\phi \\ \sin\phi & \cos\phi \end{array} \right] \left[\begin{array}{c} \cos\tau \\ j\sin\tau \end{array} \right] \tag{2.49}$$

where α is an absolute phase term. Some particular canonical states of the Jones vector are resumed in Table 2.1.

2.4.2 Scattering matrix and scattering vector

Considering an emitted wave over an scenario and its respective back-scattered wave, the *radar cross section* determines the power balance between them. It may be defined as

$$\sigma = 4\pi r^2 \frac{\left| \overrightarrow{\mathbf{E}}_S \right|^2}{\left| \overrightarrow{\mathbf{E}}_I \right|^2} \tag{2.50}$$

where $\overrightarrow{\mathbf{E}}_I$ and $\overrightarrow{\mathbf{E}}_S$ are the incident and scattered electric fields respectively and r is the target to sensor distance. This definition is valid for deterministic scatterers.

In the case of distributed targets, the *scattering coefficient* or *sigma-naught* is defined

43

Polarization state	Unitary Jones vector	ϕ	τ
Linear Horizontal	$\begin{bmatrix} 1 \\ 0 \end{bmatrix}$	0	0
Linear Vertical	$\begin{bmatrix} 0 \\ 1 \end{bmatrix}$	$\frac{\pi}{2}$	0
Linear 45°	$\frac{1}{\sqrt{2}} \begin{bmatrix} 1 \\ 1 \end{bmatrix}$	$\frac{\pi}{4}$	0
Linear -45°	$\frac{1}{\sqrt{2}} \begin{bmatrix} 1 \\ -1 \end{bmatrix}$	$-\frac{\pi}{4}$	0
Left Circular	$\frac{1}{\sqrt{2}} \begin{bmatrix} 1 \\ j \end{bmatrix}$	$\left[-\frac{\pi}{2}...-\frac{\pi}{2}\right]$	$\frac{\pi}{4}$
Right Circular	$\frac{1}{\sqrt{2}} \begin{bmatrix} 1 \\ -j \end{bmatrix}$	$\left[-\frac{\pi}{2}...-\frac{\pi}{2}\right]$	$-\frac{\pi}{4}$

Table 2.1: Jones vectors for some canonical polarization states

instead as

$$\sigma^0 = \frac{4\pi r^2}{A_0} \frac{\left\langle \left| \overrightarrow{\mathbf{E}}_S \right|^2 \right\rangle}{\left| \overrightarrow{\mathbf{E}}_I \right|^2} \tag{2.51}$$

where $\left\langle \left| \overrightarrow{\mathbf{E}}_S \right|^2 \right\rangle$ stands for the combined scattered electric field of all the scatterers over an illuminated area A_0. Both parameters depend on many factors, among them the wave polarization. Let's consider now the Jones vectors characterizing the incident and scattered fields, $\underline{\mathbf{E}}_I$ and $\underline{\mathbf{E}}_S$. The relation between them can be established as

$$\underline{\mathbf{E}}_S = \frac{e^{-jkr}}{r}\mathbf{S}\underline{\mathbf{E}}_I = \frac{e^{-jkr}}{r} \begin{bmatrix} S_{11} & S_{12} \\ S_{21} & S_{22} \end{bmatrix} \underline{\mathbf{E}}_I \tag{2.52}$$

where **S** is the so-called *scattering matrix*, composed by the elements S_{ij} known as the *complex scattering coefficients*. On the one hand, the elements on the diagonal are known as the *copolar* terms, since relate incident and scattered fields at the same polarization state. On the other hand, the off-diagonal elements are the *cross-polar* terms, which relate fields at orthogonal polarization states. The remaining term accounts for the propagation effect in the amplitude and the phase.

Orbital SAR systems are usually in a monostatic configuration, i.e., transmitter and

receiver are located in the same position. In this case, both cross-polar terms are equal for the reciprocity theorem, so the polarimetric information relies only on three terms: the two copolar and the crosspolar complex scattering coefficients. Then, considering the commonly used *lexicographic basis*, based on the horizontal and vertical linear polarization states, the scattering matrix for a monostatic case may be rewritten as

$$\mathbf{S}_{HV} = \begin{bmatrix} S_{hh} & S_{hv} \\ S_{hv} & S_{vv} \end{bmatrix}. \tag{2.53}$$

The same information may be given in vector form, the so called *scattering vector* $\mathbf{k}$, as

$$\mathbf{k}_{HV} = \begin{bmatrix} S_{hh}, \sqrt{2}S_{hv}, S_{vv} \end{bmatrix}^{T} \tag{2.54}$$

where ^{T} stands for the vector transposition operator. Another basis usually defined is the *Pauli basis*, which is of particular interest since its terms may be easily related to canonical physical geometries. Its scattering vector is given by

$$\mathbf{k}_{Pauli} = [P_1, P_2, P_3] = \frac{1}{\sqrt{2}}[S_{hh} + S_{vv}, S_{hh} - S_{vv}, 2S_{hv}]^{T}. \tag{2.55}$$

Note that the different constant terms in the late expressions are introduced to preserve the total power invariance. Each component of the Pauli decomposition have the next characteristics:

- **P1**: The back-scattering is related to odd bounce scattering. The most significant cases are the specular scattering (1 reflection) and the trihedral like scattering (3 reflections).

- **P2**: The back-scattering is related to even bounce scattering. The most significant case is the dihedral like scattering (2 reflections), such as the ground to wall reflection.

- **P3**: The back-scattering is usually related to volumetric scattering, mostly associated to vegetation, since it depends on the penetration of the wave on a medium where it has multiple reflections. However, it is also sensitive to other scattering processes, such as the double bounce reflection to a non-orthogonal to LOS surface [31]. A clear example is a building which is not oriented in the LOS direction.

2.4.3 Generalized scattering vector and interferometric coherence

Consider the scattering vector $\mathbf{k}$ corresponding to a certain resolution cell or pixel in a PolSAR acquisition. The corresponding pixel in a generic SAR image μ, usually addressed as *scattering coefficient*, may be defined as

$$\mu = \boldsymbol{\omega}^{H}\mathbf{k} \tag{2.56}$$

where $\boldsymbol{\omega}$ is a unitary complex projection vector and ^{H} is the complex transposition. The new image, which is the result of applying this projection to all the possible pixels, may be understood as a weighted combination of all the channels forming the PolSAR acquisition. Thus, this combination offers sensitivity to different scattering mechanisms depending on $\boldsymbol{\omega}$.

Considering two different PolSAR acquisitions, defined by the scattering vectors $\mathbf{k}_i$ and $\mathbf{k}_j$ respectively, the following matrices may be defined,

$$\begin{aligned}
\mathbf{T}_{ii} &= \left\langle \mathbf{k}_i \mathbf{k}_i^H \right\rangle \\
\mathbf{T}_{jj} &= \left\langle \mathbf{k}_j \mathbf{k}_j^H \right\rangle
\end{aligned} \tag{2.57}$$

where $\langle . \rangle$ stands for an spatial averaging of several pixels or multi-look. They are addressed as *covariance matrices*, when $\mathbf{k}$ is given in the lexicographic basis or *coherency matrices*, when using the Pauli basis. For fully-polarimetric data, the size of the matrices is 3x3 while for the dual-polarimetric case it is 2x2, since one of the complex scattering vectors is missing in $\mathbf{k}$. This matrices contain the polarimetric information related to each single PolSAR acquisition. The polarimetric information between acquisitions, which in fact provides also interferometric information, is defined as

$$\boldsymbol{\Omega}_{ij} = \left\langle \mathbf{k}_i \mathbf{k}_j^H \right\rangle . \tag{2.58}$$

This matrix is known as *inteferometric matrix*, an contains both the polarimetric and the interferometric correlations between acquisitions i and j.

Taking into account the basic acquistions $\mathbf{k}_i$ and $\mathbf{k}_j$ and applying (2.56), two new generic SAR images $\mu_i = \boldsymbol{\omega}_i{}^H \mathbf{k}_i$ and $\mu_j = \boldsymbol{\omega}_j{}^H \mathbf{k}_j$ are obtained. Now, considering the coherence calculation described in (2.31), the coherence between $\boldsymbol{\mu}_i$ and $\boldsymbol{\mu}_j$ may be defined as [32]

$$\hat{\gamma}_{ij} = \frac{\left\langle \mu_i \mu_j^* \right\rangle}{\sqrt{\left\langle \mu_i \mu_i^* \right\rangle \left\langle \mu_j \mu_j^* \right\rangle}} = \frac{\left\langle \boldsymbol{\omega}_i^H \mathbf{k}_i \mathbf{k}_j^H \boldsymbol{\omega}_j \right\rangle}{\sqrt{\left\langle \boldsymbol{\omega}_i^H \mathbf{k}_i \mathbf{k}_i^H \boldsymbol{\omega}_i \right\rangle \left\langle \boldsymbol{\omega}_j^H \mathbf{k}_j \mathbf{k}_j^H \boldsymbol{\omega}_j \right\rangle}} . \tag{2.59}$$

At this point, two different assumptions are made in order to avoid introducing inconsistent polarimetric terms:

- The values of $\boldsymbol{\omega}_i$ and $\boldsymbol{\omega}_j$ must be preserved for all the pixels involved in the spatial averaging, in order to combine pixels in the same polarimetric configuration. Then, they are not affected by the spatial averaging in (2.59), or in other words, they can be applied after the averaging computation.

- In order to preserve the phase center of the scatterers along the acquisitions, for DInSAR purposes, the values of the weight vectors must be preserved for the whole PolSAR data-set. Then, it must be accomplished that $\boldsymbol{\omega}_i = \boldsymbol{\omega}_j = \boldsymbol{\omega}$.

Considering the previous assumptions, an taking into account the expressions in (2.57) and (2.58), the generic coherence may be rewritten as

$$\hat{\gamma}_{ij} = \frac{\boldsymbol{\omega}^H \boldsymbol{\Omega}_{ij} \boldsymbol{\omega}}{\sqrt{\left(\boldsymbol{\omega}^H \mathbf{T}_{ii} \boldsymbol{\omega} \right) \left(\boldsymbol{\omega}^H \mathbf{T}_{jj} \boldsymbol{\omega} \right)}} . \tag{2.60}$$

At this point, $\boldsymbol{\omega}$ may be tuned up in order to optimize the coherence value, and thus, the phase quality. As seen in further sections, the coherence optimization algorithms aim to find the $\boldsymbol{\omega}$ which provides the maximum coherence value.

2.4.4 Polarimetric basis transformation

Orbital fully-polarimetric data is usually given in the lexicographic basis, described by the scattering matrix defined in (2.53). Given any orthogonal basis, such as the lexicographic, any possible basis may be obtained through

$$\mathbf{S}_{AB} = \mathbf{U}_2^T \mathbf{S}_{HV} \mathbf{U}_2 \tag{2.61}$$

where the matrix $\mathbf{U}_2$ is defined by the polarization ellipse parameters ϕ and τ and the unknown phase term α as

$$\mathbf{U}_2 = \left[\begin{array}{cc} \cos\phi & -\sin\phi \\ \sin\phi & \cos\phi \end{array} \right] \left[\begin{array}{cc} \cos\tau & j\sin\tau \\ j\sin\tau & \cos\tau \end{array} \right] \left[\begin{array}{cc} e^{j\alpha} & 0 \\ 0 & e^{-j\alpha} \end{array} \right]. \tag{2.62}$$

The term α is usually obviated since it does not carry any polarimetric nor interferometric information. A matrix $\mathbf{U}_3$ may be defined, in order to apply the polarimetric basis transformation directly to the scattering vectors and the polarimetric covariance and interferometric matrices, as

$$\mathbf{k}_{AB} = \mathbf{U}_3 \mathbf{k}_{HV}$$

$$\{\mathbf{T}, \boldsymbol{\Omega}\}_{AB} = \mathbf{U}_3 \{\mathbf{T}, \boldsymbol{\Omega}\}_{HV} \mathbf{U}_3^{-1} \tag{2.63}$$

where $^{-1}$ stands for the inverse of a matrix and $\mathbf{U}_3$ is defined as

$$\mathbf{U}_3 = \left[\begin{array}{ccc} 1 & 0 & 0 \\ 0 & \cos 2\phi & \sin 2\phi \\ 0 & -\sin 2\phi & \cos 2\phi \end{array} \right] \left[\begin{array}{ccc} \cos 2\tau & 0 & j\sin 2\tau \\ 0 & 1 & 0 \\ j\sin 2\tau & 0 & \cos 2\tau \end{array} \right] \tag{2.64}$$

where the component matrix related to the absolute phase term α is not represented to ease the notation.

2.5 Conclusions

The objective of this chapter is to provide the minimum theoretical background for the following chapters of this thesis.

The main characteristics of the SAR instrument have been described, to understand the nature of the data acquired. The main capabilities of both the instrument and the orbital deployment are highlighted.

47

The traditional applications of SAR, which are InSAR and DInSAR, are put forward. Here, the sensitivity of interferometric phase to topography and terrain displacement is presented. The limitations of these techniques are described, evidencing the need for more advanced approaches.

This serves as a perfect introduction to PSI multi-temporal analysis of SAR data-sets. All the steps to precisely retrieve the underlying topography and motion during the data-set time span are described. The strategies to overcome the limitations of traditional techniques are presented.

Last but not least, a brief introduction in SAR Polarimetry is included. This section will ease the comprehension of the different polarimetric manipulation of data carried out in the core chapters of this thesis.

3

CHAPTER 3

DATA-SET DESCRIPTION

T HIS chapter describes the PolSAR data-set used to show the benefits of the techniques developed and used in the course of this thesis. The principal characteristics of Radarsat-2 satellite and the specific mode used are put forward. A brief description on the stack of images used and the temporal span covered is given.

A brief description of the site is also provided, and the possible terrain displacement which may be present is pointed out. Several areas of interest have been selected to present the results, which are also described with more detail.

Figure 3.1: Approximate area of monitoring over Barcelona. The approximate geographic location is 42° 22' N, 2° 7' E.

3.1   Site description

The data-set used in this work has been acquired over the city of Barcelona. The capital of Catalonia is the largest metropolitan area on the shores of the Mediterranian Sea, reaching a population over 1.6 million people on the city itself, but extending to over 4.7 million people in the whole urban area.

Barcelona is under an important construction activity, including several underground infrastructures. Some of them affect or threaten several areas in the city. For instance, the tunnel that connects the High Speed Train (AVE) line with France passes very close to the Sagrada Familia cathedral. Also the new underground line (L9) that connects the city with the airport could generate subsidence in different parts of the urban area.

A block in El Carmel neighborhood collapsed in 2005 due to a new underground line. Also building damages caused by the AVE tunnel in the South of the city were detected.

This triggered a general alarm, which made evident the need of a large scale monitoring of these activities. Moreover, several important infrastructures near the shore, such as the airport and the harbor facilities, are known to present subsidence. Fig. 3.1 shows the approximate area under monitoring.

3.1.1 Areas of interest

This section describes the different areas selected over Barcelona where the subsidence results will be presented. In the following a brief description of each zone is provided, giving the main characteristics of the location and highlight the main causes for any possible terrain displacement.

3.1.1.1 Barcelona-El Prat Airport

The Barcelona-El Prat airport, located near the El Prat de Llobregat city, is one of the main hubs in Europe. For instance, the number of passengers was more than 37.5 million passengers during 2014. In June 2009 the capacity of the airport increased when the new T1 terminal was inaugurated. It was quite an ambitious and complex project, since the facilities are located over the Llobregat river delta. The construction was planned to assume a certain settlement due to the soft material in its base. This fact makes it a perfect candidate to present subsidence. The areas of interest included around the airport facilities are:

- **Terminal T1:** The new terminal building and its surroundings is obviously the main area observed, since it is the principal zone where subsidence is expected. See its location in Fig. 3.2, labeled as A.

- **Access road:** This area has undergone a high construction activity, mostly related to the airport expansion but also some works regarding the new Barcelona metro line (L9). The Area Of Interest (AOI) is labeled as B in Fig. 3.2.

3.1.1.2 Port de Barcelona

El Port de Barcelona is one of the most active seaports in the Mediterranean Sea. It covers a wide extension of Barcelona seashore, reaching almost an area of 8 km². Many facilities in the port are constructed over land reclaimed from the sea, which are subject to present subsidence. The areas of interest shown in the results are:

- **Breakwaters:** The main breakwaters, which are the outermost structure in the harbor, are known to present relevant motion [33].

Figure 3.2: General overview of Barcelona-El Prat airport. The areas of interest selected are the terminal T1 (A) and the access road (B).

- **Energy Bay:** This bay, resembling a peninsula and entirely constructed over more than 1,5 km^2 of land reclaimed to the sea, is used as the oil loading/storing area, and also contains a thermal power plant.

- **W Barcelona:** Popularly known as "Hotel Vela", this characteristic building placed over a small expansion of the harbor was built in 2009. Due to its location a certain settlement of the building is presumed.

3.1.1.3 L9 metro line

The L9 metro line, currently under construction, will become the longest metro line in Europe, with more than 47 km in length. This subway infrastructure connects Barcelona with the airport, crossing in its way several sections of urban area. The specific region of interest is a track of the line which was under tunneling work when the SAR monitoring was performed, specifically between Hospital de Sant Pau and Plaça Lesseps. This is the location of one of L9 stations under construction, in Plaça Sanllehy, which will be one of the hubs of the Barcelona metro network. Its characterized by a big well of almost 100

Figure 3.3: General overview of El Port de Barcelona. The areas of interest selected are the breakwaters (C), the Energy Bay (D) and W Barcelona hotel (E).

m deep. Fig. 3.4 gives an overview of the line and the construction of the station. The tunneling work is assumed to cause certain settlement over the upper surface of the city.

53
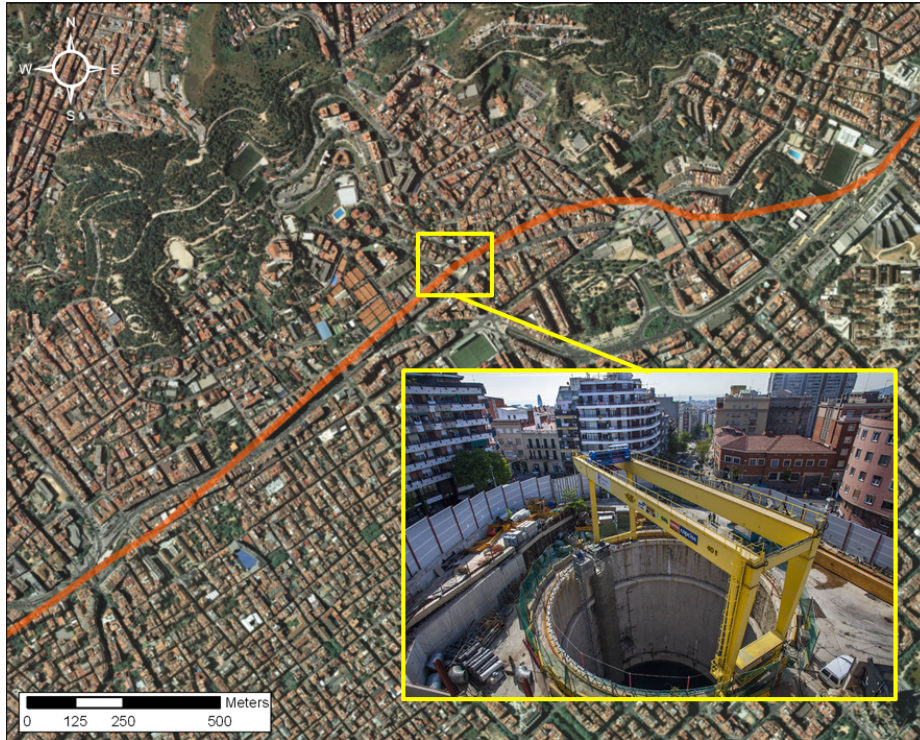
Figure 3.4: General overview of the L9 metro line selected. The area of interest is located in Sanllehy square.

3.2 PolSAR data-set characteristics

The PolSAR data-set used in this work was acquired by the satellite Radarsat-2 from the Canadian Space Agency (CSA), in the framework of the scientific project SOAR-EU 6779. This satellite works on a near-polar sun-synchronous Low Earth Orbit (LEO), with an altitude of 798 km over the Earth surface. The SAR sensor on-board works at C band and with fully-polarimetric capabilities. The actual data-set is acquired in strip map mode, concretely with the Fine QuadPol mode. The principal characteristics of the system are shown in Table 3.1.

The potential PolSAR data-set was composed of 39 acquisitions, from 20th January 2010 to 20th July 2012. Unfortunately, one of the programmed acquisition failed. Moreover, three more acquisitions do not accomplish the baseline requisites to be included in the DInSAR processing. Finally, the acquisition taken on 9th March 2010 is rejected for phase quality reasons, since an unlikely heavy event of snowfall took place in that date [34]. The processing has been carried out with a total of 34 acquisitions. Table 3.2 summarizes all this information.

Parameter	Value
Carrier frequency	5.4 GHz
Wavelength	5.54 cm
Sampling frequency	31.7 MHz
PRF	1.38 kHz
Range Bandwidth	30.0 MHz
Azimuth Bandwidth	0.9 kHz
Pixel size(range x azimuth)	4.73 x 4.82 m
Scene size	25 x 25 km
Incidence angle	29º
Acquisition	Descending Right-looking
Polarimetric channels	HH, HV, VH, VV

Table 3.1: System and acquisition parameters

Date	Comment	Date	Comment
2010/01/20		2011/05/15	
2010/02/13		2011/06/08	Rejected - Baseline
2010/03/09	Rejected - Snowfall	2011/07/02	
2010/04/02		2011/07/26	
2010/04/26		2011/08/19	
2010/05/20		2011/09/12	
2010/06/13		2011/10/06	
2010/07/07		2011/10/30	
2010/07/31		2011/11/23	
2010/08/24		2011/12/17	
2010/09/17	Rejected - Baseline	2012/01/10	Not acquired
2010/10/11		2012/02/03	
2010/11/04		2012/02/27	
2010/11/28		2012/03/22	
2010/12/22		2012/04/15	
2011/01/15		2012/05/09	Rejected - Baseline
2011/02/08		2012/06/02	
2011/03/04		2012/06/26	
2011/03/28		2012/07/20	
2011/04/21			

Table 3.2: List of PolSAR acquisitions. Date is given in yyyy/mm/dd.

The combination of the PolSAR acquisitions has produced a total of 224 valid interferograms with enough phase quality to extract good measurements of topographic error and displacement. Fig. 3.5 shows a graphical representation of the interferogram selection, where the nodes are the acquisitions and the links are the interferograms. Only
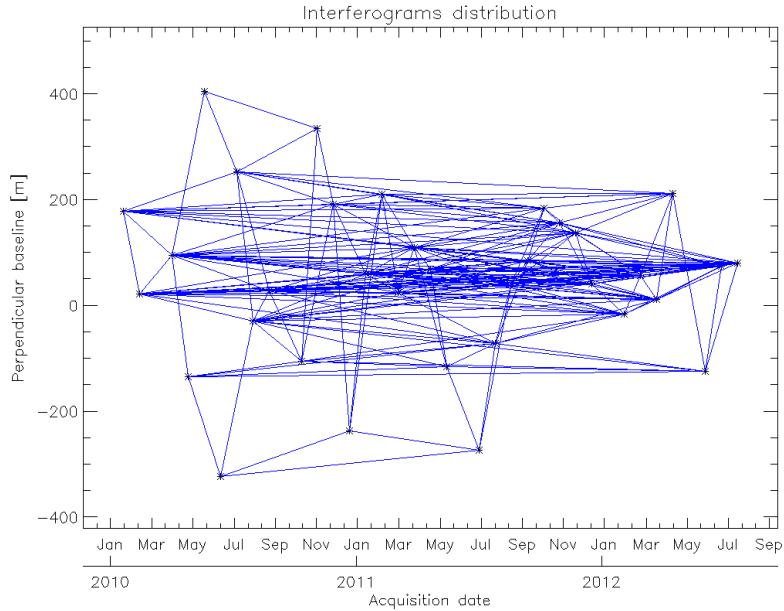
Figure 3.5: Interferograms distribution in the spatial/temporal baselines space. Doppler is obviated.

the spatial and temporal 2D representation is provided, since the doppler difference of all interferograms is minimal.

The inteferometric chain described in 2.13 has been applied to the PolSAR data-set. Each step has been carried out for each polarimetric channel of the PolSAR acquisitions. Mind that some procedures, such as the derivation of the offsets in the registration or the synthetic interferogram generation are obtained only for one case and applied directly to the rest of polarimetric channels.

The final product of the interferometric chain consists of the following items:

- Registered SLCs for each polarimetric channel.

- Interferometric phases for each polarimetric channel.

- Coherency matrices in several multi-looks.

Fig. 3.6 shows an RGB composite of the Pauli channels, a usual way to provide a visual representation of PolSAR data. A 5x3 multi-look has been applied as well as an horizontal flip to better match the geometry in Fig. 3.1. As it may be appreciated, the urban area is

56

Figure 3.6: Pauli RGB representation of Barcelona. Composite of channels P1 (Blue), P2 (Red) and P3 (Green).

an heterogeneous combination of the responses in the different channels. This fact hints the potential of PolSAR data to better characterize the area under monitoring.

4

Polarimetric basis results combination

Polarimetric SAR data, either dual or fully polarimetric, provides a higher degree of information than the single polarimetric one. Each channel in a PolSAR acquisition is in fact a conventional SAR image, but sensitive to different scatterers within the scene. Thus, the displacement information extracted from each channel separately is related to different targets in the same scenario. This chapter describes several criteria in order to exploit this extra information, considering the different treatment of the data carried out during the application of the DInSAR techniques. The pixel candidates selection considered, and more specifically, working at full-resolution or applying a spatial average or multi-look, defines the different approaches in the combination of displacement results.

4.1 Pixel selection criteria considerations

In 2.3.1, three different multi-temporal phase quality estimators are described: Coherence stability, dA and TSC estimators. Among the different characteristics of each one, the coherence stability estimator implies an spatial averaging of the SAR data-set. For the purposes of this chapter, from now on it is addressed as a low resolution estimator, while the amplitude dispersion and the TSC are considered as high resolution estimators.

The availability of a PolSAR data-set provides sensitivity to different geometric characteristics in the illuminated scene. Then, the pixel selection is bound to lead to different pixel candidates for each polarimetric channel. At this point, whether working at low or high resolution implies the use of different criteria to exploit all the displacement measurements obtained. In the following sections, the specific considerations for each estimator are put forward.

4.1.1 Low resolution polarimetric basis combination

This section describes the approach followed to combine the different polarimetric basis results in the low resolution case. The coherence stability estimator is ideally meant to be applied over scenarios composed by distributed targets, where statistically similar scatterers are combined in the spatial averaging. Unfortunately, this kind of scenario is rather uncommon due to the presence of deterministic targets, usually associated with man-made structures, but also caused by certain natural sources, such as rock outcrops. The most typical example of these heterogeneous distributions are the urban areas. Nonetheless, the application of the coherence estimator in these cases is equally valid, since deterministic targets turn to have a high coherence value due to their stability and significance inside the resulting spatial averaged pixel. This fact may be assumed from the coherence estimator expression in (2.31). A certain pixel n behaving like a stable deterministic target is usually associated with a high amplitude. Then, its relevance in the resolution cell and thus in the coherence estimation is high.

Let's consider an heterogeneous scenario, formed by a random distribution of deterministic and distributed targets. The loss in resolution implies that the resulting pixels cover a larger area than the one provided by the original SAR data. This bigger cell is bound to contain a certain geometric diversity, i.e., several kinds of geometries included. This fact favors the sensitivity in the different polarimetric channels available.

Therefore, a high spatial coincidence is expected during the pixel selection, i.e., the same pixel is probably selected in most of the polarimetric channels available. Mind also that the multi-look reduces the sampling over the scene, since the resulting number of pixels is lower. This automatically favors the final pixel coincidence.

The data resolution loss also determines the kind of phenomenon bound to be detected.

Since the averaged pixel represents a wider area, the displacement detected should be related to a spatially extensive phenomenon. This kind of displacement should not depend on the polarimetric channel, since it is presumed to be the same for all the targets in the area.

Considering the previous statements, the displacement detected in spatially coincident averaged pixels from different polarimetric channels is redundant and can be useful to reduce the noise of the measure, since they can be considered as different realizations of the same experiment. Hence, the ideal case would be a total coincidence of selected pixels.

4.1.2 High resolution polarimetric basis combination

This section describes the approach followed to combine the different polarimetric basis results in the high resolution case. Among the two options available, acdA and TSC, the former has been selected for the present study. Since the number of acquisitions in the data-set fulfills the requirements of the dA estimator, this way we avoid the resolution loss by a factor of 2 in range inherent to the TSC estimator.

Since the targets detected are point-like scatterers and considering the resolution of the last generation satellites, in the order of meters, the scattering of each resolution cell can be assumed to be caused by a few dominant targets. Furthermore, the backscattering level in each polarimetric channel is strongly related to the geometry of the objects inside each pixel. This way, it is possible to distinguish targets within a resolution cell due to its physical and geometric charateristics.

In this line, another consideration related to the SAR acquisition system distortions (see section 2.1.1) arises. Layover and foreshortening cause that spatially separated objects may lie on the same resolution cell in the slant-range coordinate system. Thus, the combination of the topographic error measurement derived from the DInSAR process and geocoding techniques, it is possible to separate these two scatterers in the ground-range plane if their geometric characteristics are different.

PSI techniques provide a measurement of terrain displacement and topographic error for each polarimetric channel. The latter is related to the reference DEM used to extract the topographic component of the differential phase of each interferogram, see 2.2.3. To easily understand the rationale behind the approach described in this section, it is assumed that the DEM models perfectly the underlying terrain in the scene. With this consideration, the topographic error is exclusively related to the overground elements, such as buildings, vegetation, or any possible outcrop. In other words, the height measurement is related to the different targets detected by each polarimetric channel. Considering a certain resolution cell over the PolSAR acquisition, its contribution in each channel may be caused by different scatterers, each one located at a different height but belonging to the same cell due to the SAR distortions. Therefore, these targets may be separated in
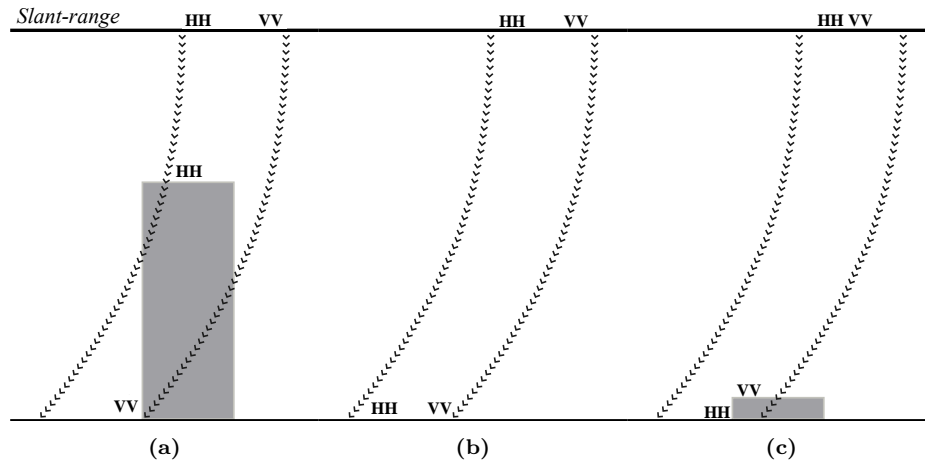
Figure 4.1: High resolution casuistry between scatterers lying in the same resolution cell. In the example, there are two scatterers detected in the same cell with HH and VV channels. (a) high height difference, (b) no height difference and (c) insignificant height difference.

ground range, knowing its relative height, through the geocoding techniques described in 2.1.5. On the contrary, scatterers that belong to the same resolution cell and have similar height must be spatially closer. Fig. 4.1 describes all these cases.

The case reflected in Fig. 4.1a describes the situation where two different scatterers, detected in different polarimetric channels, are placed in the same resolution cell due to layover. The separation through geocoding of this targets increases the final pixel density. It also enables the detection of different displacement behaviors for each target, which allows the understanding of complex displacement phenomena, such as the progressive tilt of a building. Notice how this would not be possible with single polarimetric data, since only one of the two scatterers would be detected.

Fig. 4.1b and Fig. 4.1c show the cases when both scatterers are closer. As in the low resolution case, an averaging of displacement values is considered. Note that a distance threshold, in this case the height, should be defined to discriminate between cases 4.1a and 4.1c. The criterion

The criterion to decide the threshold should be based in several factors:

- The precision of the height measurement, in order to separate targets.

- The actual height difference, since farther targets may present different behaviors.

The simplest assumption is that close targets should have the same motion behavior. The precision in height is in the same order of magnitude that the pixel size. Thus, the latter may be used as a possible threshold. To take into account the acquisition geometry,

the next criterion is proposed. Consider a target in the center of the resolution cell at height h equal to zero. If the height increases, eventually the pixel will belong to the previous resolution cell in range, due to the acquisition geometry. This separation will be considered in the following as the height threshold for the separation. It may be defined as

$$h_{th} = \frac{dr}{2\tan\theta} \tag{4.1}$$

where dr is the pixel size in the ground projected range and θ is the incidence angle.

When working at high resolution, another interesting case are the isolated pixels, i.e., pixels which are selected only in one of the polarimetric channels. Given the high resolutions given by the new generation SAR satellites, this situation is bound to be frequent. This also contributes greatly to the pixel density of the final combined results.

4.2   Polarimetric basis optimization

PolSAR datasets are usually given in the lexicographic base, defined by the linear horizontal and vertical polarizations. Of course, the sensitivity of this channels to the scene depends highly on the distribution of the scatterers within, since its particular geometric characteristics may not be suited to this acquisition configuration. In order to improve the overall sensitivity, other polarimetric basis may be used. The following approaches are proposed:

- **Pauli decomposition**: As seen in 2.4.2, this particular decomposition has a direct and easy relation with basic physical geometric configurations that may be found in the scene, related to the odd bounce, even bounce and volumetric scattering. It is particularly useful in urban areas, since most of the targets present one of these scattering behaviors. Even the volumetric scattering, which is usually related to vegetation, has been demonstrated to have sensitivity to non-oriented double bounce scattering [31]. Furthermore, its derivation from the original lexicographic base is direct, so almost no additional computational cost is required, see (2.55). Technically it is not a basis optimization, but as mentioned above it provides in general a better response than the lexicographic base because it is more sensitive to human-made structures.

- **Optimum base**: Section 2.4.4 shows that any polarimetric base may be obtained through a unitary transformation. Through equations (2.63) and (2.64), this may be written as

$$\begin{bmatrix} D1 \\ CR \\ D2 \end{bmatrix} = \begin{bmatrix} 1 & 0 & 0 \\ 0 & \cos 2\phi & \sin 2\phi \\ 0 & -\sin 2\phi & \cos 2\phi \end{bmatrix} \begin{bmatrix} \cos 2\tau & 0 & j\sin 2\tau \\ 0 & 1 & 0 \\ j\sin 2\tau & 0 & \cos 2\tau \end{bmatrix} \begin{bmatrix} HH \\ HV \\ VV \end{bmatrix} \tag{4.2}$$

where D1 and D2 are the direct channels and CR is the cross polar channel of a generic polarimetric base. By adjusting ϕ and τ, an optimum base may be obtained

which maximizes the quality of the base as a whole. The following subsection is devoted to the particular approaches considered.

4.2.1 Optimum base derivation characteristics

The input of the polarimetric basis transformation is the PolSAR data-set in the lexicographic base. The output is an optimum base, consisting of two direct channels and a single cross-polarization channel. This new data-set leads to a new stack of inteferometric pairs, which are characterized by a certain phase quality.

The most straightforward figures of value in the optimization are the phase quality estimators, see section 2.3.1. The idea behind the polarimetric basis optimization is to improve the base as a whole, which may be achieved in several ways. Then, the final reference is related to a certain combination of the estimations in each channel. The approaches considered are:

- **Arithmetic mean**: The arithmetic mean may be defined as

$$\mu = \frac{1}{P} \sum_i^P \sigma_i \tag{4.3}$$

  where σ_i represent the elements averaged and P is the amount of elements, so $P = 3$ for fully polarimetric data. This is the usual statistical parameter considered when trying to maximize a combination of individual measurements. The main drawback is that it has no sensitivity on each term separately, so the optimization may favor some elements over the others.

- **Geometric mean**: The geometric mean is defined as

$$\mu = \left(\prod_i^P \sigma_i \right)^{1/P}. \tag{4.4}$$

  This approach has some interesting characteristics when performing a maximization. On the one hand, since it is based on the product of each element, low values of σ_i lead to a drastic decrease of the geometric mean. On the other hand, similar values in the elements are related to a high geometric mean. Hence, the maximization of μ entail an equalization between the elements averaged.

Hence, the geometrical mean is considered more appropriate for the purposes of basis optimization, since it tends to preserve all the polarimetric channels available. The arithmetic mean may imply a magnification of certain channels, to the detriment of the others.

The polarimetric optimization is applied both for the low resolution and the high resolution approaches, taking as figures of merit the coherence stability and the amplitude

dispersion estimators respectively. For instance, the optimum base derivation for the coherence stability case may be written as

$$\arg\max_{\phi,\tau} \{\mu_\gamma (\phi,\tau)\} = (\gamma_{D1} (\phi,\tau) \cdot \gamma_{D2} (\phi,\tau) \cdot \gamma_{CR} (\phi,\tau))^{\frac{1}{3}} \qquad (4.5)$$

The amplitude dispersion case is equivalent, but undergoing a minimization of the mean dA index.

4.3 Polarimetric basis combination results

This section presents the polarimetric basis results combination using the PolSAR data-set over Barcelona. A comparison between three different polarimetric basis is considered:

- **Lexicographic base:** Using the default polarimetric channels provided in Radarsat-2 PolSAR acquisitions, see (2.54): HH, HV and VV.

- **Pauli Base:** Using the Pauli decomposition over the lexicographic basis, see (2.55): P1, P2 and P3.

- **Optimized base:** Using the best base achievable in terms of phase quality, see Section 4.2. The optimized base channels are addressed as D1 and D2 for the direct channels and CR for the cross channel.

In order to highlight the different characteristics between the low resolution and the high resolution approaches, the results are divided into two different sections. In each case, a statistical comparison between the results provided by each polarimetric basis data-sets is presented. The main information is included in different tables with the statistical PSs distribution for each case. The structure for all the tables is as follows, defining sections from top to bottom:

- **Original 1st/2nd/3rd ch:** Original PSs selection for each channel in the original polarimetric base.

- **1st/2nd/3rd ch. isolated:** Pixel which are isolated in its resolution cell for each channel. For instance, in the lexicographic base, pixels who are either selected only for HH, VV and HV.

- **X & Y mean/sep.:** Combinations of coincident pair of channels. Includes both the averaged (mean) and the separated (sep.) pixels considering the separation threshold described in 4.1.2. Three different sections are included in the table to cover all the possible cases. For instance, in the lexicographic base, pixels who are selected both for HH & VV, HH & HV or VV & HV.

65

- **X & Y & Z mean/sep.:** Same as above, but with combinations of coincident trios of channels. In this case, it represents a single section on the table, since only three channels are available.

- **Total PSs:** Accumulated PSs derived from the combination. Note that the separated pixels are counted twice or three times depending if they belong to a separated pair or trio respectively.

For each section section related to the combination (from section 2 to 7) two kinds of statistical information are provided:

- The actual number of PSs which belong to each case.

- The percent compared to the corresponding original selection. If different selection are involved, all the related percents are provided. To ease the reading of the table, each channel an its related percents are identified by different colors. Note that the percent in the last section (Total PSs) is always above 100%. This is due to the fact that it account for the addition of all channels, so the total amount is always bigger than any of them separately.

This section also includes the mean displacement results over two of the AOIs described in 3.1.1:

- Airport Terminal T1.

- L9 metro line.

Unless specified, all the mean displacement maps provided are generally oriented in the North-East axis. A brief description of the terrain displacement phenomena affecting these areas is provided. For the full and detailed analysis of all the areas of interest, see the phase quality optimization results in 5.6.

4.3.1 Low resolution results

This section is devoted to present the low resolution combined results obtained through the coherence stability estimator. The main objective of this approach is to take advantage of the pixel coincidence, in order to obtain different realizations of the same displacement. This allows to reduce noise in the final measurements. Also, some increase in PS density is expected, exploiting the non-coincident pixels

To provide a view of the impact of the resolution in the combination of results, three different multi-look windows have been considered: 5x3, 9x5 and 13x7 in lines by samples notation. Considering the relation between sampling and resolution provided by the
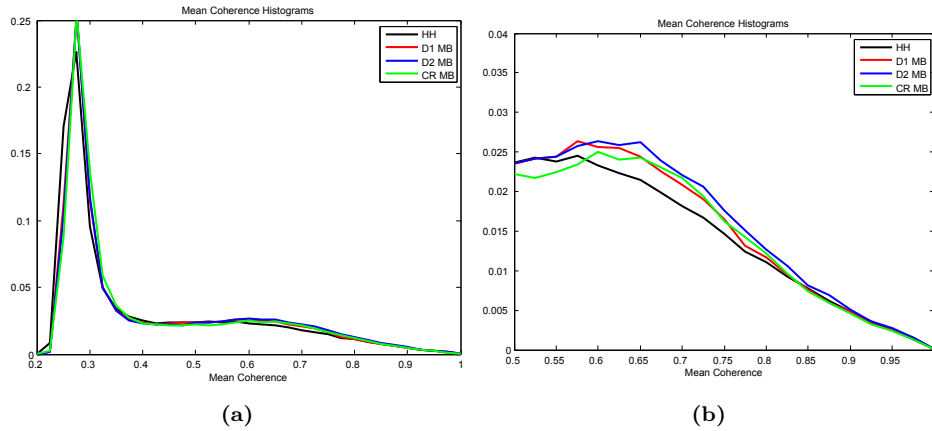
Figure 4.2: Time averaged coherence histograms comparison, using the HH and the optimum base data-set. 4.2a shows the full histogram and 4.2b focuses on the higher values.

data-set (see Table 3.1) the equivalent number of looks for each case is 9.2, 27.8 and 56.2 respectively.

A single phase quality threshold of 10 degrees of standard deviation has been considered for all the cases, setting coherence thresholds according to the relation between phase standard deviation and the coherence values in Fig. 2.12. The according plot has been selected considering the effective number of looks for each case.

Table 4.1, Table 4.2 and Table 4.3 provide the statistical distribution of PSs for each multi-look processed, in the format detailed in section 4.3.

In terms of PSs gain, the comparison between the original selections and the pixels obtained in the final combinations rise up to more than a twofold increase in some cases. Of course, the merging of the different polarimetric channels provides a highest number of measurement points thanks to the polarimetric diversity. However, a decrease in density is observed as the multi-look window increases in size.

There is another interesting issue regarding the different multi-look windows applied. Using a smaller multi-look window the resolution of the data is better preserved, which leads to a better sampling of the terrain under monitoring. This means that the total number of resolution cells also increases, which in principle should automatically provide a higher number of PSs detected. However, this is not the case for this site. The 5x3 multi-look results present a similar or even worse density of PSs than the 9x5 ones. The main argument behind this issue is the trade-off between the proper sampling and the noise reduction which provides the spatial averaging.

Nevertheless, the multi-look 13x7 results provide less PSs than the 9x5 multi-look results as expected. In this case, the spatial sampling is too low and the noise reduction is not

5x3	Lexicographic (**HH**,**VV**,**HV**)	Pauli (**P1**,**P2**,**P3**)	Optimum base (**D1**,**D2**,**CR**)
Original 1st ch.	11427	9917	11385
Original 2nd ch.	9285	12564	12595
Original 3rd ch.	9302	10169	11313
1st ch. isolated	5251	3996	986
%	46.0%	40.3%	8.7%
2nd ch. isolated	4385	6753	1628
%	47.1%	53.7%	17.7%
3rd ch. isolated	3265	4730	1999
%	35.2%	46.5%	12.9%
1st & 2nd mean	1477	2233	2129
%	12.9% 15.9%	22.5% 17.8%	18.7% 18.8%
1st & 2nd sep.	1	2	1
%	0.0% 0.0%	0.0% 0.0%	0.0% 0.0%
1st & 3rd mean	2612	1860	475
%	22.9% 28.1%	18.8% 18.3%	4.2% 3.8%
1st & 3rd sep.	3	3	2
%	0.0% 0.0%	0.0% 0.0%	0.0% 0.0%
2nd & 3rd mean	1339	1751	1043
%	14.4% 14.4%	13.9% 17.2%	9.2% 8.3%
2nd & 3rd sep.	0	2	2
%	0.0% 0.0%	0.0% 0.0%	0.0% 0.0%
All mean	2082	1822	7791
%	18.2% 22.4% 22.4%	18.4% 14.5% 17.9%	68.4% 68.9% 61.9%
All sep.	1	1	1
%	0.0% 0.0% 0.0%	0.0% 0.0% 0.0%	0.0% 0.0% 0.0%
Total PSs	**20422**	**23162**	**16064**
%	179% 220% 220%	234% 184% 228%	141% 127% 142%

Table 4.1: Pixel selection distribution using the coherence stability estimator with a 5 lines by 3 samples multi-look window for all the polarimetric basis processed.

able to compensate for.

The first section of each table is devoted to the PSs provided by the original results. In general, the overall highest density of PSs is found on the optimum base results, for all multi-look windows considered. This is reflected in the time averaged coherence histograms in Fig. 4.2, which shows a comparison between the HH channel and each channel in the optimum base. The HH channel has been selected as a reference, since the histograms for the rest of the channels in the lexicographic and Pauli base are very similar. The coherence improvement is better appreciated towards the high values, as shown in the histograms detail in Fig. 4.2b.

Despite the previous fact, the total PSs provided by the combination is always lower for the optimum base than for the other basis employed. The explanation for this issue lies

9x5	Lexicographic (HH,VV,HV)	Pauli (P1,P2,P3)	Optimum base (D1,D2,CR)
Original 1st ch.	13410	11491	14289
Original 2nd ch.	11115	14919	15662
Original 3rd ch.	11254	12152	14442
1st ch. isolated	4559	2813	1092
%	34.0%	24.5%	7.6%
2nd ch. isolated	2516	6008	2518
%	22.4%	40.3%	17.1%
3rd ch. isolated	3659	3822	1746
%	32.9%	31.5%	11.1%
1st & 2nd mean	2953	2698	2693
%	22.0% 26.6%	23.5% 18.1%	18.8% 18.6%
1st & 2nd sep.	0	0	1
%	0.0% 0.0%	0.0% 0.0%	0.0% 0.0%
1st & 3rd mean	1949	2121	703
%	14.5% 17.3%	18.5% 17.5%	4.9% 4.5%
1st & 3rd sep.	0	4	3
%	0.0% 0.0%	0.0% 0.0%	0.0% 0.0%
2nd & 3rd mean	1697	2354	1422
%	15.3% 15.1%	15.8% 19.4%	9.8% 9.1%
2nd & 3rd sep.	0	0	1
%	0.0% 0.0%	0.0% 0.0%	0.0% 0.0%
All mean	3949	3855	9795
%	29.4% 35.5% 35.1%	33.5% 25.8% 31.7%	68.5% 67.8% 62.5%
All sep.	0	0	2
%	0.0% 0.0% 0.0%	0.0% 0.0% 0.0%	0.0% 0.0% 0.0%
Total PSs	**21282**	**23674**	**19485**
%	159% 191% 189%	206% 159% 195%	140% 128% 138%

Table 4.2: Pixel selection distribution using the coherence stability estimator with a 9 lines by 5 samples multi-look window for all the polarimetric basis processed.

on the pixels coincidence. As explained in 4.2.1, the optimization criterion to derive the optimum based was focused on maximize the quality of the base as a whole. This reflects, as commented above, on an increase of PSs in each channel but also favors the coincidence between channels This is very convenient for the averaging of measurements. Obviously, with more coincidence, the number of isolated pixels decreases as it may be seen in Table 4.1 to Table 4.3. This is the main cause for lower number of PSs in the optimum base results respect to the others.

The goodness of the results may be seen then from two perspectives: High density of PSs versus high quality of measurements. On the one hand, lexicographic and Pauli base are more suited to increase the pixel density and rely on the native quality of the original results. This is reflected in the number of isolated pixels, which reach percent values above 30% in many cases. On the other hand, optimum base prioritizes the pixel coincidence.

13x7	Lexicographic (HH,VV,HV)	Pauli (P1,P2,P3)	Optimum base (D1,D2,CR)
Original 1st ch.	8466	7261	8929
Original 2nd ch.	7139	9432	9668
Original 3rd ch.	6884	7792	8841
1st ch. isolated	2623	1333	516
%	31.0%	18.4%	5.8%
2nd ch. isolated	2100	3383	880
%	30.5%	35.9%	15.6%
3rd ch. isolated	1172	2135	1376
%	16.4%	27.4%	9.1%
1st & 2nd mean	1140	1715	1677
%	13.5% 16.0%	23.6% 18.2%	18.8% 19.0%
1st & 2nd sep.	0	1	0
%	0.0% 0.0%	0.0% 0.0%	0.0% 0.0%
1st & 3rd mean	1813	1323	354
%	21.4% 26.3%	18.2% 17.0%	4.0% 3.7%
1st & 3rd sep.	0	1	0
%	0.0% 0.0%	0.0% 0.0%	0.0% 0.0%
2nd & 3rd mean	1009	1445	729
%	14.1% 14.7%	15.3% 18.5%	8.2% 7.5%
2nd & 3rd sep.	0	0	0
%	0.0% 0.0%	0.0% 0.0%	0.0% 0.0%
All mean	2889	2888	6382
%	34.1% 40.5% 42.0%	39.8% 30.6% 37.1%	71.5% 72.2% 66.0%
All sep.	1	0	0
%	0.0% 0.0% 0.0%	0.0% 0.0% 0.0%	0.0% 0.0% 0.0%
Total PSs	**12749**	**14226**	**11914**
%	151% 179% 185%	196% 151% 183%	133% 123% 135%

Table 4.3: Pixel selection distribution using the coherence stability estimator with a 13 lines by 7 samples multi-look window for all the polarimetric basis processed.

This allows for the averaging between channels of most of PSs in the scene to reduce the measurement noise. Notice that for all multi-look windows employed, the percent of trios is always around 70% in the optimum base case.

The tables also reveal how for all polarimetric basis, the coincidence improves as the multi-look window expands. This is quite expected, since as the resolution cells grow wider the spatial sampling of the terrain decreases, so the total number of possible PSs is also reduced. Then, the coincidence between PSs increases merely for probability reasons.

For the sake of completeness, the tables also include the coincident pixels which are considered separately for exceeding the topographic error difference threshold. Remember that this threshold was set considering the size of the final pixel processed. These values are roughly 25, 45 and 65 meters for the 5x3, 9x5 and 13x7 multi-looks respectively. As
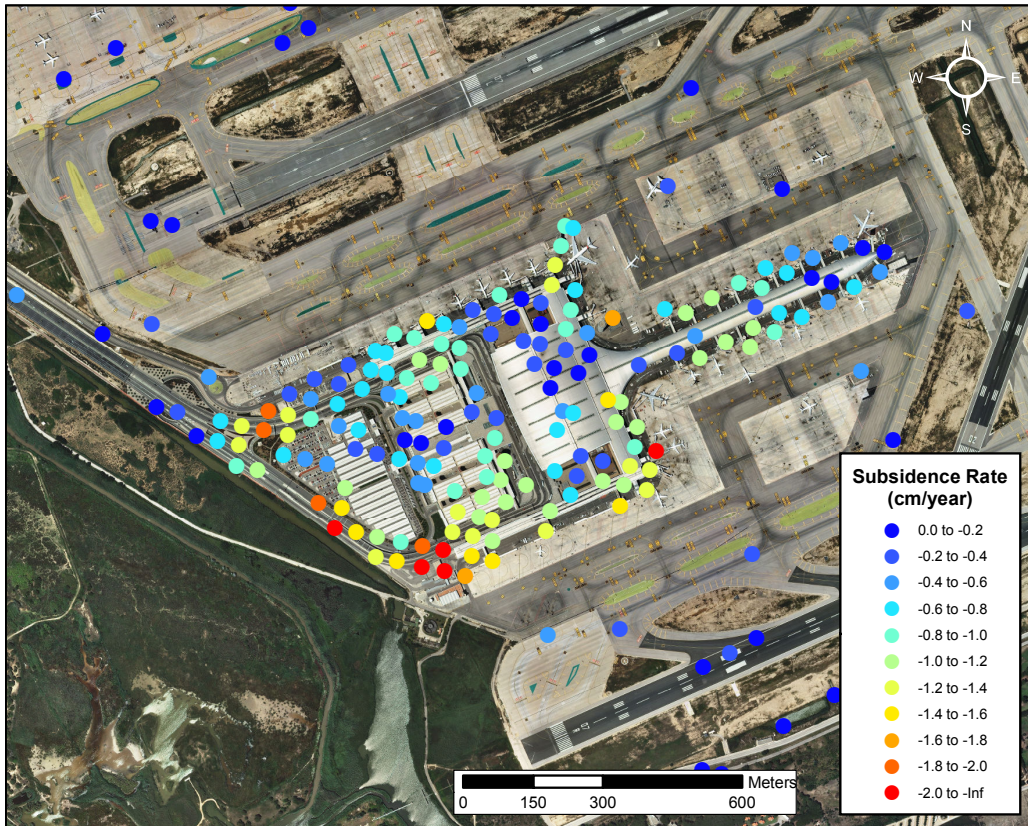
Figure 4.3: Displacement rate combined results of the lexicographic data-sets using the coherence stability estimator over the airport T1 terminal.

it may be seen, these events are statistically nonexistent by using the coherence stability estimator for the combination. Notice that the maximum number of separable PSs detected is only 4 over thousands of pixels, which has almost no significance in the total statistics.

The remaining of this section is devoted to provide a visual representation of the terrain displacement results obtained using low resolution combination techniques. Since it provides a good agreement between resolution and PSs density, the 9x5 multi-look has been selected for the displacement maps. First, a general description is done for each site selected. Then, a comparison between each combination method and one of the original channels is provided.

Fig. 4.3 presents a general overview over the Barcelona-El Prat T1 terminal area. The example map corresponds tho the lexicographic base combination.

A general subsidence behavior is observed in the area. As commented in 3, a certain

71

settlement was expected in the construction project, since the building is over a delta. Most PSs are located on the main structure of the terminal. Some other sparse points are observed in the surroundings. At first glance, the settlement observed is not general, but distributed in several focuses. They are distributed around the structure, reaching mean displacement values of 2 cm/year. Note that the natural area in the southwest part does not include any points. This is part of the Delta del LLobregat natural park, which is basically crowded by dense reeds. C-band is not able to penetrate vegetation, leading to uncorrelated data in all polarimetric channels in the base.

Fig. 4.4 shows the comparison between HH channel results and each one of the basis results combination for the terminal T1 area. In general terms, a certain increase of PSs is observed in the combined results respect to the original channel ones, specially for the lexicographic and the Pauli base case. Also the narrower part of the building, where the plane access fingers are located, is better sampled in the combined results. As an specific comment, the Pauli combination presents higher coverage over the airport runways than the other options. This is due to the fact that P1 channel is directly related to single bounce scattering, which is mainly related to flat surfaces.
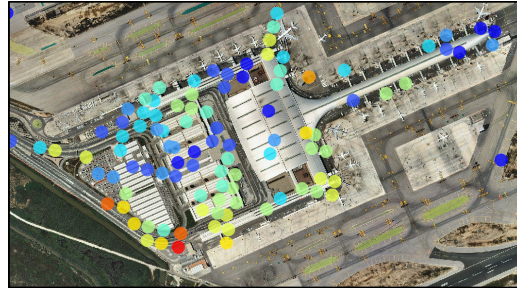
(a)
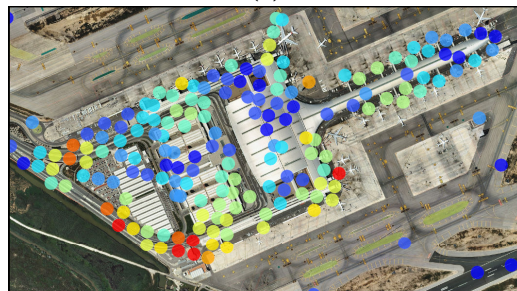
(b)
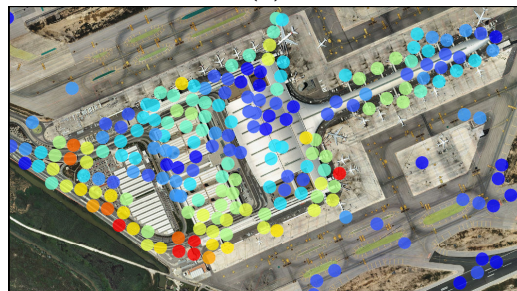
(c)
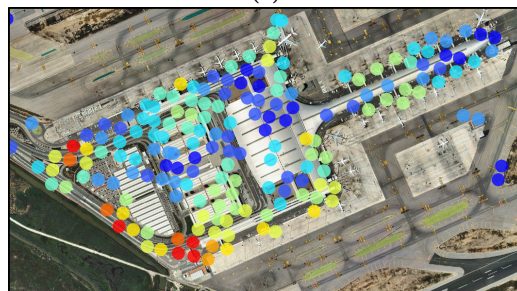
(d)

Figure 4.4: Displacement rate combined results comparison obtained using the coherence stability estimator over the over the airport T1 terminal: (a) HH, (b) lexicographic combination, (c) Pauli combination and (d) optimum base combination.
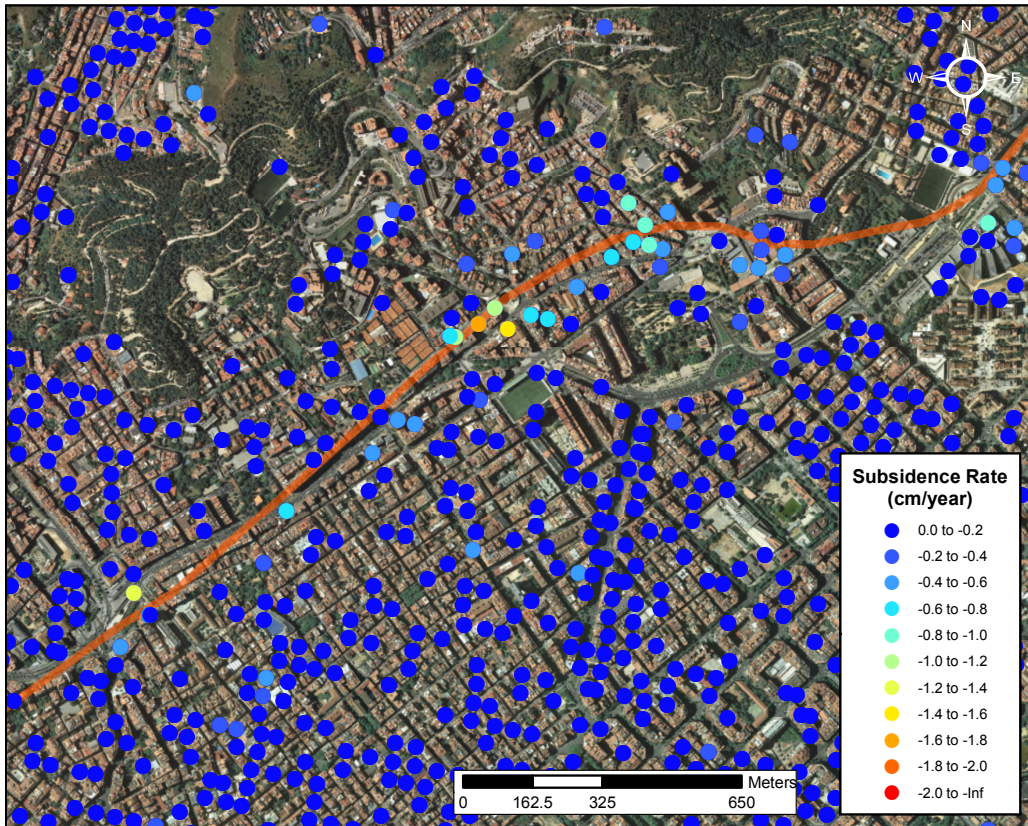
Figure 4.5: Displacement rate combined results of the lexicographic base data-sets using the coherence stability estimator over the L9 metro line.

Fig. 4.5 presents the general overview over the track of metro line under construction in the Barcelona urban area, using the lexicgraphic base combination results. As it may be appreciated, a certain subsidence around the track (depicted in orange) is observed, which is probably caused by the tunneling work performed in the monitoring period, see chapter 3. This is a really challenging subsidence phenomenon to detect, since the displacement magnitude is very low (below 1 cm/year) and the affected area is extremely narrow. The lack of spatial resolution related to the coherence estimator approach is certainly a drawback in this case.

Fig. 4.6 shows the comparison between the HH channel and the base combination results for the L9 metro line track around Sanllehy square. For convenience, a certain tilt has been applied to the image, mind the North direction indicated by the compass. A general increase of PSs is observed in the basis combination results, providing a slightly better coverage in the urban area. However, the sampling and characterization of the phenomenon observed is rather poor. The main improvement is an increase of PSs. The lexicographic and the Pauli basis combination provide the higher PSs increase, while the optimum base basis combination favors the displacement results noise reduction.

74

(a)

(b)

(c)

(d)
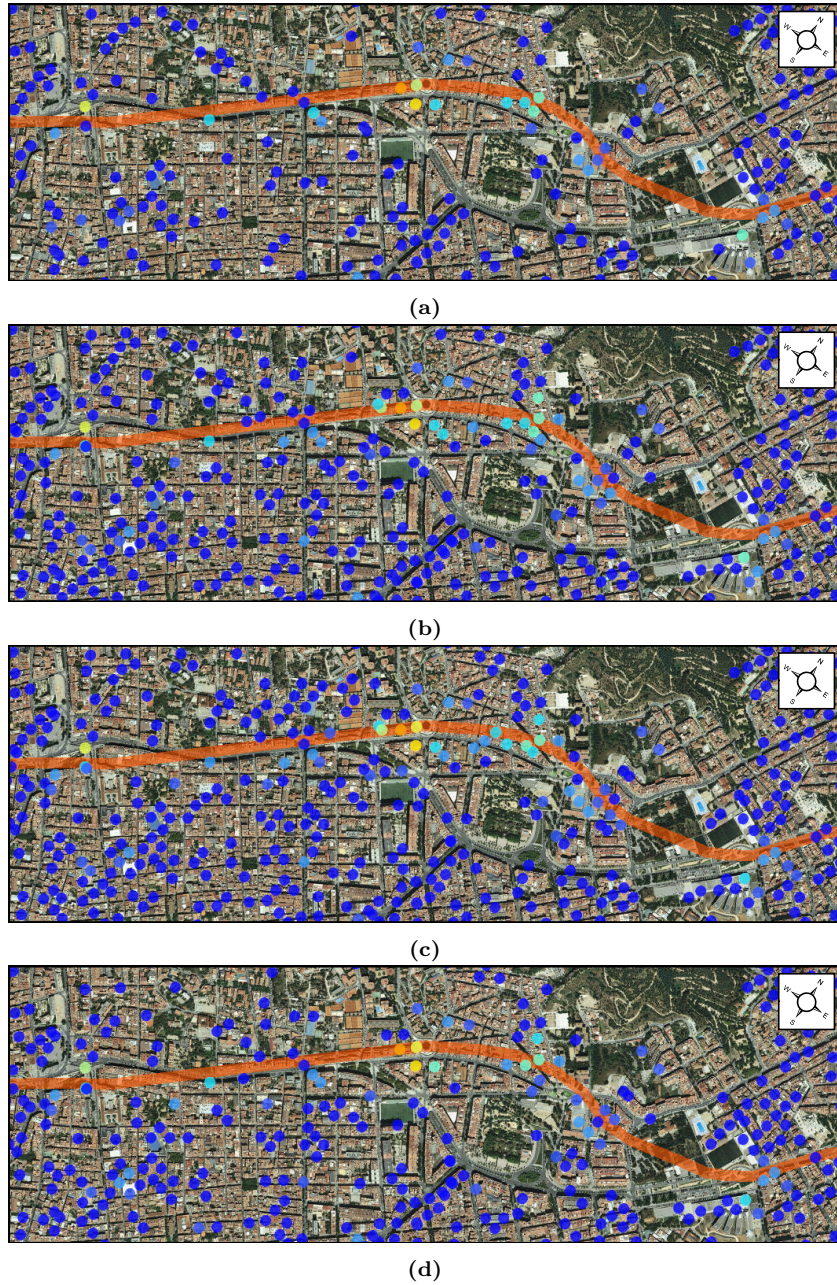
Figure 4.6: Displacement rate combined results comparison obtained using the coherence stability estimator over the L9 metro line: HH (a), lexicographic combination, (b), Pauli combination (c) and optimum base combination (d).

|	Lexicographic (**HH**,**VV**,**HV**)	Pauli (**P1**,**P2**,**P3**)	Optimum base (**D1**,**D2**,**CR**)
Original 1st ch.	92295	84006	129481
Original 2nd ch.	83551	95355	156631
Original 3rd ch.	80152	86316	152550
1st ch. isolated	49012	45946	37306
%	53.1%	54.7%	28.8%
2nd ch. isolated	41632	57182	57877
%	51.9%	60.0%	44.9%
3rd ch. isolated	45348	49517	68571
%	54.3%	57.4%	37.0%
1st & 2nd mean	19251	14099	29066
%	20.9% 23.0%	16.8% 14.8%	22.4% 19.1%
1st & 2nd sep.	66	137	214
%	0.1% 0.1%	0.2% 0.1%	0.2% 0.1%
1st & 3rd mean	12039	12766	13932
%	13.0% 15.0%	15.2% 14.8%	10.8% 8.9%
1st & 3rd sep.	153	96	573
%	0.2% 0.2%	0.1% 0.1%	0.4% 0.4%
2nd & 3rd mean	10758	12793	20343
%	12.9% 13.4%	13.4% 14.8%	13.3% 13.0%
2nd & 3rd sep.	70	182	741
%	0.1% 0.1%	0.2% 0.2%	0.5% 0.5%
All mean	11735	10920	48053
%	12.7% 14.0% 14.6%	13.0% 11.5% 12.7%	37.1% 31.5% 30.7%
All sep.	39	42	337
%	0.0% 0.0% 0.0%	0.0% 0.0% 0.0%	0.3% 0.2% 0.2%
Total PSs	**190480**	**204179**	**279215**
%	206% 228% 238%	243% 214% 236%	216% 178% 183%

Table 4.4: Pixel selection distribution using the dA estimator for all the polarimetric basis processed.

4.3.2 High resolution results

In this section, the high resolution combination results obtained using the dA estimator are shown and analyzed. This estimator is more suitable than coherence stability for the specific scenario under monitoring, since urban areas present a high amount of point-like scatterers.

The main objective in this case is to exploit the polarimetric diversity of PolSAR data. The sensitivity over the scene provided by each channel is bound to deliver a significant increase in PSs density after the combination, compared to the low resolution approach. For all the results obtained, a dA threshold of 0.25 has been set, which is approximately equivalent to 15 degrees of phase standard deviation.

Table 4.4 provides the statistical distribution of PSs for the high resolution combination results, in the format detailed in section 4.3. Concerning the PS density, a great increase is observed when comparing combined results with each original channels in each polarimetric base. More than a twofold increase is present in almost every polarimetric basis. The final number of PSs selected by the lexicographic and the Pauli basis combination results are quite similar, with the latter achieving a slightly better density. The optimum base presents the better density after its combination, outperforming the other basis in a 35-40% of improvement.

The percent of improvement respect to each original base channels for the optimum base is slightly lower compared to the other cases. This is due to the fact that the optimum base channels present a higher quality as a whole compared to the other basis, achieving an improvement around 60% of PSs detected a priori.

Looking at the isolated PSs section for each case, this is the dominating population for the lexicographic and the Pauli base combination results. In general, they represent 50% of pixels respect the originals for each channel. This is not the case for the optimum base, where the percents are significantly lower.

The pairs section present similar percent of PSs for each case, between 10 and 20% of the original pixels. However, channel trios present the other main discrepancy between the lexicographic/Pauli basis and the optimum base. In this case, the optimum base reaches populations between 30 and 40%, while the other cases never reach the 15% of PSs compared to the original channels. The main cause for this event is the a priori PSs density provided by the optimum base, which favors the overall coincidence of pixels.

Regarding coincident pixels which are separated through threshold, small percents are detected in all cases, reaching a maximum of 0.5% respect to the original PSs selections. The relevance of this case is still low as in the low resolution approach, but it is more statistically significant. This information may be locally useful to discriminate two different displacement behaviors in the same resolution cell.

Then, the optimum base in the high resolution approach provides not only the highest density of PSs but also the highest coincidence, becoming the better option among all the polarimetric basis combination options.

In the following, the high resolution polarimetric basis combination results over the same areas as in the low resolution section are presented. The first one is the airport T1 terminal and the second one, the metro line track under construction below the city.

Fig. 4.7 present the general high resolution results at the T1 terminal, using the optimum base results combination approach. Notice how the higher resolution allows for a much better characterization of the several settlement phenomena affecting the surroundings of the building.

Fig. 4.8 presents the comparison between the HH results and each one of the combinations
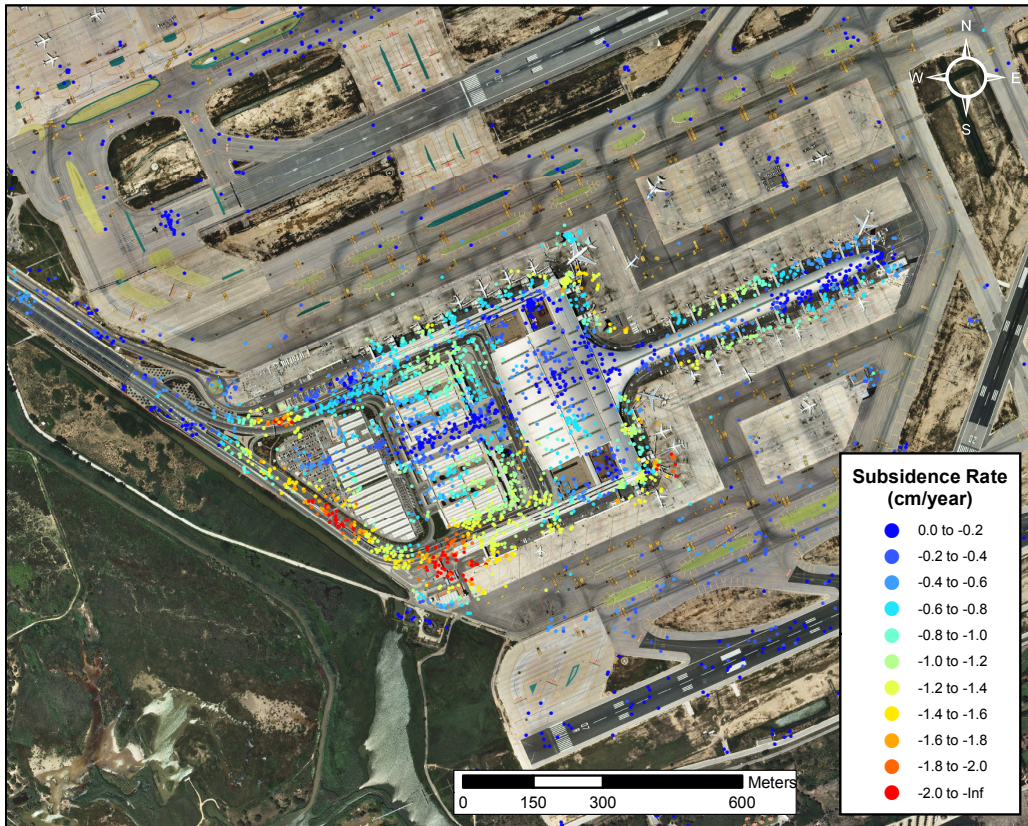
Figure 4.7: Displacement rate optimum base combined results using the dA estimator over the airport T1 terminal.

studied. in this case, unlike the low resolution combination results over this area, the increase of PSs density is easily appreciated from top to bottom, departing from the HH channel until the optimum base combination.
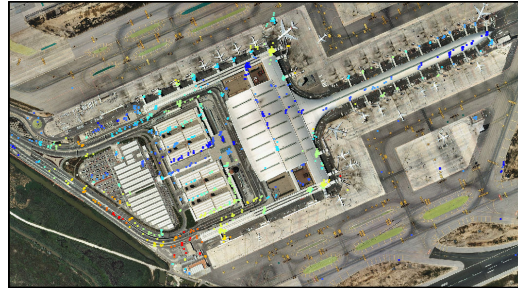
(a)
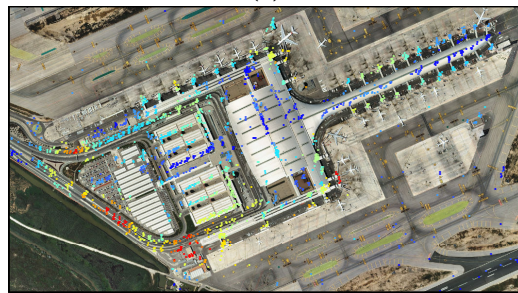
(b)
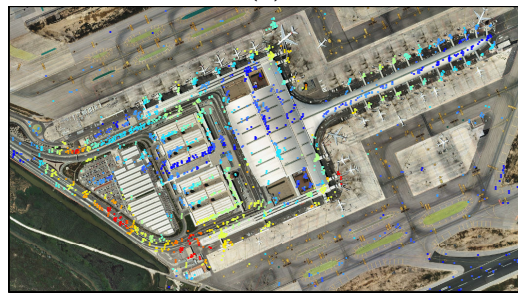
(c)
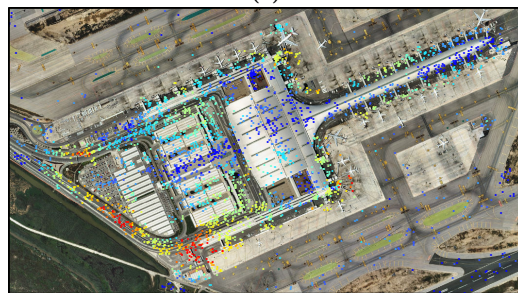
(d)

Figure 4.8: Displacement rate combined results comparison obtained using the dA estimator over the over the airport T1 terminal: HH (a), lexicographic combination, (b), Pauli combination (c) and optimum base combination (d).
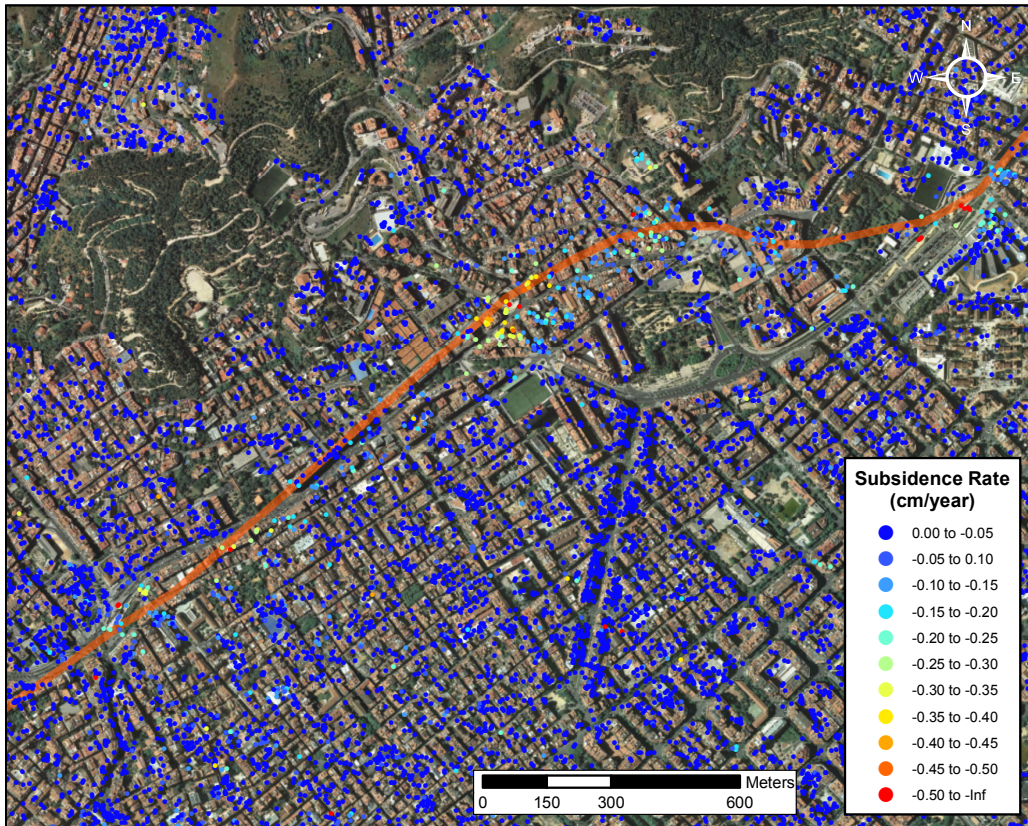
Figure 4.9: Displacement rate combined results of the optimum base data-sets using the dA estimator over the L9 metro line.

Fig. 4.9 shows the general displacement detected along the track of L9 metro line under construction. In this case, also the high resolution plays a key factor to be able to detect the subsidence phenomena caused by the tunneling works. The main subsidence bowl located in Sanllehy square is now easily spotted in the center of the displayed area.

The comparison shown in Fig. 4.10 give an insight of the benefits of a higher density of PSs in order to characterize localized displacement phenomena like this one. The high resolution polarimetric base results combination approaches provide with better characterizations of localized displacement events. Moreover, the polarimetric basis optimization allows to achieve the ideal PolSAR data-set, which provides with both higher PSs density and measurement quality.

(a)

(b)

(c)

(d)
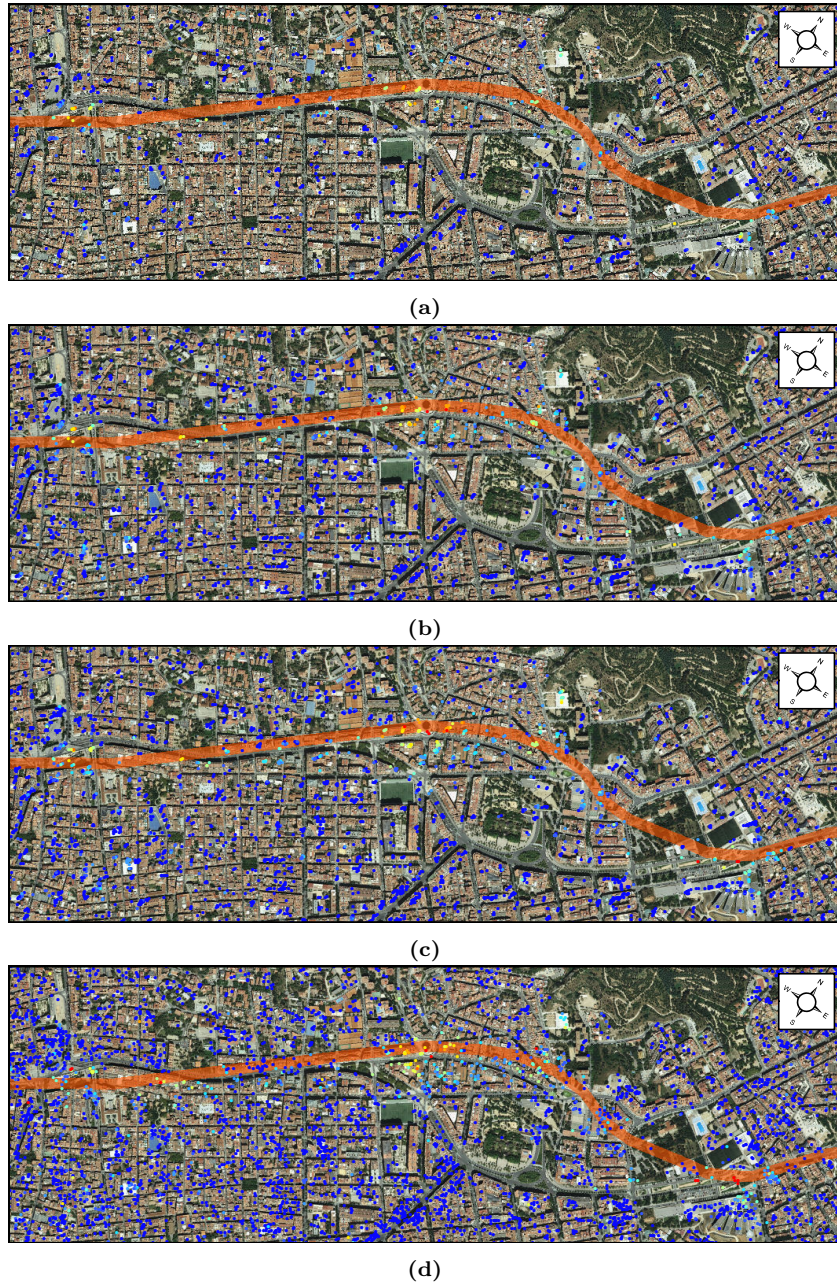
Figure 4.10: Displacement rate combined results comparison obtained using the dA estimator over the L9 metro line.: HH (a), lexicographic combination, (b), Pauli combination (c) and optimum base combination (d).

4.4 Conclusions

This chapter presented the most basic approach to exploit PolSAR data in the PSI framework. Each polarimetric channel is processed by means of the CPT processing chain to retrieve the mean displacement and the topographic error. These results are combined to obtain an improved outcome. Higher density of PSs is achieved and also improved quality, thanks to the redundancy among final results. Both coherence stability and amplitude dispersion estimators are used, providing results at both low and high resolution.

Apart from the well known lexicographic and Pauli basis, the concept of optimum base is introduced. The main aim is to provide an a priori high quality polarimetric base to improve the input of the latter combined results.

For the low resolution combination, different multi-look windows have been tested to analyze the impact of the different levels of averaging. Increasing the multi-look window in general decreases the percent of PSs in the total combination with respect to the original channels. In this case, the better trade off between resolution loss and noise reduction through averaging is given by the 9x5 multilook window. In fact, the number of PSs detected is even better than in the 5x3 case, which has potentially 3 times more resolution cells.

In general, a twofold increase in PSs has been observed in the combined results. This density falls behind with larger multi-look windows, mainly to the reduction of spatial sampling over the scene. The best results in the original basis, in terms of density, are provided by the optimum base for all the cases studied. However, optimum base results combination presents the lowest PSs density. This is expected, since this approach gives priority to the pixel coincidence, and hence, to the measurements averaging.

A priori, the general pixel coincidence was predicted to be high. A clear difference between lexicographic and Pauli with respect to the optimum base is observed. The results show that for the former, depending on the multilook window applied, the coincidence ranges from 30 to 50 percent. Obviously, larger multi-look windows entail higher coincidences. On the contrary, optimum base preserves a more than 70 percent of coincidence for all multi-look windows.

Hence, the appropriate approach depends on the preference between the measurement robustness or the PSs density. Considering the characteristics of the estimator, the former should always be the objective of the low resolution approach. Moreover in terms of density, the high resolution results clearly overcome the low resolution ones. Then, the low resolution approach focused on density should only be considered when:

- The number of point scatterers in the scene is scarce.

- The number of images in the data-set is not enough to fulfill the dA estimator requirements.

For the high resolution combination, using dA as estimator, more than a twofold increase in PSs density is observed for all basis. In this case, the optimum base results combination outperforms the rest of basis in both density and overall pixel coincidence. In fact, each single channel in the optimum base is much better than its counterparts in the other basis. Thus, in terms of percentage of improvement, the optimum base is slightly worse. The latter improvement leads to a lower improvement in combined PSs density for the optimum base respect to the others.

As a concluding remark, it has been observed that the optimum base channels have shown a great improvement with respect to the other basis channels. Basis optimization is restricted to optimize the base as a whole. Thus, dealing with the optimization of a single channel may lead to an even better improvement. Next chapter deals with this approach, usually addressed as phase quality optimization.

5

PHASE QUALITY
OPTIMIZATION

T HE previous chapter deals with the combination of the displacement measurements obtained from each polarimetric channel available in the multi-temporal PolSAR data-set. In this particular approach, the main contribution of the polarimetric aspect of the SAR data is limited purely to the distinction of displacement behaviors between polarimetric channels. The number of PSs for each original channel is limited by the sensitivity of this channel over the scene. The current chapter aims to exploit further the capabilities of PolSAR data, addressing the phase quality optimization concept.

The rationale behind phase quality optimization is to combine the different polarimetric channels available in a PolSAR data-set in order to obtain a single optimum one. A polarimetric channel is more sensitive to certain scattering mechanisms, strongly related to the geometry of the targets in the observed scene. Thus, the aim for a optimum channel which provided the better sensitivity for each resolution cell is justified.

The optimization carried out is for its use in PSI framework, i.e., deal with multi-temporal data-sets. This chapter will show which restrictions must be followed to guarantee a reliable outcome.

The figure of merit used for the optimization are the phase quality estimators described in 2.3.1. Interferometric coherence and dA values are directly related to phase quality. Then, raising the values of the estimators due to optimization leads to a better phase quality in the optimized SAR data-set. At the end, the purpose of the optimization process in provide better results both in terms of PSs density and quality of the measurements.

There are different approaches available in the literature regarding the phase quality optimization, which are described in the following sections. These approaches are applied for each phase quality estimator.

5.1 Phase quality optimization in the PSI framework

The optimization process in a multi-temporal framework is bound by certain restrictions and considerations. This section is devoted to enumerate and describe them.

The resolution cell size in a SAR acquisition is several orders of magnitude higher than the wavelength of the emitted electromagnetic wave. This is directly related to the size of the scatterers detected inside each pixel. In this scenario, the back-scattering wave is the result of the coherent combination of the waves generated by each scatterer separately. In fact, this is the process behind the speckle phenomenon, since the scatterers distribution in each cell may be considered uncorrelated with its neighbors. From this situation arises the concept of scattering phase center, which represents the center of mass of all the scatterers inside the resolution cell, i.e., the equivalent target that would generate the combined back-scattered wave. This is the general reference to characterize the scattering process occurring in each pixel of the SAR image.

Consider a single pixel in an interferogram. The polarimetric configuration of the acquisition defines which targets are detected inside. Therefore, the scatterers distribution and consequently the scattering phase center of the pixel changes for each polarimetric channel. Then, a phase difference exist between channels, since each phase center is related to different path delays.

This extra polarimetric phase component is not desirable form the interferometric point of view, since phase differences should ideally be related only to residual topography and displacement. Thus, to prevent changes in this component, the same polarimetric channel should be considered for both master and slave pixels when forming the interferogram.

When dealing with PolSAR acquisitions, each pixel is characterized by a scattering vector, see 2.4.3. Then, a generic pixel or scattering coefficient μ may be obtained using a complex

projection vector $\boldsymbol{\omega}$ as described in (2.56). When obtaining the interferogram between two generic pixels in different acquisitions, the polarimetric component is avoided by considering the same $\boldsymbol{\omega}$ for both master and slave.

Moreover, since this work deals with multi-temporal PolSAR data-sets, this restriction must apply for the whole set of acquisitions. Then, the projection vector $\boldsymbol{\omega}$ of a particular resolution cell is preserved for each pixel during the whole temporal span of the data-set.

Contrarily to the temporal domain, the spatial domain is not bound to any restrictions, i.e., the neighboring pixels may be set to any polarimetric channel freely. This assumes that neighboring pixels may have completely different phase centers. This is the usual assumption when dealing with PSI techniques.

Note that the previous assumptions regarding a single resolution cell apply to the spatial averaged pixel when using the interferometric coherence estimator as well. Once the spatial averaging is applied the resulting pixel is considered as the new elemental spatial reference.

5.2   Phase quality optimization algorithms

The literature provides several criteria to perform the polarimetric optimization, which may be applied to the different phase quality estimators available. The following subsections describes each one of the approaches considered in this work: Best, Equal Scattering Mechanism (ESM) and Sub-optimum Scattering Mechanism (SOM).

5.2.1   Best optimization criterion

Best is the simplest optimization approach possible. Given a certain polarimetric basis, this algorithm selects for each pixel the polarimetric channel providing the better response. This goodness of this response is provided by the phase quality estimator used. Since it only performs a selection among the polarimetric channels available, no further calculations must be done, so its derivation from the original data is considered immediate.

5.2.2   Equal Scattering Mechanism optimization criterion

The ESM criterion is the most commonly used in the literature. The naming derives from the restriction pointed out in 5.1, i.e., $\boldsymbol{\omega}_i = \boldsymbol{\omega}_j$, where i and j stand for the two PolSAR acquisitions defining and interferogram. Then, a single unitary complex projection vector $\boldsymbol{\omega}$ is considered for both acquisitions. The objective of the ESM optimization is to find

the $\boldsymbol{\omega}$ which optimizes the phase quality estimator employed. The different approaches for each estimator are described in the following sections.

5.2.3 Sub-Optimum scattering Mechanism optimization criterion

This approach is based on the polarimetric basis transformation described in 2.4.4 [35]. The algorithm scans all the possible orthogonal basis, in order to find either the co-polar or the cross-polar channel which maximizes the phase quality estimator value. The sub-optimum tag is due to the fact that the search space of the basis transformation is only a subspace of the possible combinations in the ESM approach, so the SOM solution is always lower or equal than the ESM one. In the following sections, the benefits of this method over the ESM algorithm are pointed out for each phase quality estimator.

5.3 Coherence stability optimization

As described in 2.3.1, the coherence stability estimator performs a temporal averaging of the coherence value for each interferogram. The following subsections describe the distinctive features for each one of the criteria shown in 5.2.

5.3.1 Best coherence stability

The basic estimation of the phase quality in an interferogram is the coherence estimator described in 2.2.4. Then, the Best approach over this estimator simply selects, for each pixel, the polarimetric channel with the highest coherence value. This may be summarized, taking as an example the lexicographic basis, as

$$\hat{\gamma}_{Best} = \max\left\{\hat{\gamma}_{hh}, \hat{\gamma}_{hv}, \hat{\gamma}_{vv}\right\}. \tag{5.1}$$

The extension of the Best approach for a multi-temporal data-set, from now on Best-MB, uses the coherence stability estimator defined in (2.33) instead of the coherence estimator. Then, the corresponding summarized equation is

$$|\hat{\gamma}_{Best}| = \max\left\{|\hat{\gamma}_{hh}|, |\hat{\gamma}_{hv}|, |\hat{\gamma}_{vv}|\right\}. \tag{5.2}$$

The interferometric phase is the one related to the polarimetric channel selected. Note that, since the estimator involves the whole data-set, the selection is preserved during all the temporal span of the data-set, accomplishing the restrictions stated in 5.1.

This method is very simple and effective, since the scattering diversity in the available polarimetric channels provides good sensitivity in most of the cases. Moreover, its derivation may be considered instantaneous, since only a maximum calculation is necessary

to obtain each pixel. However, this method does not fully exploit the possibilities of the PolSAR data. The following subsections describe more efficient ways to perform the polarimetric optimization.

5.3.2   ESM coherence stability

The original coherence optimization algorithms focused on the single baseline problem, i.e., perform the optimization considering a single interferogram. The general formulation is described in [32], in which the projection vectors for the first and the second acquisition may be different. This approach, known as Different Scattering Mechanism (DSM), is analytically solvable, which is very convenient. However, it does not accomplish the temporal restriction set in 5.1, where projection vectors for master and slave in the interferogram must be the same. Then, this approach has been discarded for the purposes of this work.

In order to fulfill this temporal restriction, an adaptation of the algorithm to was proposed in [36], which sets the basis of the ESM approach for coherence optimization. In fact, the new algorithm optimizes a tweaked version of the general formulation of the coherence, expressed as

$$\hat{\gamma}_C = \frac{\boldsymbol{\omega}^H \boldsymbol{\Omega}_{ij} \boldsymbol{\omega}}{\boldsymbol{\omega}^H \mathbf{T} \boldsymbol{\omega}} \tag{5.3}$$

where i and j label master and slave acquisitions and $\mathbf{T}$ is the averaged covariance (or coherence) matrix, defined as

$$\mathbf{T} = \frac{\mathbf{T}_{ii} + \mathbf{T}_{jj}}{2} \tag{5.4}$$

A nice feature of this new coherence expression is that $|\hat{\gamma}_C| \leq |\hat{\gamma}|$ and the phase is exactly the same as in the original coherence.

Unfortunately, this optimization problem is no longer solvable analytically. Then, it must be addressed with a numerical iterative solution based on the numerical radius [36, 37]. The algorithm assumes coherence stability, when $\mathbf{T}_{ii} \simeq \mathbf{T}_{jj}$. This is the same as considering that the scattering term described in (2.17) remains unchanged between acquisitions, i.e., the targets distribution is the same. This is a common requirement with PSI techniques.

As an alternative, the optimization of the generalized coherence expression in (2.60) may be carried out using a brute force method. The projection vector may be parameterized as [32]

$$\boldsymbol{\omega} = \left[\begin{array}{c} \cos\alpha \\ \sin\alpha\cos\beta e^{j\delta} \\ \sin\alpha\sin\beta e^{j\phi} \end{array} \right] \left\{ \begin{array}{l} 0 \leq \alpha \leq \frac{\pi}{2} \\ 0 \leq \beta \leq \pi \\ 0 \leq \delta \leq \pi \\ -\pi \leq \phi \leq \pi \end{array} \right. \tag{5.5}$$

Considering a certain sampling on the parameters, the whole space of solutions may be scanned in order to find the optimum solution [38, 39].

89

Applying any of the two previous approaches, an optimum value of the projection vector $\boldsymbol{\omega}_{opt,ESM}$ is obtained, which defines the combination of polarimetric channels that provide the better phase quality. The related coherence may be derived from (2.60), obtaining the optimum values of coherence modulus and interferometric phase.

The ESM approaches to polarimetric optimization described above refer to the single baseline case, i.e., the optimization of an individual interferogram. Since this work deals with multi-baseline data, and according to the restrictions in 5.1, a global optimization which involves all the interferometric pairs must be carried out. This approach is referred as Multi-Baseline Equal Scattering Mechanism (ESM-MB) in the following. Its formulation is an extension of the ESM case. The figure of value in this case is the time averaged coherence modulus, i.e., the coherence stability estimator defined as

$$\bar{\gamma} = \frac{1}{M} \sum_{i=0}^{M-1} |\hat{\gamma}_i| \tag{5.6}$$

where M is the number of interferograms.

As in the ESM case a brute force approach may be used, this time applied to (5.6). However, given the fact that the whole PolSAR data-set is involved in the calculation, the computational cost is severely increased.

The solution proposed in [40], which is an extension of the work in [36] to tackle the multi-baseline coherence optimization, is used in this work instead. As in the single baseline case, an alternative expression to perform the optimization is defined. Assuming also polarimetric stability, this time in the whole interferometric stack, the averaged covariance (or coherence) matrix is defined now as

$$\mathbf{T} = \frac{1}{N} \sum_{i=1}^{N} \mathbf{T}_{ii} \tag{5.7}$$

where N is the number of PolSAR acquisitions. Using (5.7), an equalization may be applied to the polarimetric interferometric matrices and the projection vector as

$$\boldsymbol{\Pi}_{ij} = \mathbf{T}^{-1/2} \boldsymbol{\Omega}_{ij} \mathbf{T}^{-1/2} \qquad \mathbf{w} = \frac{\mathbf{T}^{1/2}\boldsymbol{\omega}}{\boldsymbol{\omega}^H \mathbf{T}^{1/2}\boldsymbol{\omega}} \tag{5.8}$$

The optimization criterion is given by

$$\bar{\Gamma} = \frac{1}{M} \sum_i \sum_j \left|\hat{\Gamma}_{ij}\right| \tag{5.9}$$

where

$$\hat{\Gamma}_{ij} = \mathbf{w}^H \boldsymbol{\Pi}_{ij} \mathbf{w}. \tag{5.10}$$

Considering this setup, the optimum values of $\boldsymbol{\omega}$ are obtained through a numerical iterative process, well described in [40]. Note that the method described in [40] is equivalent to [36] when reducing the PolSAR data-set to only 2 acquisitions. Following this approach notably reduces the computational cost of the minimization.

5.3.3 SOM coherence stability

The SOM optimization method is based on the polarimetric basis transformation described in 2.4.4 [35]. It focuses on finding the values of ϕ and τ that maximizes the inteferometric coherence in one of the three channels of the resulting polarimetric base. Notice how only one channel is taken, while the others are rejected. Since only a basis rotation is applied, this solution is only a subspace of the possible solutions in the ESM method.

Considering the scattering vector in the lexicographic basis defined in (2.54), the generic transformed scattering vector defined in (2.63) may be expressed as

$$\mathbf{k}_{AB} = \left[S_{aa}, \sqrt{2}S_{ab}, S_{bb} \right]^T \tag{5.11}$$

S_{aa} and S_{bb} represent co-polar channels, so an optimization process leads to the same solution in both cases. Then, the problem is reduced to apply the optimization only on a co-polar and a cross-polar channel. Labeling the generic interferometric coherence in each case as γ_{aa} and γ_{ab}, the optimization process may be defined as

$$\gamma_{SOM} = \max \left\{ \arg\max_{\phi,\tau} \gamma_{aa}, \arg\max_{\phi,\tau} \gamma_{ab} \right\} \tag{5.12}$$

In order to extend to the multi-baseline problem, the Multi-Baseline Sub-optimum Scattering Mechanism (SOM-MB) is proposed. As in the ESM-MB case, this approach optimizes the coherence stability estimator defined in (5.6). Note that a single pair of optimum ϕ and τ values are found for each pixel in the whole interferometric stack.

Unfortunately, the solution may only be reached by a brute force approach. However, a two step process is applied to ease the computational cost, sampling the values of ϕ and τ with a coarse step and finding the optimum solution through the application of the CGM algorithm [29].

5.4 Amplitude dispersion optimization

This section focuses on the application of the optimization criteria described in 5.2 for its application on the amplitude dispersion estimator. Unlike the coherence estimator, the amplitude dispersion requires the whole set of SAR acquisitions in order to obtain the phase quality estimation. In other words, it is inherently suitable for a multi-temporal data-set. Each pixel in the temporal stack is associated to a single phase quality measurement. The next subsection go into the details of each optimization criterion.

5.4.1 Best amplitude dispersion

The application of the Best method is straightforward. Taking as a reference the lexico-graphic basis, the optimum amplitude dispersion in the Best criterion is

$$D_{A,Best} = \min \{D_{A,hh}, D_{A,hv}, D_{A,vv}\}. \tag{5.13}$$

The interferometric phase for each pixel is the one matching the selected channel.

5.4.2 ESM amplitude dispersion

The ESM criterion aim to find the optimum polarimetric combination which provides the highest possible phase quality value. In the case of optimizing the amplitude dispersion, a general expression of the estimator may be defined as [38, 41, 42]

$$D_A (\boldsymbol{\omega}) = \frac{1}{\langle |\boldsymbol{\omega}^H \mathbf{k}| \rangle} \sqrt{\frac{1}{N} \sum_i^N \left(|\boldsymbol{\omega}^H \mathbf{k}_i| - \langle |\boldsymbol{\omega}^H \mathbf{k}| \rangle \right)^2} \tag{5.14}$$

where

$$\langle |\omega^H \mathbf{k}| \rangle = \frac{1}{N} \sum_i^N |\omega^H \mathbf{k}_i|. \tag{5.15}$$

Notice how any polarimetric basis defining the scattering vectors $\mathbf{k}_i$ of each acquisitions is suitable. In other words, since this transformation involves the whole polarimetric space, the starting orthogonal basis is irrelevant.

To solve the optimization problem, a brute force approach must be undertaken, parameterizing the projection vector as described in (5.5) and sampling the parameters. As in previous cases, the computational cost may be lowered considering a coarse search step followed by a CGM refinement in order to find the optimum solution.

The optimum projection vector $\boldsymbol{\omega}_{opt,ESM}$ may be applied to the scattering vectors of each acquisition to obtain each optimum ESM SAR image. The optimum interferometric phases are derived from the combinations of the optimum images. The optimum interferometric phase expression is

$$\phi_{ESM} = \arg \left\{ \left(\boldsymbol{\omega}_{opt,ESM}^H \mathbf{k}_i \right) \left(\boldsymbol{\omega}_{opt,ESM}^H \mathbf{k}_j \right)^* \right\} \tag{5.16}$$

5.4.3 SOM amplitude dispersion

As in the coherence case, the SOM criterion may be applied to the amplitude dispersion estimator. The brute force method is the only solution also in this approach, sampling all

the possible values of ϕ and τ to find the optimum dA for each pixel. An specific pair of parameters is associated for all the time series of each pixel, to preserve the restriction in 5.1. The optimization is applied to both the co-polar and the cross-polar channel. The, the optimum value is the one providing the minimum amplitude dispersion value. All the process is summarized as

$$D_{A,SOM} = \min \left\{ \arg\min_{\phi,\tau} D_{A,aa}, \arg\min_{\phi,\tau} D_{A,ab} \right\}, \tag{5.17}$$

where $D_{A,aa}$ and $D_{A,ab}$ stand for the co-polar and the cross-polar amplitude dispersion indices.

5.5 Temporal sublook coherence optimization

The last specific phase quality optimization section is devoted to the temporal sublook coherencee estimator. As the amplitude dispersion estimator, the TSC obtains a global estimation for each pixel, which perfectly adapts to any multi-baseline approach. In the following subsections, the particularities of each optimization approach are put forward.

5.5.1 Best temporal sublook coherence

As for the other estimators reviewed, the application of the Best approach for the TSC relies on the estimations for each original polarimetric channel as

$$TSC_{Best} = \max \{TSC_{hh}, TSC_{hv}, TSC_{vv}\}. \tag{5.18}$$

The Best TSC interferometric phase is the one related to the channel selected.

5.5.2 ESM temporal sublook coherence

As stated in 5.2, the TSC estimation is based on the coherence estimator, where the master and slave involved are the temporal time series of each sublook for each pixel. Considering this fact, from the estimator point of view, the calculus is equivalent to a single-baseline case. Then, all the theoretical basis in [32] and [36], briefly described in 5.3.2, is applicable for the TSC optimization. The main difference is the definition of the scattering vector and thus, the polarimetric and inteferometric covariance matrices.

For a certain pixel, the sublook scattering vector in the lexicographic basis may be defined as

$$\mathbf{k}_{i,t} = \left[SL_{i,hh}(t), \sqrt{2}SL_{i,hv}(t), SL_{i,vv}(t) \right]^T \tag{5.19}$$

93

where $i = 1, 2$ is the sublook index and t is the time domain index. Considering this scattering vectors, parallel definitions of (2.57) and (2.58) may be considered, with two main differences:

- The spatial averaging related to the multilook is replaced by a temporal averaging of the time series.

- The $[i, j]$ indices are fixed to [1,2], since the correlation is between the two sublook stacks.

This matrices allow the definition of a generalized expression for the TSC estimator as

$$TSC\left(\boldsymbol{\omega}\right) = \frac{\left|\boldsymbol{\omega}^{H}\boldsymbol{\Omega}_{12}\boldsymbol{\omega}\right|}{\sqrt{\left(\boldsymbol{\omega}^{H}\mathbf{T}_{11}\boldsymbol{\omega}\right)\left(\boldsymbol{\omega}^{H}\mathbf{T}_{22}\boldsymbol{\omega}\right)}}. \tag{5.20}$$

Notice how this definition is equivalent to the generic interferometric coherence defined in (2.60). However, in this case the absolute value is taken since it is the only relevant term for the TSC estimation.

Since the optimization is equivalent to a single baseline case, the approach proposed in [36] may be applied directly. The algorithm is equivalent to the ESM-MB described in equations (5.7) to (5.10), with $[i, j] = [1, 2]$ and $M = 2$. As on the other cases, the brute force method using the parameterization in (5.5) may be used instead.

5.6 Phase quality optimization results

This section shows the application of the optimization techniques in the PSI framework. For this purpose, the real data-set over Barcelona described in chapter 3 is employed. The main objective is to point out, showing several examples, the benefits of polarimetric optimization in the detection of displacement phenomena.

First some examples of the optimization functions are provided, both for the coherence stability and the amplitude dispersion estimators.

Then, the results over the airport T1 terminal and the L9 metro line track are shown. The rest of the areas described in chapter 3 are included in appendix A. In all cases, the results for both estimators are provided. Each section compares the results obtained using the original polarimetric channels [HH,VV,HV] and the ESM-MB optimized ones. For the sake of simplicity, all the mean displacement values provided are projected in the vertical direction, assuming that all the ground motion detected presents a subsidence behavior.

5.6.1 Optimization functions

As seen in the previous sections, SOM-MB and ESM-MB are based on an optimization process. Either the coherence stability or the amplitude dispersion may be given as a function certain parameters which explore the polarimetric space. This function is then maximized (for coherence) or minimized (for dA) to find the optimum value of the estimator. In the following, some examples are given to illustrate its behavior. Since the ESM-MB optimization depends on four parameters, the graphical representation is intricate. Since the general behavior of both functions is the same, SOM-MB examples are given instead, which only depend on two parameters.

Fig. 5.1 shows some examples of SOM-MB functions to optimize, based on the coherence stability estimator. In each case, a different level of mean coherence for the Best-MB case has been taken as reference. This is intended to provide samples of optimization functions for different levels of phase noise.

As it may be appreciated, the smoothness of the function does not depend much on the quality of the original data. Moreover, they include in general a single true maximum, with the possible existence of local maxima.

This characteristics of the function allow for the two steps approach minimization. First, a coarse step with enough sampling to discriminate between the local an the true maximum. Second, a refinement step, based on the CGM algorithm, in order to locate the exact maximum of the function.
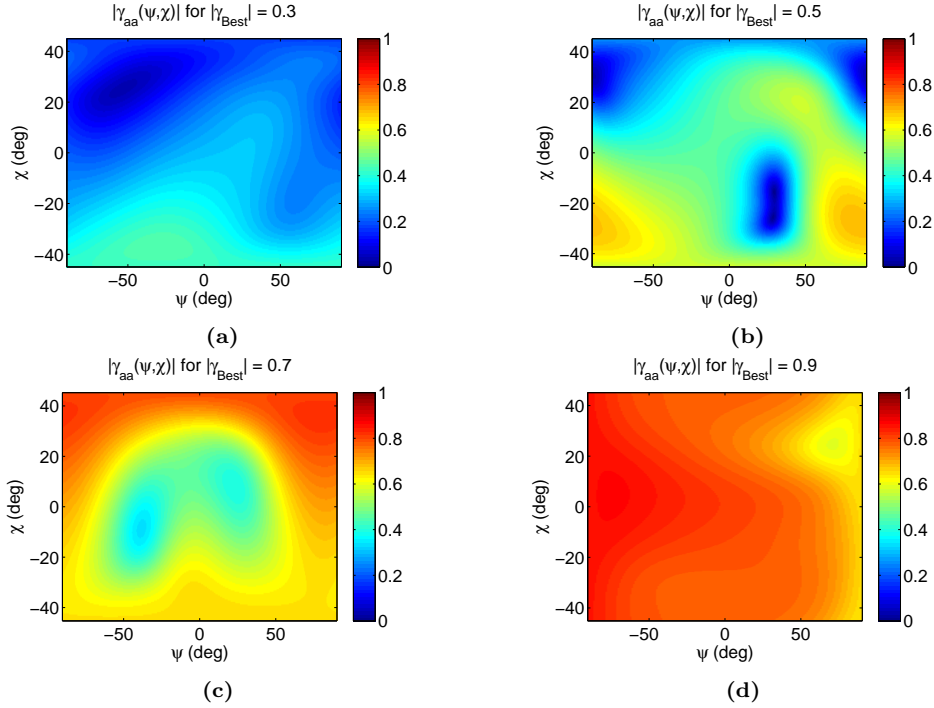
Figure 5.1: SOM-MB optimization functions examples using the coherence stability estimator, for pixels at different Best-MB mean coherence levels. (a) $\gamma_{Best-MB} = 0.3$, (b) $\gamma_{Best-MB} = 0.5$, (c) $\gamma_{Best-MB} = 0.7$ and (d) $\gamma_{Best-MB} = 0.9$.

Despite including a single maximum, it may be either very localized as in Fig. 5.1b or quite spread as in Fig. 5.1d. This is related to the polarimetric diversity of the pixel. For instance, the pixel in Fig. 5.1b has a good response only in a particular polarimetric configuration while the one in Fig. 5.1d may be sensitive to several configurations.

Fig. 5.2 shows some examples of the SOM-MB optimization approach based on the dA estimator. As for the coherence stability case, the Best-MB approach is taken as reference in order to select different quality pixels.

A similar smooth behavior is observed. As in the previous case, also a single true minimum with possible local minimums are found, see the blue areas in Fig. 5.2. In general, the minimums are narrower than in the coherence case, due to the highest polarimetric sensitivity present in full resolution PolSAR data. A clear example is found in Fig. 5.2a. However, some points like Fig. 5.2d may be equally sensitive in almost any polarimetric configuration. Therefore, it is worth pointing out that this functions are not only a way to reach the optimum value for the PSs quality. Moreover, they prove to be a powerful tool to analyze the nature of the targets detected.
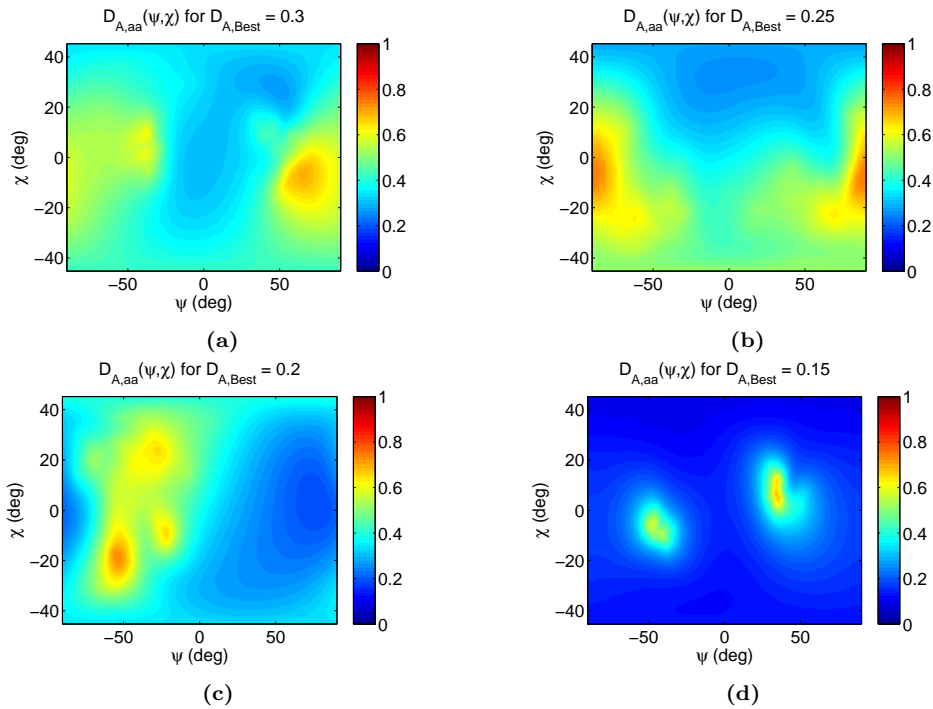
Figure 5.2: SOM-MB optimization functions examples for the dA estimator, for pixels at different Best-MB mean coherence levels. (a) $\gamma_{Best-MB} = 0.3$, (b) $\gamma_{Best-MB} = 0.5$, (c) $\gamma_{Best-MB} = 0.7$ and (d) $\gamma_{Best-MB} = 0.9$.

5.6.2 Coherence stability optimization results

The coherence stability results obtained in this chapter used a multi-look window of 9 ines by 5 samples. The mean coherence threshold is set to 0.68, equivalent to a phase standard deviation of 10 degrees.

The structure of the results chapter is organized as follows: First a comparison between the different optimization techniques described over the entire monitored area are provided. Then specific results over the different areas of interest are shown, with an overview and specific comparisons between the performance of the original channels and the optimized ones. Moreover, a comparison with the polarimetric basis combination results presented in chapter 4 is carried out. This is used as an additional benchmark to assess, in terms of PSs density, the performance of phase quality optimization methods.

97
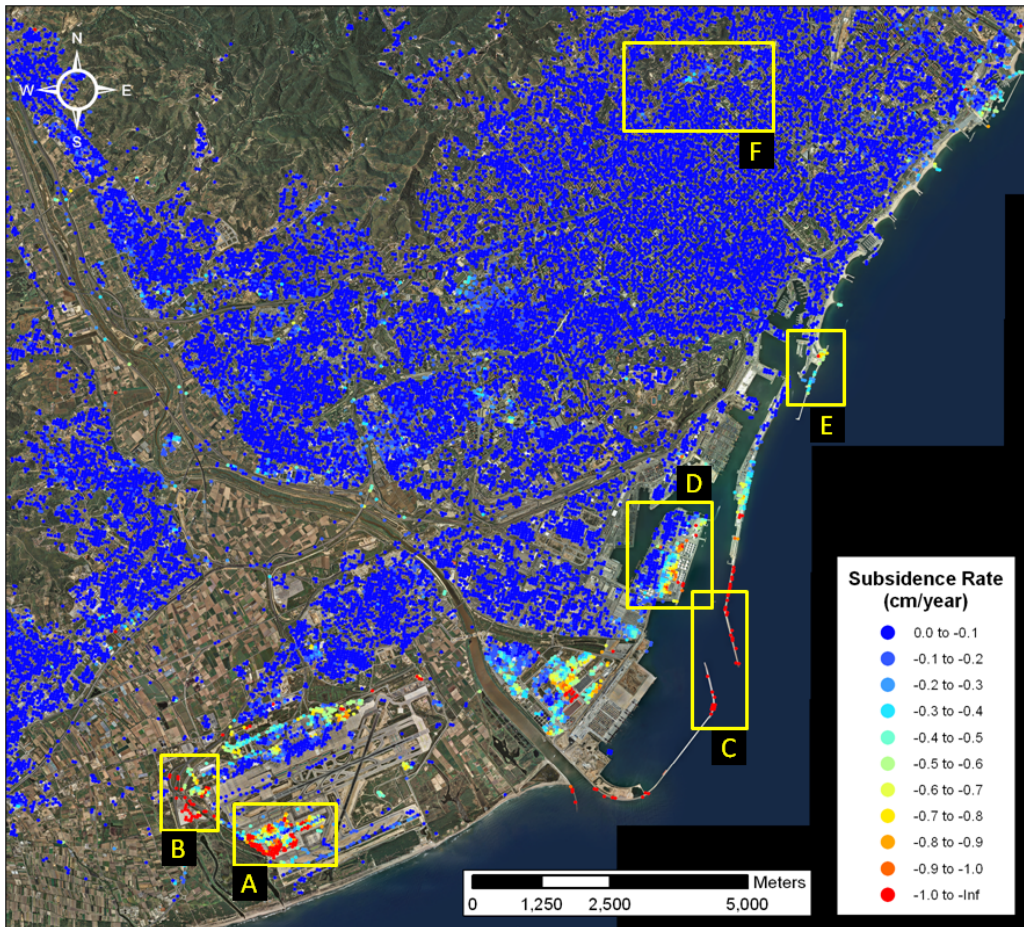
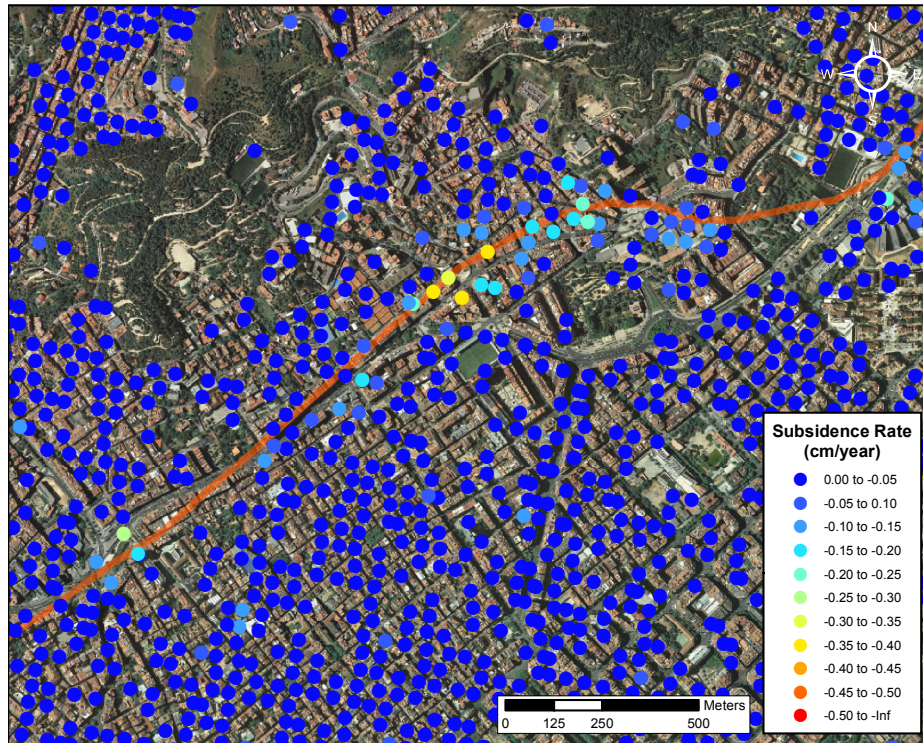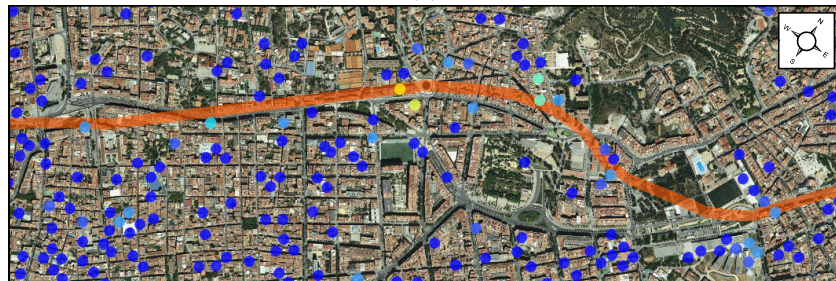**Figure 5.3:** General displacement rate results obtained using the ESM-MB optimization on the coherence stability estimator over Barcelona. The different areas of interest are shown from A to F.

5.6.2.1 General results

Fig. 5.3 gives an overview of the subsidence detected over the whole area under monitoring. A scale between 0 and 1 cm/year has been selected, since it is a good compromise to better appreciate all the different areas presenting subsidence. Each specific AOI is labeled with a capital letter. The current chapter includes area A and area F. The rest of the sites, from B to E, are found on appendix A. Each area is provided with an adapted scale to better observe the motion pattern.

As it may be appreciated, most of the subsidence phenomena detected are found near the coast. However, some small affected areas are found in the urban area. As expected, most of the PSs are found in areas with man-made structures. All gaps observed are related
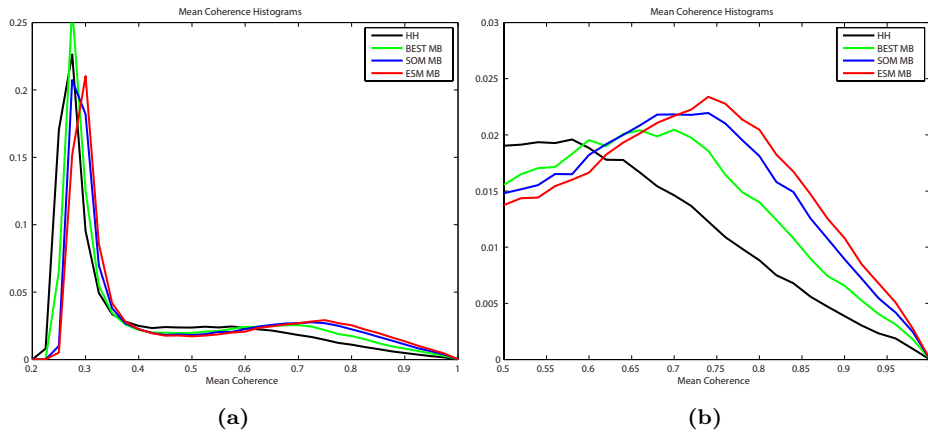
Figure 5.4: Time averaged coherence histograms comparison, using the HH, Best-MB, SOM-MB and ESM-MB data-set. 5.4a shows the full histogram and 5.4b focuses on the higher values.

mostly to agricultural areas, forests, parks or areas experiencing continuous changes. For instance, notice the elongated vertical gap to the East of area F. This corresponds to La Sagrera train station, which is currently under construction.

Fig. 5.4a shows the histograms with the distribution of time averaged coherences for one of the original channels and for each optimization method. The high peak around 0.3 is related both to water bodies and vegetated areas. A great portion of the area processed is over the sea, and that is the reason for this unbalance towards the low values of mean coherence.

The quality improvement by the optimization in lower section of the histograms is not significant. In other words, there is no polarimetric combination which provides an stable response in time. This is expected in those areas where all targets are affected by temporal decorrelation. However, the high section of the histograms, see Fig. 5.4b, highlights the usefulness of the optimization techniques. As it may be seen as the complexity of the optimization method increases, a better time averaged coherence is achieved.

Table 5.1 resumes the different PSs detected for each optimization method. The original lexicographic basis and each polarimetric basis combination results are also included to ease the comparison. A notable increment in PSs density is already achieved by the Best-MB method, with almost a factor of two in some cases. SOM-MB provides a better improvement, reaching almost a factor of 2 with respect most of the original channels. Of course, the best result is given by the ESM-MB method, approaching a threefold increase in PSs density.

A comparison of the current results with the densities achieved by the polarimetric basis combination results is carried out in the following. Obviously, the combination is done with equivalent data-sets, i.e., using a multi-look window of 9x5 with the same mean co-

MLook:9x5	PSs	Incr. vs HH	Incr. vs VV	Incr. vs HV
HH	13410	1.00	1.21	1.19
VV	11115	0.83	1.00	0.99
HV	11254	0.84	1.01	1.00
Lexicographic comb.	21282	1.59	1.91	1.89
Pauli comb.	23674	1.76	2.13	2.10
Optimum comb.	19485	1.45	1.75	1.73
Best-MB	21352	1.59	1.92	1.89
SOM-MB	24512	1.82	2.20	2.18
ESM-MB	30945	2.31	2.78	2.75

Table 5.1: PSs selected for each data-set. Polarimetric basis combination results are also included for comparison. ML window: 9x5. Coherence threshold: 0.68

herence threshold. At first glance, the density using the lexicographic basis combination is almost identical as the one achieved by the Best-MB method. This is quite expected, since the Best-MB mean coherence is constructed taking the better values from the lexicographic channels. Any difference is related to the PSI processing, for instance, the PSC filtering of isolated pixels after the linear estimation, see 2.3.2. Surely, Best-MB applied to the other polarimetric basis available would provide similar densities as the ones shown in Table 4.2.

The PS density achieved by the SOM-MB method overcomes all polarimetric basis combination results. In this case, since some portion of the polarimetric space is surveyed, the solution achieves a more optimum solution for the phase quality. However, the results are only slightly better than the Pauli combination ones. This is surely related to the scene under monitoring, since Pauli base characterizes quite well the targets found in urban areas.

ESM-MB performance is clearly better than any polarimetric optimization results, achieving improvement factors between 1.3 and 1.6 depending on the case. Moreover, the phase noise is reduced, making this option the preferred one both in terms of density and motion measurements quality.

5.6.2.2 Barcelona-El Prat Airport T1 terminal

This section present the results obtained in the Barcelona-El Prat airport terminal T1 area, labeled as A in Fig. 5.3. The scale selected is between 0 and 2 cm/year, adapting to the mean displacement rates detected in this area. As introduced in 3.1.1.1, T1 terminal is located over a delta, a certain settlement is expected on its infrastructure. As it may be
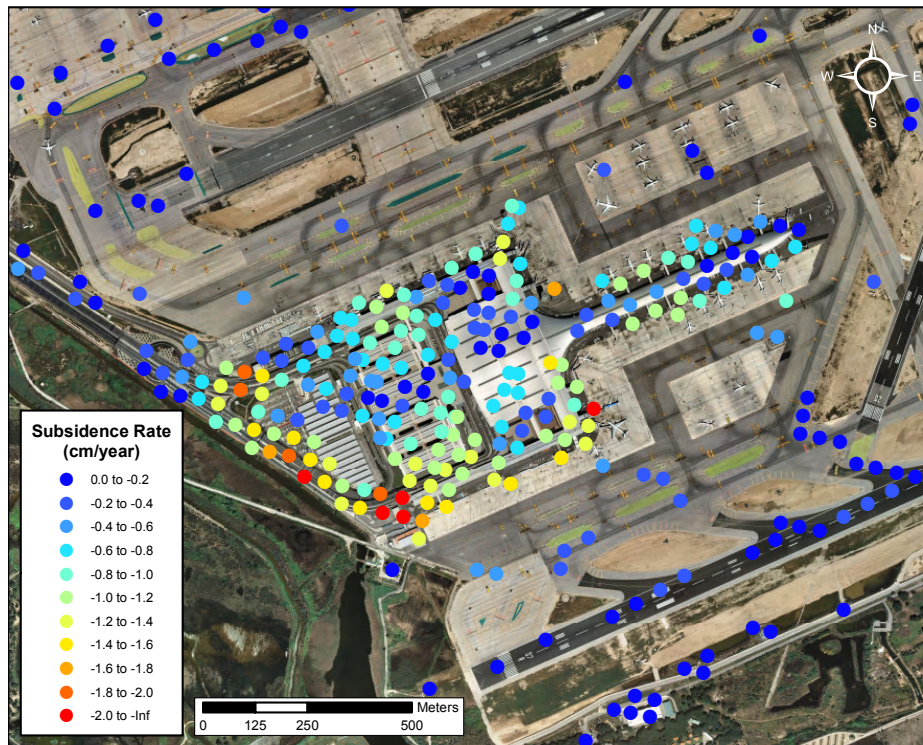
Figure 5.5: Displacement rate results obtained using the ESM-MB optimization on the coherence stability estimator over the Airport T1 terminal.

seen in the overview provided in Fig. 5.5, different areas in the main structure presenting subsidence are found. In fact, as far as the resolution of the coherence stability allows to detect, there seems to exist several focuses mainly in the eastern and southern parts of the building. The maximum mean displacement rate detected is around 2 cm/year.

Comparing these results with the lexicographic basis combination shown in Fig. 4.3, a certain increase in density is observed, specially in the main structure of the building and some runaways. However, the lack in resolution hinders the visual appreciation of the improvement provided by phase quality optimization methods.

Fig. 5.6 provides a comparison between the results obtained using each one of the original channels and the ESM-MB optimized ones. As it may be observed, the density of points and so the characterization of the phenomena is better in the ESM-MB case (Fig. 5.6d) than in the raw channels results. Notice how some points which do not appear in the original channels are now present in the optimized results.
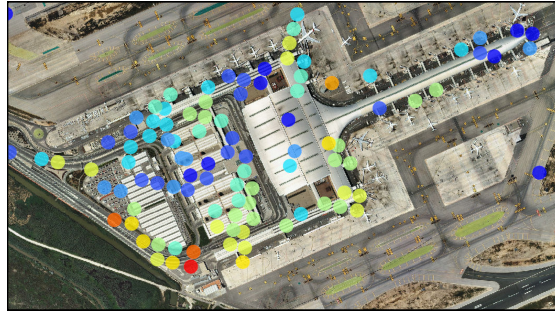
(a)
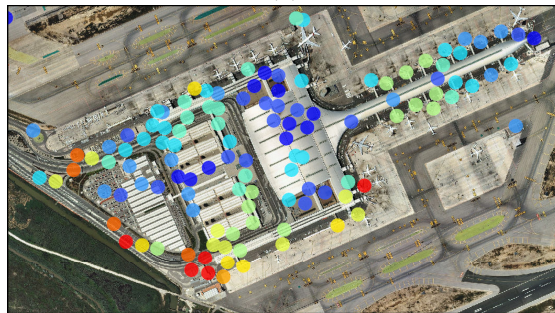
(b)
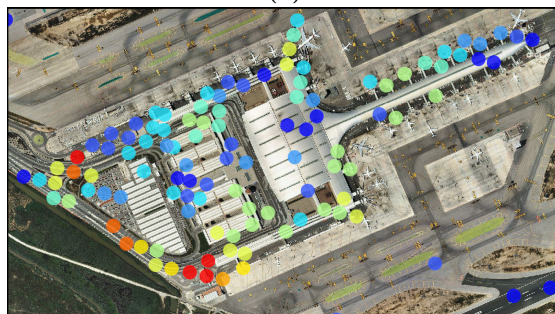
(c)
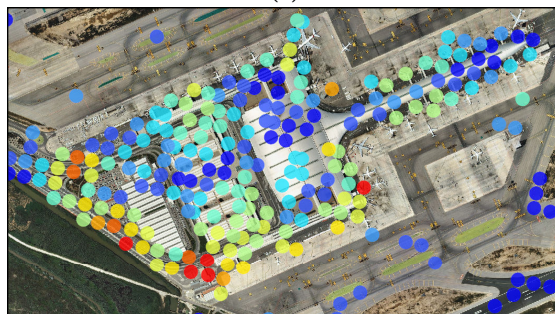
(d)

Figure 5.6: Displacement rate results obtained using the coherence stability estimator over the Airport Terminal T1: HH (a), HV (b), VH (c) and ESM-MB (d).

Figure 5.7: Displacement rate results obtained using the ESM-MB optimization on the coherence stability estimator over the L9 metro line.

5.6.2.3 L9 metro line

Fig. 5.7 show the motion observed along the track of L9 metro line under construction. The scale selected is between 0 and 0.5 cm/year, which is quite near to the noise threshold, since the motion is very low. The results show that the maximum displacement rate detected the ESM-MB optimization approach is below 0.4 cm/year. Since the affected area does not spread much around the metro line track, the the lack of resolution hampers the identification the main focus of displacement, located at Sanllehy square. Some subsidence spots are also obtained in Lesseps square, at the western part of the AOI.

In this case, when comparing the optimization results with the basis combination ones, a clear increase in density is perceived, see Fig. 4.5 for reference. ESM-MB a far more consistent coverage over the whole urban area than the basis combination approach. Fig. 5.8 shows the comparison between channels HH, HV, VV and the ESM-MB optimization results. For convenience the images orientation has been changed, mind the compass on the top/right. As it may be seen, all the results provide a bad spatial sampling of the phenomenon due to the poor resolution. In any case, the more robust results are found in the optimized channel, both in terms of density and displacement measurement.

(a)

(b)

(c)
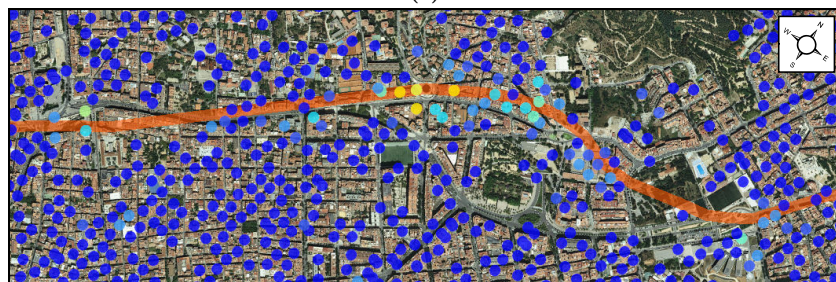
(d)

Figure 5.8: Displacement rate results obtained using the coherence stability estimator over the L9 metro line: HH (a), HV (b), VH (c) and ESM-MB (d).

5.6.3 Amplitude dispersion optimization results

This is the second specific section of results, this time showing the application of the phase quality optimization techniques on the dA estimator. This estimator preserves the full resolution of the data and it is reliable if enough acquisitions are available, which is the case of the data-set used. Moreover, since most of the area monitored contains human-made structures, the estimator is bound to detect high densities of PSs. For all the results obtained, a dA threshold of 0.25 has been used, which is approximately equivalent to 15 degrees of phase standard deviation.

The structure of the results is organized as follows: First some general comparisons between the different optimization techniques described are provided. Then specific results over the different areas of interest are given, with an overview and specific comparisons between the performance of original channels and optimized ones. The same color-bars as in the coherence stability case are used for each location. Moreover, a comparison between the dA estimator and the coherence stability estimator is carried out. To better benchmark the dA optimization, also the comparison with the polarimetric basis combination results in chapter 4 is provided.

5.6.3.1 General results

Fig. 5.9 shows a global view of the ground displacement detected, with all the specific AOI highlighted. As it may be appreciated, equivalent displacement retrieval as in the coherence stability case in Fig. 5.3 is observed, but with higher resolution and pixel density. This should allow for a better identification of the phenomena already detected using the coherence stability estimator in 5.6.2. The following sections give a more detailed analysis on the results obtained, along with a comparison between the optimized and the original results.

The histograms in Fig. 5.10 show the dA index statistical distribution for HH, Best-MB, SOM-MB and ESM-MB. Notice how the improvement in the amplitude dispersion statistics as the complexity of the optimization method increases. A severe reduction of the dA index when using the ESM-MB method compared to the original HH channel is clearly appreciated.

As in the previous case, the pixel selection represented in Table 5.2 is provided, in order to appreciate the increase in terms of PSs density for each optimization method. Also the original channels and the results for the polarimetric basis combination are included for comparison purposes. To ease the interpretation of the results, the increase factor with respect to each original channels is provided.

Comparing the density between Table 5.1 and Table 5.2,the improvement provided by the different optimization methods is quite more significant for the dA than for the coherence stability estimator. Taking as reference the worst original channel, HV in this case, in gen-
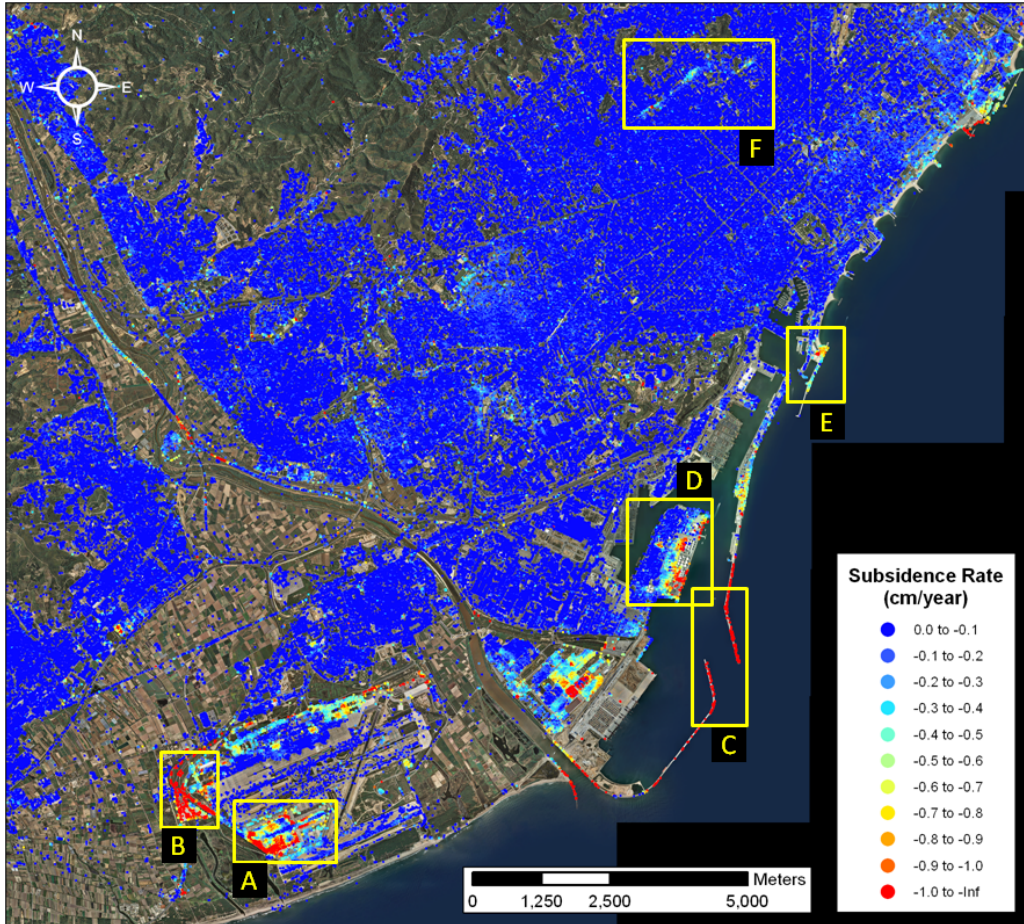
Figure 5.9: General displacement rate results obtained using the ESM-MB optimization on the dA estimator over Barcelona. The different areas of interest are shown from A to F.

eral the improvement in density of PSs is more than 2, 5 and 6 times better for Best-MB, SOM-MB and ESM-MB methods respectively. This is related to the geometric diversity of the high resolution PSs, which is very selective for each polarimetric channel. Then, thanks to the optimization methods, the optimized channel adapts better to any scattering configuration. Now, the comparison with the dA basis combination results is put forward. As in the mean coherence results, the Best-MB provides similar densities as the polarimetric basis combination results using the lexicographic basis. However, SOM-MB results clearly overcome any of the basis combination results, providing improvement factors between 1.5 and 2.2. As always, the better improvement is provided by ESM-MB method, with density multiplying factors between and 1.8 and 2.8 with respect to basis combination results. As for the coherence stability, this is the best approach both in density and quality.
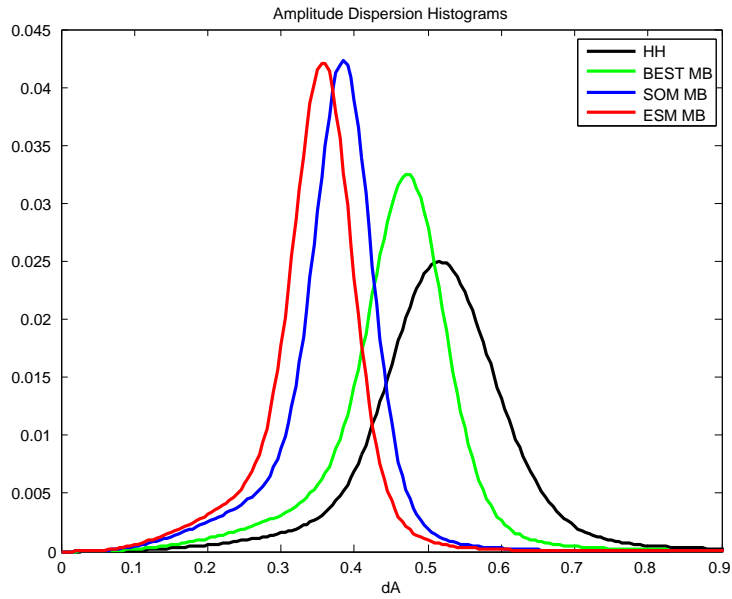
Figure 5.10: Amplitude dispersion histograms comparison, using the HH, Best-MB, SOM-MB and ESM-MB data-sets.

dA:0.25	PSs	Incr. vs HH	Incr. vs VV	Incr. vs HV
HH	92295	1.00	1.10	1.15
VV	83551	0.91	1.00	1.04
HV	80152	0.87	0.96	1.00
Lexicographic comb.	190480	2.06	2.28	2.37
Pauli comb.	204179	2.21	2.44	2.55
Optimum comb.	279215	3.02	3.34	3.48
Best-MB	189623	2.05	2.27	2.36
SOM-MB	421334	4.57	5.04	5.26
ESM-MB	530009	5.74	6.34	6.61

Table 5.2: PSs selected for each data-set. Polarimetric basis combination results are also included for comparison. dA threshold: 0.25

5.6.3.2 Barcelona-El Prat Airport

In this section, the dA subsidence results over the selected locations in Barcelona-El Prat airport T1 terminal are presented. This is an interesting area since its main areas of interest are infrastructures, perfect candidate areas for applying the dA estimator. The scale selected is between 0 a 2 cm/year.
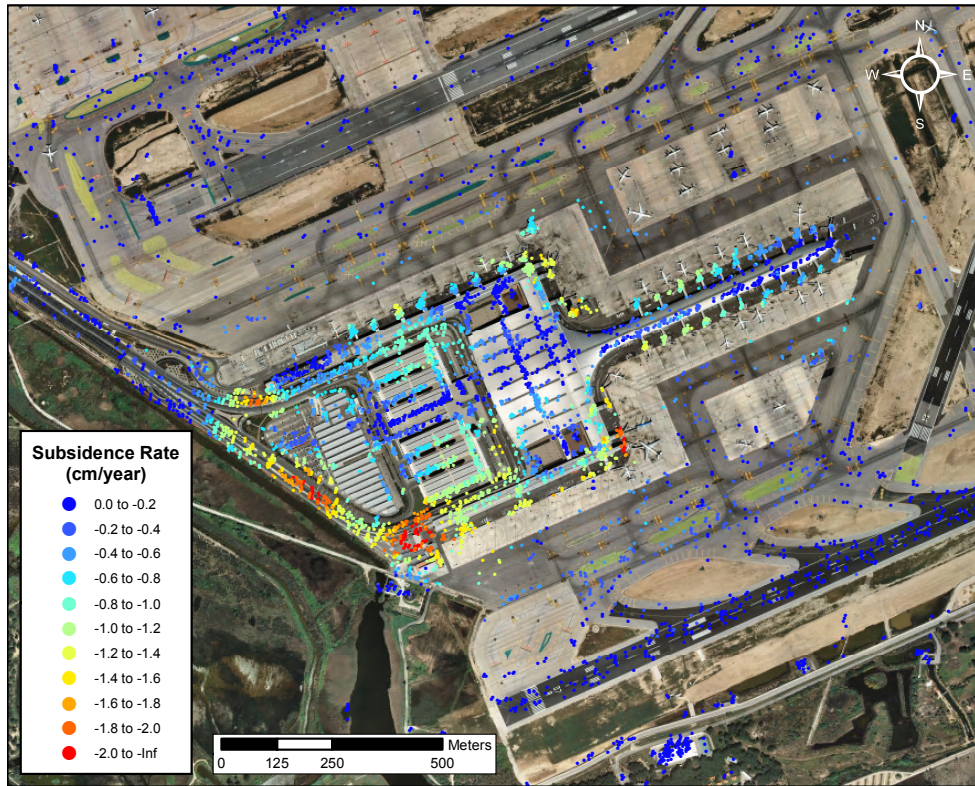
Figure 5.11: Displacement rate results obtained using the ESM-MB optimization on the dA estimator over the Airport T1 terminal.

The results using the coherence stability estimator in Fig. 5.5 suggested the existence of several small focuses of subsidence in the terminal T1 area. The results provided in Fig. 5.11 allow to clearly identify all these focuses, located mainly in the road accesses in the South-West. The maximum displacement rate detected for each deformation bowl is around 2.5 cm/year, affecting areas with extensions below 500 meters. Minor affectation over the building is also observed, presenting displacements rates below 1 cm/year.

The comparison with the optimum base combination results shown in Fig. 4.7 reveals a higher density of points for the ESM-MB ones. Moreover, the optimization adapts to the targets over the scene. This can be appreciated in the positioning of the measurement points, which clearly follow the main structures in the scene.

Fig. 5.12 shows the comparison between the original channels and the ESM-MB optimized one. The information of displacement of each individual focus is present also in the original channels, but the higher density in the optimized results allows for a better extraction of the phenomena extension and behavior. It is worth notice also the significant increase in density over the runways. No relevant motion is detected, but the surveying over this areas is clearly more effective.
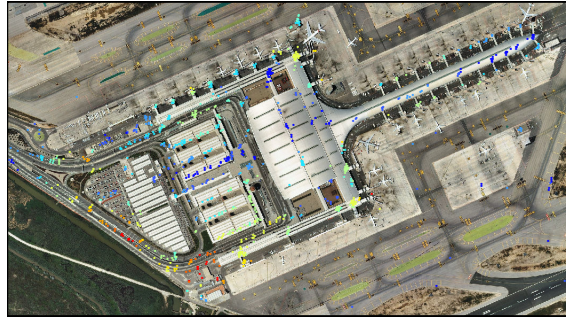
(a)

(b)

(c)
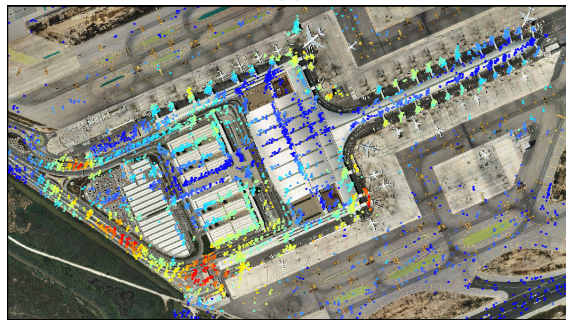
(d)

Figure 5.12: Displacement rate results obtained using the dA estimator over the Airport Terminal T1: HH (a), HV (b), VH (c) and ESM-MB (d).

109
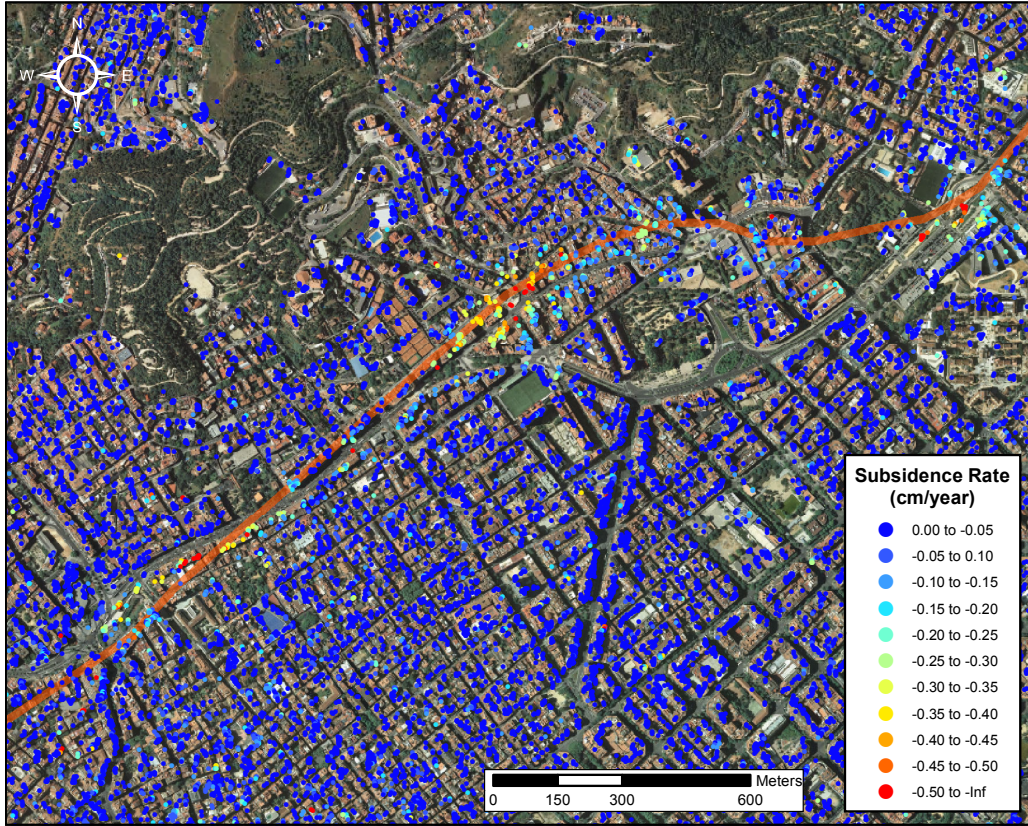
Figure 5.13: Displacement rate results obtained using the ESM-MB optimization on the dA estimator over the L9 metro line.

5.6.3.3   L9 metro line

This section is devoted to present the results obtained over the track of L9 metro line monitored during its tunneling works. Fig. 5.13 presents the general results obtained using the dA estimator along with the ESM-MB data-set. The scale used is between 0 and 0.5 cm/year.

As previously commented, the scale used is close to the noise floor of the measurement, so the representation provided seems slightly noisier than the examples in the previous locations. However, the selected stretching of the values allows to identify the area affected by subsidence during the metro works. Comparing this results with the ones provided by the coherence stability estimator in Fig. 5.7, the three focuses located at the West, middle and East of the area of interest shown, are now clearly identified. Moreover, the areas with the highest subsidence are now recovered, detecting displacement rates above 0.7 cm/year locally.

In this case, the comparison between the optimum base combination in Fig. 4.9 and the results in Fig. 5.7 show a clear increase in density in the latter. Moreover, thanks to the specific sensitivity of the ESM-MB method, the scene is better characterized. For instance, notice the nice adjustment of the PSs to the buildings.

Fig. 5.14 provides the comparison between the original channels and the ESM-MB optimized one for the L9 line results. This is a clear example of the diversity provided by the polarimetric data. Notice the scarceness of PSs provided by each polarimetric channel separately compared to the optimized results. All the different features in the city are clearly identified in the latter, while this is hardly possible in the former assuming the same level of phase quality threshold. Moreover, the identification of subsidence phenomena present is easier thanks to the density provided by the optimization.

111

(a)

(b)

(c)
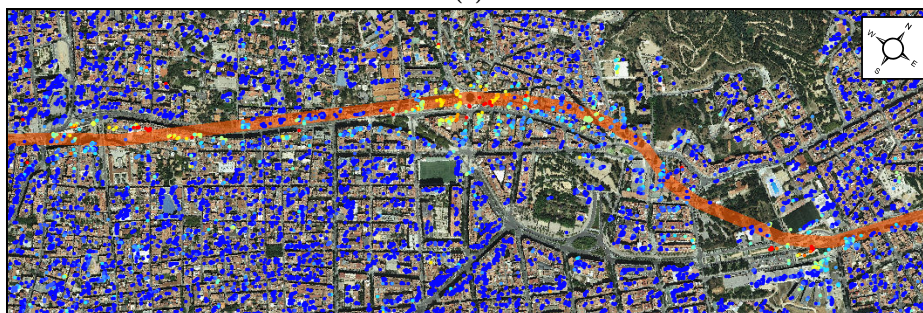
(d)

Figure 5.14: Displacement rate results obtained using the dA estimator over the L9 metro line: HH (a), HV (b), VH (c) and ESM-MB (d).

5.7 Dual polarimetric vs Fully polarimetric quality optimization

A big discussion has arisen in the polarimetric community, concerning the future space-borne mission design, on the importance of the inclusion of fully-polarimetric capabilities. From a theoretical point of view, dual-polarimetric data is not able to completely characterize the polarimetric space, which restricts the capabilities in many polarimetric disciplines. However, the use of fully-polarimetric data reduces the swath by a factor of two in the range direction, which degrades severely the coverage area of the satellite. In the following, the performance in terms of PSs density between dual and fully polarimetric is tested.

5.7.1 Comparison characteristics

The comparison between dual-polarimetric and fully-polarimetric carried out in this chapter is based on the ESM-MB optimization method, since is the one providing the better results. Moreover, SOM-MB requires a fully-polarimetric dataset in order to perform the basis rotation.

The study is done only in statistical terms, since the visual results achieved are very similar to the ones in 5.6. The comparison avoids two main drawbacks of fully polarimetric data:

- Coverage reduction due to the half swath loss in range.

- Highest computational cost of the optimization process.

All this considerations should be addressed in a more qualitative way.

To carry out the analysis in fair conditions, the fully-polarimetric data-set over Barcelona is used, narrowing it down to simulate the several dual-polarimetric modes possible:

- **HH/VV**: Taking the combination of both co-polar channels. This option present the same swath restrictions as the fully-polarimetric data.

- **HH/HV**: First co-polar and cross-polar combination.

- **VV/VH**: Second co-polar and cross-polar combination.

The results obtained in this section are not comparable to the general results in sections 5.6.2 and 5.6.3. In this case, some of the images rejected in the former results are used in the current one, including the snowfall event in 9th March 2010 [34], see chapter 3 for details. Obviously, the global quality of the results is worse, reaching lower PSs
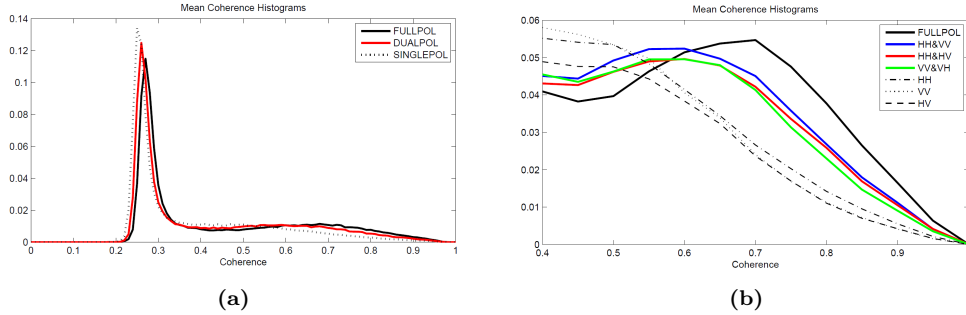
Figure 5.15: Coherence stability histograms for the dual VS fully polarimetric comparison. (a) are the general representative histograms for each case and (a) shows a detail for all histograms in high coherence values.

coher:0.75	HH	VV	HV	HH-VV	HH-HV	VV-VH	Full-Pol
PSs	6060	4675	4796	11390	10961	9709	16469
Incr. vs HH	1.00	0.77	0.79	1.88	1.81	1.60	2.72
Incr. vs VV	1.30	1.00	1.03	2.44	2.34	2.08	3.52
Incr. vs HV	1.26	0.97	1.00	2.37	2.29	2.02	3.43

Table 5.3: Dual polarimetric VS Fully polarimetric PSs distribution for the coherence stability estimator.

densities. In any case, the cross-comparison between dual and fully polarimetric results is still completely valid. This is the results of the specific study done in the framework of Polinsar 2013 Workshop [CA7].

5.7.2 Comparison results

This section provides the statistical comparison between PSI results using the dual and the fully polarimetric data-sets. For the sake of completeness and also to provide a reference of the intrinsic improvement provided by each approach, the results for each single polarimetric channel are also included. The improvement factors respect the latter are also provided. This study is carried out both for the coherence stability and the dA estimators.

Fig. 5.15 shows the quality distribution of the data in histograms. Fig. 5.15a presents 3 representative histograms for single, dual and fully polarimetric results. As it was the case for the previous coherence stability results, the gain is appreciated towards the higher values. In order to avoid the high peak in the histograms related to natural areas, Fig. 5.15b presents a detail of this area in the histograms. Here all the histograms are provided, where the improvement between approaches is clearly appreciated.
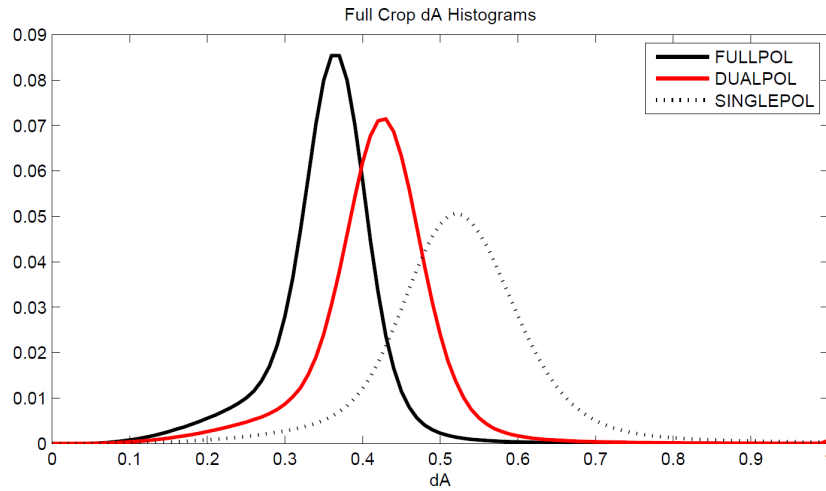
Figure 5.16: Amplitude dispersion histograms for the dual VS fully polarimetric comparison. Representative graphs.

dA:0.25	HH	VV	HV	HH-VV	HH-HV	VV-VH	Full-Pol
PSs	75653	66377	64815	228853	217785	214435	463412
Incr. vs HH	1.00	0.88	0.86	3.03	2.88	2.83	6.13
Incr. vs VV	1.14	1.00	0.98	3.45	3.28	3.36	6.98
Incr. vs HV	1.17	1.02	1.00	3.53	3.36	3.31	7.15

Table 5.4: Dual polarimetric VS Fully polarimetric PSs distribution for the dA estimator.

Table 5.3 shows the PSs density for each case. For this results, a coherence threshold of 0.75 has been used. For each case, the increase in PSs as a multiplying factor with respect to the single polarimetric cases is provided.

Notice how dual polarimetric data-sets provide an increase in density around a factor of 2 with respect the original channels. However, fully polarimetric results overcome the original results by more than a factor of 3 in most of the cases. This representing a 1.5 increase with respect the dual polarimetric options.

As it is the general case, the performance increase for the coherence stability estimator is not dramatic. In the following, the results achieved with the dA estimator are put forward.

Fig. 5.16 present three representative dA histograms for the single, dual and fully polarimetric data-sets. Since equivalent cases present very similar histograms, only examples of each one are included. In this case, a clear gain is appreciated between each general approach.

Table 5.4 presents the PSs density obtained using each one of the data-sets under test. As usual, the factors with respect the single polarimetric results are included.

Respect to the dual polarimetric channels, the results obtained for each are quite similar. The dual-copolar channel option is slightly better, since in general both channels present better response in urban areas. The improvement is in general more than a threefold increase in PSs with respect to original channels.

Taking a look on the fully polarimetric results, they achieve an increase of more than six times the number of original PSs, reaching the factor of seven in two cases. Comparing the dual polarimetric modes, this represents more than a twofold increase in PSs. This is quite significant, since the additional channel in the fully-polarimetric data-set enables a much better density of measurements.

Nonetheless, it is important to stress that dual-polarimetric data-sets provide a good degree of performance with respect to the original channels separately. This is very positive, since many satellites nowadays (2016) have only dual polarimetric capabilities. However, this work has demonstrated than the benefits of using fully polarimetric data make worth considering future missions with these capabilities.

5.8   Conclusions

This chapter discussed the application of phase quality optimization techniques for its use in the PSI analysis. Different techniques have been described and applied to obtain ground motion measurements and evaluate its effectiveness. Moreover, motion results over two specific locations have been included: Barcelona-El Prat airport T1 terminal and a track of L9 metro line under construction. An extensive analysis over more areas is found in appendix A.

PolSAR data acquisitions provide the means to explore the polarimetric space. In other words, if fully-polarimetric data is at disposal, it is possible to emulate any SAR acquisition configuration. From the target detection point of view, the sensor is able to adapt to the scene under monitoring in order to retrieve the better response from it. It has been demonstrated that, since the data-set quality is optimized, the final PSI results achieve higher PSs density and better motion measurements.

A mandatory restriction when dealing with multi-temporal data-sets is than the selected polarimetric transformation must be preserved, at pixel level, for the whole stack of images. This way, the phase component related to a change in the phase center is canceled. Otherwise, this additional component would contaminate the topographic residual and motion estimations during the PSI analysis.

Three different methodologies, Best-MB, SOM-MB and ESM-MB have been proposed and

described. Best-MB relies in the original sensitivities provided by the original channels in the polarimetric basis. SOM-MB methodology takes a step further and applies the basis rotation concept to find the optimum channel. This represents exploring just a portion of the polarimetric space. Finally, ESM-MB exploits the full potential of PolSAR data, reaching the whole polarimetric space to find the optimum sensitivity to the scene.

Each methodology has been applied using the coherence stability estimator as figure of merit. Since the polarimetric basis combination results hinted the 9x5 multi-look as the best option, it has been used as benchmark also for the phase quality optimization results. Better PSs densities have been achieved with respect the original channels, reaching the highest improvement, a factor of 3, with the ESM-MB approach. The comparison with polarimetric basis combination approach provided in chapter 4, shows that ESM-MB outperforms any of the combination results, by factors up to 1.6. The motion maps provided over the AOIs selected highlight the PSs density gain in each area, allowing for a deeper and more precise analysis of the motion under monitoring.

Coherence stability reduces the spatial resolution of our data-set, which may hinder the detection of some phenomena. In order to preserve it, the amplitude dispersion estimator has also been tested along with the optimization methodologies. In this case, the improvement in density is far more important, reaching a multiplying factor of more than 2, 5 or 6 for Best-MB, SOM-MB and ESM-MB respectively. The gain respect to the basis combination results is also higher than in the coherence stability case, where ESM-MB outperforms the best combination by a factor of 3. The optimized sensitivity provided by each pixel allows achieving this improvement.

Of course, this density is clearly perceived in the motion map examples. Thanks to the better sensitivity to the scene, a very good characterization of the targets is provided in the final results. A good example of this improvement is seen in the airport terminal, where the PSs are clearly associated to the main structures. Moreover, the higher density allow for the detection of localized motion events. Notice for instance the L9 line in the urban area. In this case, a subidence phenomena caused by tunneling, which is very narrow in space and low in intensity, can be detected with ease.

Finally, a comparison of the performance of fully polarimetric data with respect to each dual polarimetric mode has been carried out. PSI analysis using fully polarimetric data has demonstrated to overcome any of the dual polarimetric modes. The density increase is around a factor of 2 both for the coherence stability and the amplitude dispersion estimators. However, dual polarimetric modes outperform the density provided by single polarimetric channels by a factor between 2 and 3 depending on the estimator. This is quite positive right now, since most of current satellite missions include only dual polarimetric capabilities.

In conclusion, the phase quality optimization techniques prove to be an useful asset in the PSI framework when PolSAR data-sets are available. Higher measurement densities can be achieved without the need to sacrifice quality requirements.

117

6

PolDinSAR analysis

P HASE quality optimization, as seen in the results presented in chapter 5, provide the means to improve PSI results when PolSAR data is available. Improvement in density has been clearly demonstrated in chapters 4 and 5, both for low and high resolution approaches. The aim of the current chapter is to give an insight of the real improvement in phase quality and hence, in the final measurements retrieved by PSI techniques.

In some of the cases, the physical interpretation of the transformations carried out during the phase quality optimization may be uncertain. The optimized data-set is obtained through a combination of each channel in the original PolSAR basis. The doubt is whether or not this information is related to a physical target, or it only has a mathematical meaning. Then, this chapter addresses this issue and the implications and limitations of the polarimetric transformations.

6.1 Phase quality improvement

The aim of polarimetric optimization is to extract equivalent information from the interferometric phase while improving its quality. It is important to stress that the new phase is equivalent and not equal to the original one since the phase centers may change during the polarimetric transformation. Targets inside the resolution cell presenting the better backscattering behaviour are the ones selected.

Histograms shown in Fig. 5.4 and Fig. 5.10 showed that the different optimization methods provided better values of coherence and dA than the original channels ones. Of course, since the actual estimators are the figure of merit in the optimization, this is quite forced by default. In any case, a direct relation exists between those estimators and the phase standard deviation, see Fig. 2.12 and Fig. 2.15.

To further validate the phase quality improvement, an additional benchmark is proposed. During the PSI analysis, a linear fitting on the PolSAR data-set is carried out, see section 2.3.2. As a result of this process, a quality parameter is obtained, the LMC. In fact, it is not related on the actual pixels but on the links between them. In any case, since the objective is obtain global statistics over the data-set, the links quality is a perfectly valid estimator.

As seen in 2.3.2, LMC is affected by three different artifacts: noise, non-linearities and APS. The main focus of interest for the purpose of this quaility check is the noise. Thus, it is important to consider how the other components affect the LMC.

In general, considering a certain measurement point, it may be assumed that neither non-linearities nor atmospheric artifacts depend on the polarimetric configuration. This is generally true for the APS component, since the path delay suffered by the electromagnetic wave when crossing of the atmospheric layers should not depend on the polarimetric state.

This assumption with non-linearities is not as strong, since different polarizations may retrieve displacement from different physical targets. However, in chapter 4 it has been demonstrated that this events are quite scarce, so they have a low impact on global statistics.

Therefore, changes in the LMC when applying polarimetric transformations should not be driven by these components. Hence, any improvement in this parameter must be mainly related to noise reduction. Fig. 6.1 shows LMC histograms for the channel HH and the different optimization methods employed. A specific zooms on the highest values is given to better appreciate the differences. They show a clear gain in quality as the optimization method increases in complexity.

In the following, two visual examples of these improvement are provided, using data samples of the data-set over Barcelona. They are provided in full resolution to appreciate better the details. In both cases, interferometric phases and amplitudes are presented.
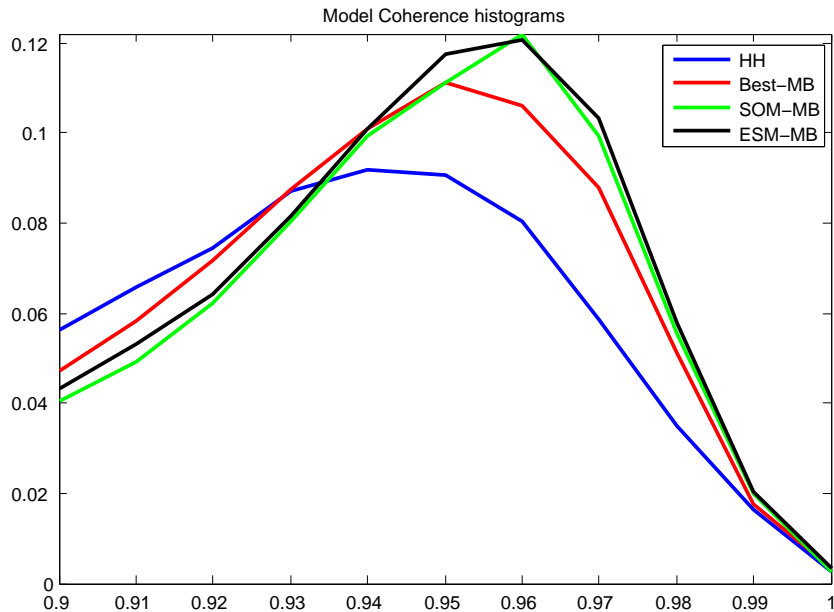
Figure 6.1: LMC histograms of different optimization methods.

This helps evaluating not only the improvement in phase quality but also its effect in the backscattering of the scene. The areas selected are located in Barcelona-El Prat airport T1 terminal and the surroundings of Torre Mapfre and Hotel Arts skyscrapers. Since the general motion events detected in the data-set location are rather low in intensity, phase visual analysis focuses on the topographic component.

Fig. 6.2 gives a general view of the phase quality optimization improvement over a wide area. It includes different kinds of land-cover: The terminal building which includes several point targets, the runways with low backscattering and the natural surroundings. As it may be observed comparing Fig. 6.2a and Fig. 6.2c, the optimization tends to equalize the amplitude in the acquisitions, providing a more homogeneous response of the scene. A good example is found in the point targets along the narrower structure of the building, related to the plane access fingers. The high back-scattering targets are attenuated while the low back-scattering ones are intensified, providing a similar response among all of them.

An interesting case are some point scatterers which tend to disappear after the optimization. This happens when temporal stability is not accomplished, i.e., the targets are not present in all all acquisitions or present high amplitude fluctuation. A clear example, which does not appear in Fig. 6.2, are the outdoor parking areas. All the targets related to vehicles are minimized during the optimization, due to its randomness in time.

Regarding the interferometric phases in Fig. 6.2c and Fig. 6.2d several facts may be observed. The structure of the building is more clearly identified in the optimized phase,

121
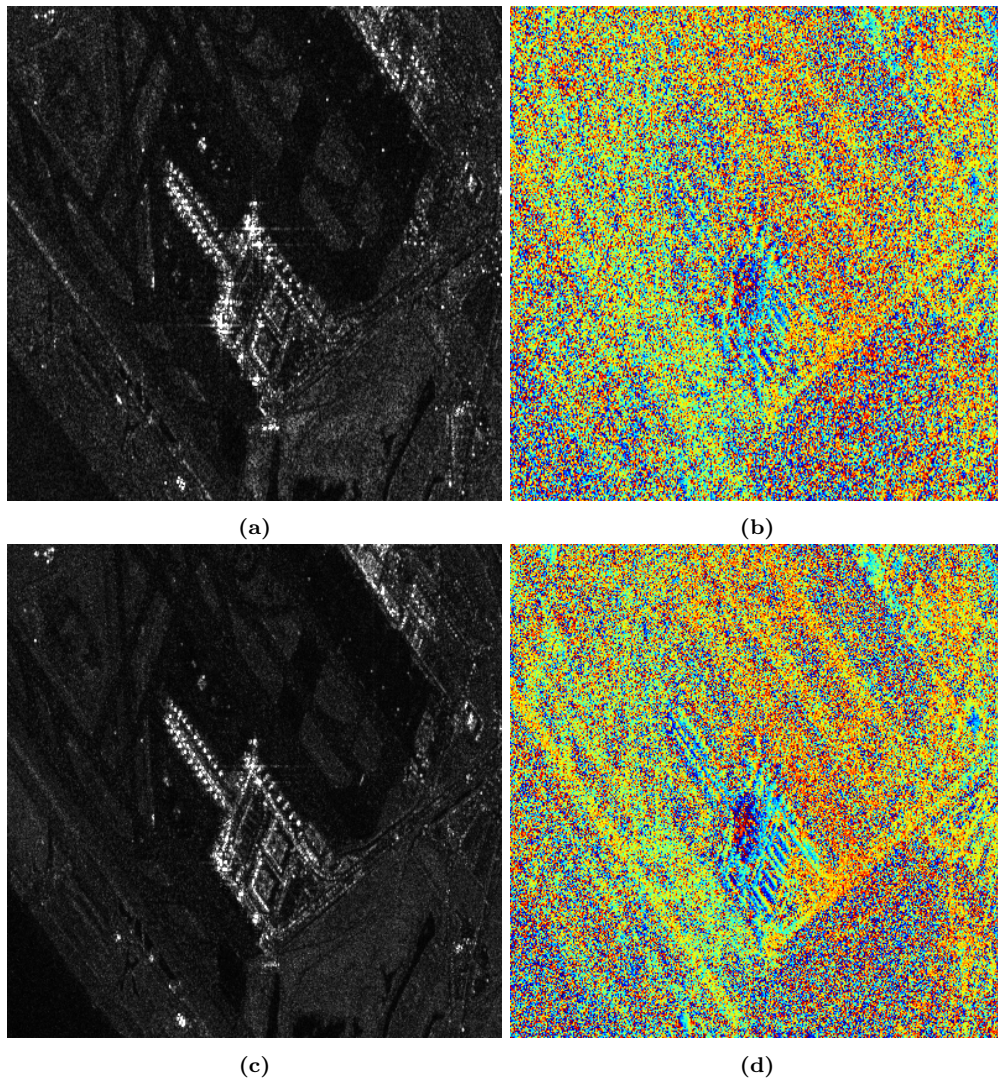
Figure 6.2: Phase improvement visual Example in the El Prat airport T1 terminal. 6.2a and 6.2b present the amplitude and phase of an interferogram in the HH channel and 6.2c and 6.2d is the equivalent optimized inteferogram using the ESM-MB method.

specially the main body, thanks to the phase noise reduction provided by the optimization. Airport runways are more defined as well, and stand out with respect to the unpaved areas. As expected, vegetated areas and water bodies do no present much or any improvement at all after the phase quality optimization.

A more specific example of phase quality improvement may be found in Fig. 6.3, located
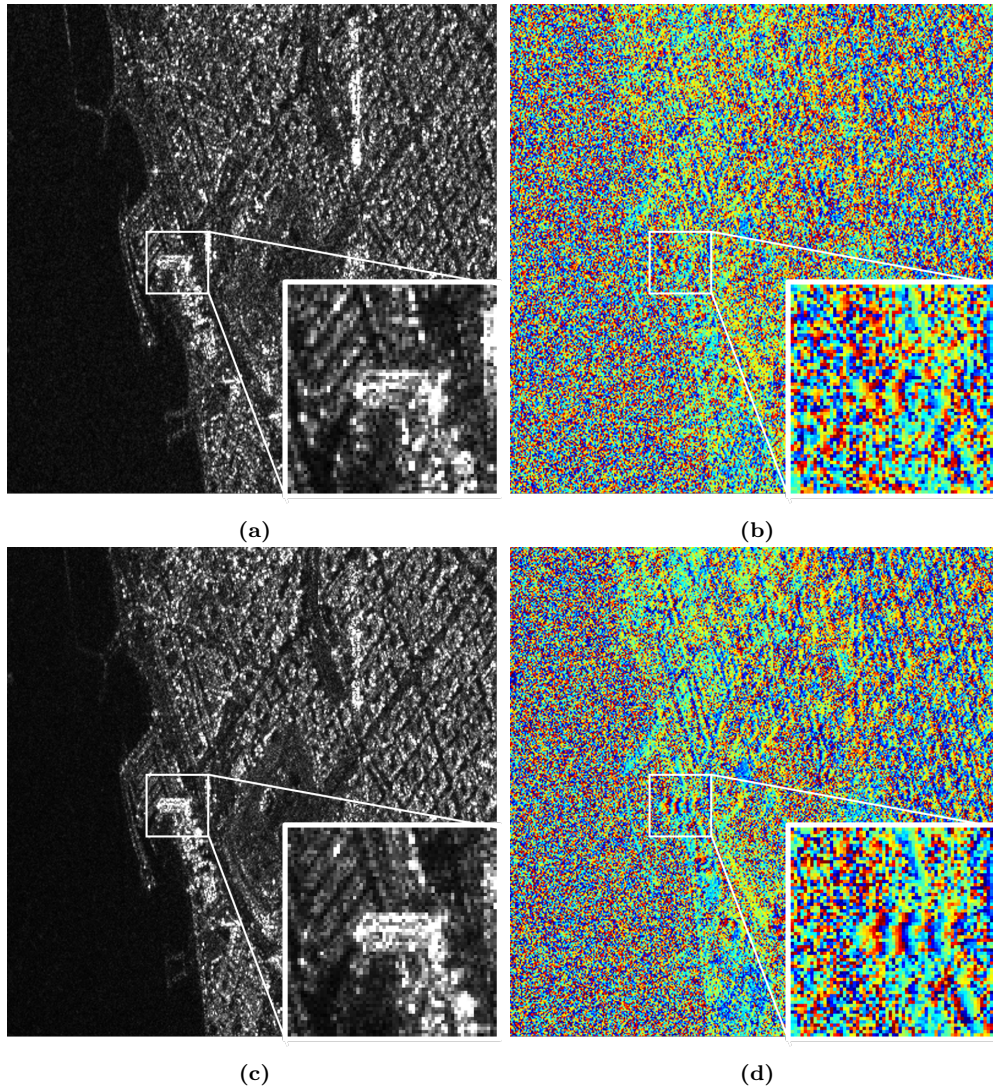
Figure 6.3: Phase improvement visual Example in the Mapfre towers. 6.3a and 6.3b present the amplitude and phase of an interferogram in the HH channel and 6.3c and 6.3d is the equivalent optimized inteferogram using the ESM-MB method.

near the Port Olimpic. This area is characterized by two most emblematic skyscrapers in Barcelona: Hotel Arts and Torre Mapfre. Both buildings were constructed during the Barcelona Olympic Games in 1992, a are more than 150 meters tall. Unfortunately, Torre Mapfre presents an very low backscattering of its structure in the dataset working frequency, in C band. However, thanks to a metallic structure surrounding the building, hotel Arts is clearly identifiable in the PolSAR acquisitions, see zoom detail in Fig. 6.3a

and Fig. 6.3c. Comparing the HH and the optimized amplitudes in the example, the characterization of the tower is far more consistent in the latter, providing an equalized back-scattering of all the resolution cells along the structure of the building. This also applies for the phases in Fig. 6.3b and Fig. 6.3d. Notice that the somewhat noisy response in the HH channel turns to a nice fringe pattern in the optimized case, allowing a good estimation of the building height. A general improvement is also observed in the city, where the phase patterns related to buildings are more clearly identified.

Notice that any kind of spatial restriction has been considered, or in other words, the optimization for each pixel time series is independent from its neighbours. However, the optimized phases achieve more spatial continuity than the original phases. This improvement is obviously related to the effect of the noise reduction. Moreover, it also indicates that the optimization provides phase values which are consistent with the scene monitored. In general one may expect sharp phase jumps in space, provided the independence of each pixel optimization. But this is generally not the case, since this abrupt changes in phase only appear when real physical changes occur in the scene. A good example of this effect is found on the main structure of the T1 terminal, see Fig. 6.3d. The phase characterizing the central part the square section of the building presents a pattern which follows the increases and decreases in height of the structure.

Fig. 6.4 Shows a 3D representation of the Hotel Arts building, with a superimposition of the height in the PSs detected using the HH and the ESM-MB data-sets. This serves as a demonstration of how the improvement of phase quality leads to a better characterization of the scene under monitoring.

6.2 Polarimetric transformations considerations

For a particular resolution cell, phase quality optimization techniques find the optimum polarimetric channel. This channel provides the better scattering response among all the possibilities in the polarimetric space under exploration. This process is summarized in the following scattering coefficient equation,

$$\mu = \boldsymbol{\omega}^H \mathbf{k} \tag{6.1}$$

where different scattering coefficients μ may be obtained adjusting the projection vector ω. Let's consider a target in a PolSAR acquisition. Through (2.56), every possible scattering coefficient is obtained. This μ is characterized by a phase and a quality measurement. This metrics may be represented in a 2D scatter plot.

Consider now an ideal point target, i.e., a single scatterer in the resolution cell. In the scatter plot representation, all points should have a unique phase value, in the phase center of the target, regardless of the quality value. In this ideal case no optimization is necessary, since all the cases provide the right information. However, phase noise may create a certain spread of the phase values around the center. This noise is related to

(a)   **(b)**

Figure 6.4: Topographic error in Hotel Arts. Results for the HH data-set 6.4a and for the ESM-MB data-set. 6.4b.

the phase quality measurement, so the spread of the scatter plot should be higher for low quality points.

The closer real case to the ideal single scatterer is a dominant target in the cell, i.e., a target in the cell which is more significant than the others. By applying polarimetric transformations to the pixel, the significance of the dominant target inside the cell may decrease, giving more relevance to the rest of targets in the cell. Thus, the total contribution in the cell may lead to variations in the resulting phase value. In this case, this also may increase the spread effect in the scatter plot. Fig. 6.5a depicts a case of a real point-like scatterer in this conditions. Since targets shown are the original pixels, the quality employed in the scatter plots is the dA.

125
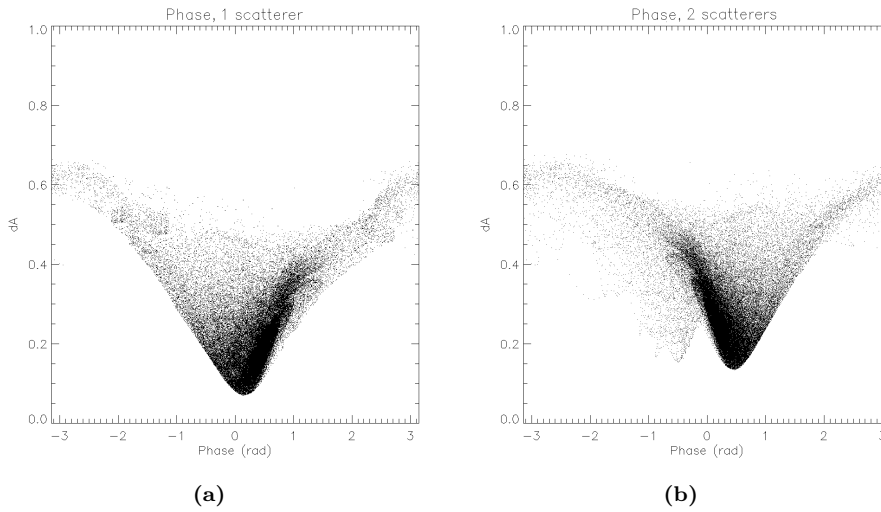
Figure 6.5: Scatter plot phase VS dA examples for (a) a single target and (b) a dual target. Each point represent a different μ transformation.

Another possible scenario is the case where two dominant scatterers with similar response are present in the same resolution cell. In this case, the expected scatter plot is the combination of two point clouds, each one characterizing the phase center of each point-like scatterer. Fig. 6.5b shows an example of this case, when one scatter is more dominant than the other. This is a clear example of the sensitivity of PolSAR data over different targets and the possibility to separate different behaviors in the same cell. By either tuning the sensitivity to either one or the other, the particular motion in each of them may be retrieved.

In a real case, several significant scatterers may be present inside each resolution cell. One of the doubts which arises when dealing with polarimetric optimization is whether or not a nonexistent or fake scatterer may be selected caused by the combination of different real ones. Fig. 6.6 depicts the situation where two scatterers clearly related to physical targets, inside the same resolution cell but with different phase centers, may produce the detection of a nonexistent scatterer. This case will be addressed from now in as *phantom target*. Then, this phantom target would be product of a mathematical combination, lacking of any physical meaning.

As seen in Fig. 6.5, the response in phase of the polarimetric transformation of targets may be quite spread. This behavior may hint the possible existence of phantom scatterers, related to the transition zones between targets.

Mind that the scatter plots shown are related to the phase of an interferogram. In the following, this same effect is analyzed from the multi-temporal perspective, by means of a PSI analysis. As explained in section 2.3, considering a SAR images data-set, PSI is able to retrieve both the mean displacement rate and the topographic error with respect the
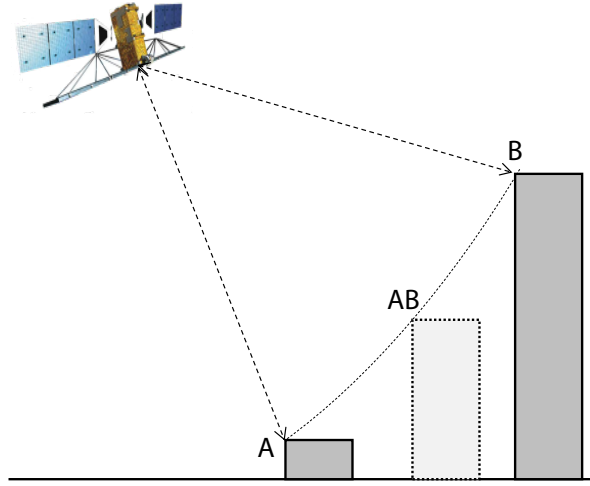
Figure 6.6: Phantom scatterer hypothesis depiction. Scatterers A and B are related to physical targets, while AB has no physical meaning.

<div style="text-align:center">(a)   (b)</div>
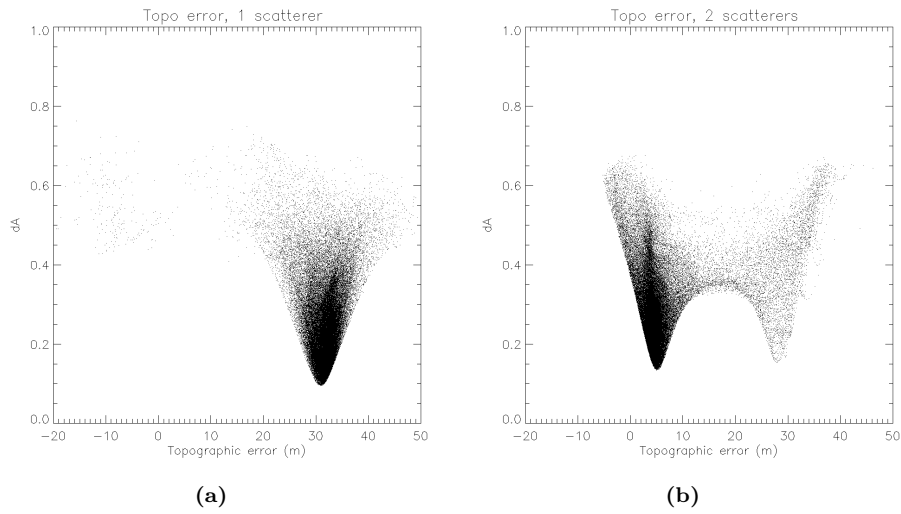
Figure 6.7: Scatter plot topographic error VS dA examples for (a) a single target and (b) a dual target. Each point represent a different μ transformation.

height reference. When dealing with PolSAR data-sets and polarimetric transformation, the topographic error is related to the height of each resulting target. Hence, similar scatter plots as in Fig. 6.5 may be derived, with the topographic error instead of phase. Fig. 6.7 presents the same targets in the previous examples, but with the distribution of topographic error values.

Looking at Fig. 6.7a, which is related to a resolution cell with a single dominant scatterer,

the topographic error values are concentrated around 31 meters. Notice how the spreading of measurements increases for higher dA values. In fact, the graph shows a wider dA dynamic range than the operative one. A dA value of 0.3 may be taken as a very permissive quality threshold. In this range, the values of topographic error are quite consistent.

When observing the dual scatterer case in Fig. 6.7b, both scatterer contributions are clearly seen in the topographic error scatter plot. The number of polarimetric transformations characterizing the dominant scatterer is much bigger than the secondary one. Nonetheless, the latter has enough high quality transformations to be characterized with ease. Note that in the operative dynamic range of dA, both targets are clearly separated. Each zone is only affected by the point spreading due to noise and relevance of the each dominant scatterer. Hence, the detection of a phantom scatterer can not be produced for reasonable quality values.

6.3 Conclusions

This chapter addressed the demonstration, showing different statistics and examples, of the improvement in phase quality delivered by the phase quality optimization algorithms.

Since the figures of merit for the optimization are the actual phase quality estimators, its values increase during the process. Due to their close relation with phase standard deviation, the phase quality increases accordingly. The LMC statistics obtained during the PSI analysis are also provided as a completely different benchmark of the phase quality. LMC has higher values for the optimization methods results, so showing a good agreement with the usual estimators.

Visual examples over some areas have been provided, analyzing the effect of the optimization process over amplitude and phase. In general, optimized amplitudes tend to equalize. Moreover, targets which present an erratic or unstable behavior in time are minimized.

Optimized phases put in evidence the noise reduction provided by the phase quality optimization techniques. Phase features, for instance related to structures and buildings, are more clearly identified in the optimized phases. However, areas affected by temporal decorrelation are neither recovered after the optimization, since they lack of information.

In general, both in amplitude and phase, a higher spatial consistency of the data is achieved. This is caused by the noise reduction, since any spatial restriction has been applied during the optimization process.

The implications of the polarimetric transformations have been analyzed. The concept of phantom scatterer has been defined. It stands for a target lacking of physical meaning, which is a mathematical product of the optimization. An analysis over raw interferometric data and after applying a PSI processing to single characteristic pixels has been carried

out. This analysis suggests that the existence of phantom scatterers is unlikely when applying sensible phase quality thresholds.

In conclusion, optimization techniques not only provide a higher density of measurement points, but also have a clear impact on the phase quality. Therefore, motion measurements retrieved after the PSI analysis of optimized data-set are bound to have a higher quality.

7

CHAPTER 7

CONCLUSIONS

7.1 Main conclusions

The main objective of this thesis was to evaluate the benefits of the use of orbital PolSAR data in a PSI analysis. The higher degree of information included in a PolSAR acquisition has been exploited and evaluated.

To support this study, a fully polarimetric Radarsat-2 data-set over the city of Barcelona has been employed. A total of 38 PolSAR acquisitions were acquired, from January 2010 to July 2012. A subset of 34 images were selected, providing a consistent data-sat to undergo most of the analysis in this work.

Conclusions are separated in different points, following the objectives established in the introduction chapter.

- **Study combination strategies of PSI measurements obtained from each polarimetric channel.**

  Chapter 4 presented the first approach to deal with PolSAR data-sets: Polarimetric basis results combination. Each channel in the polarimetric base is essentially a SAR image. Then, the multi-temporal data-set associated to each channel may be exploited by means of PSI analysis. Through this approach, considering the use of fully polarimetric data, three different motion measurement may be obtained over the scene. Since each data-set is acquired with its own polarimetric configuration, measurements refer to different geometries and distribution of targets.

  The different motion measurements have been combined to obtain a better characterization of the scene. This combination have been done both for the low resolution approach, with the coherence stability estimator, and for the high resolution approach, using the dA estimator. Different polarimetric basis have been tested, including lexicographic, Pauli and the newly introduced optimum basis.

  Two figures of merit have been defined to characterize the goodness of the results:

  - PSs coincidence, which allows for the averaging of equivalent motion measurements.

  - PSs density, which increases the measurement coverage.

  The first hypothesis was that the low resolution approach should provide high pixel coincidence, due to the characteristics of the coherence estimator. This has proven to be dependent both on the polarimetric basis and the multi-look window employed. On the one hand, lexicographic and Pauli basis only achieve good coincidence (up to 50%) for large multilook windows. On the other hand, optimum basis provides a decent degree of coincidence (more than 70%) no matter the multi-look window.

In terms of PSs density, high resolution results widely overcome the low resolution ones. Hence, the low resolution approach should focus on exploiting the pixel coincidence with the optimum basis to improve the quality of the final measurements. The low resolution approach to exploit PSs density should only be considered when the data-set is not suitable for the high resolution approach. This is when the density of point targets or the number of images is low.

The high resolution combination approach delivers the best results, getting PSs densities more than two times the ones provided in the original channels. Moreover, in this case the optimum basis overcomes the others both in density and PSs coincidence. Thus, in this case it is undoubtedly the best approach.

- **Review and establish the necessary theoretical framework for phase quality optimization, for its specific use in a PSI analysis.**

The first part of chapter 5 has been devoted to define the theoretical formalism to undergo the phase quality optimization. Specifically, the particularities of a multi-temporal (or multi-baseline) approach have been discussed.

One of the main points to consider is to avoid the modification, by means of polarimetric transformation, of the scattering phase center over time. In other words, the optimization may not be focused on single interferograms, but to the whole data stack. A single baseline optimization would maximize the phase quality. However, at the same time a random phase component in time would be introduced. Form the PSI analysis point of view, there would be no way to separate it from the topographic residual and the displacement components. Then, it should be treated as a new source of decorrelation. To avoid it, the methodologies employed to carry out the optimization are adressed as Multi-Baseline (MB).

The optimization methodologies used in this work are known as Best-MB, SOM-MB and ESM-MB. They are extensions of their former single-baseline approaches, but taking into account the multi-baseline restriction. On the one hand, in increasing order they present a higher degree of sensitivity over the polarimetric space, thus obtaining a more optimum results at the end. However, the computational cost to carry out the optimization process also increases, which establishes a trade-off in applying one criterion or the other.

- **Analyze the performance and viability of phase quality optimization, comparing the PSI results from single polatrimetric channels and the optimized ones.**

Considering both the results in chapter 5 and in appendix A, an exhaustive PSI results analysis has been carried out. A total of seven specific AOI, described in chapter 3, have been studied.

All methodologies have been tested, using the coherence stability and the amplitude

dispersion estimators. Statistically, the optimized results clearly overcome the original ones. Moreover, as expected, phase quality optimization result provide higher densities than the basis combination approach. In fact, by construction Best-MB presents almost the same performance as the lexicographic basis combination. By extension, this would be reproduced by considering the Best-MB approach on the other basis. ESM-MB is able to obtain a multiplying factor over the density of more than 6 with respect the original channels.

The displacement maps obtained for each AOI confirm the improvement achieved with phase quality optimization algorithm. Some of the phenomena observed in this particular site are quite localized and with low motion rates. The increase in density obtained has allowed to detect an characterize areas that were hardly appreciated in the original channels results.

The adaptability of PolSAR data, specially when preserving the full resolution, makes it a great asset to extract the maximum information from the scene under monitoring. The higher density and quality obtained makes it a worth methodology to apply along with PSI analysis.

- **Asses the comparison between fully and dual polarimetric data, in the specific case of phase quality optimization.**

Some attention has been devoted to the dual versus fully polarimetric controversy. The scientific community, specifically in the SAR Polarimetry field, stresses the need to have consistent sources of orbital fully polarimetric data. The incomplete characterization of the polarimetric space associated with the dual-pol data is usually not enough for many techniques.

In the particular case of this thesis, dual polarimetric data may also be exploited for phase quality optimization, but with a severe loss in performance. The good point is that the optimization process with dual polarimetric data is less computational intensive. Furthermore, most dual-pol modes do not present the half swath restriction of fully polarimetric modes. Depending on the application, this could become a serious advantage.

In terms of PSs density increase, dual polarimetric results still overcome clearly the single polarimetric ones. Then, phase quality optimization techniques are still a good asset considering the current dual polarimetric missions in orbit. However, whenever possible it is recommended to use fully polarimetric, since the performance is doubled.

- **Corroborate the actual improvement in quality of the phase after the optimization to asses its effectiveness.**

The first part of chapter 6 has been devoted to demonstrate the actual gain in phase quality after the optimization process. It is quite obvious that the estimator

values improve, since they are the parameters to optimize. Then, since estimator values are better, so do the phase as well, knowing the close relation between phase standard deviation and each estimator.

However, to provide a more solid demonstration of this improvement, an additional estimation of the quality has been provided: the Linear Model Coherence. LMC is not related to the phase quality directly, but it is a internal PSI quality factor. However, this parameter has proven to be sensible to the optimization process, obtaining better estimates of the LMC value. As the other components which affect this parameter have almost no relation with the polarimetric transformations, the improvement in LMC is basically due to phase noise reduction.

Some examples over the actual phase have been provided, demonstrating in a visual way the improvement both in the amplitude and in the phase quality.

- **Analyze the implications of polarimetric transformations and its physical meaning.**

Phase quality optimization is basically based on a complex linear combination of several SAR acquisitions. Somehow, the data in each channel of the polarimetric base is the result of an interaction of the electromagnetic wave and physical targets. Thus, the mathematical combination of different channels could loose this physical meaning.

The second part of chapter 6 has been focused on refuting this statement. This event has been defined as phantom scatterer, i.e., a fake target generated as product of optimization. An analysis over the possible transformations of a pixel including first a single target and then a dual target has been carried away. This analysis has been done over the actual phase and also including the whole data-set,through a PSI analysis.

The analysis has been done inspecting this information in scatter plots. This scatter plots related the quality values with the phases product of any possible polarimetric transformation. The conclusion of the analysis stands that, for reasonable quality thresholds, the existance of phantom scatterers is unlikely.

7.2   Future research lines

To provide a continuity to the research line opened in this thesis, different future lines may be considered, listed in the following.

- **Analysis of PolSAR data in further frequency bands.**

  Some studies in this field of work have been done already in X-band, using TerraSAR-X and TanDEM-X dual polarimetric images [38, 41, 42]. However, it would be interesting to test L-band data from ALOS, which provides a completely different sensitivity over the scene. This will allow exploring the performance of phase quality optimization in a natural environments, where L-band data would be less affected by temporal decorrelation.

- **Analysis of areas characterized by distributed scatterers.**

  Following the line of the previous point, it would be nice to further exploit the possibilities of the coherence stability estimator. A perfect candidate to test the behavior of coherence optimization would be a volcanic area, which is characterized by high quality distributed scatterers. This scenario would allow also to test the TSC optimization, since this estimator should have a good behavior in this kind of scenarios.

  Another option would be trying it on a natural environment. This should be feasible, as said in the previous point, with the appropriate frequency band, and if possible, with a short revisiting time. With this setup, it would be easy to evaluate the improvement due to the increase in sensitivity provided by PolSAR data.

- **Extend the application of optimization methods using other figures of merit.**

  This work has focused on the traditional phase quality estimators: coherence stability and amplitude dispersion. Moreover, the TSC estimator has been introduced but not put to test in the final results. This estimators are directly related to the phase quality, since a direct relation between them and the standard deviation has been established, see section 2.3.1. Thus, its optimization focuses on improve the PSI analysis input data to reduce the phase noise.

  Other approaches may be explored, since other figures of merit have proven to be sensitive to the improvement provided by phase quality optimization. For instance, consider the LMC parameter product of the linear fitting carried out during the PSI analysis. This parameter has been used as an alternative benchmark to confirm the goodness of the optimization. It could be a good candidate to be directly used as figure of merit in the optimization. Of course, since this estimator tries to adjust the data to a linear model, it should be assessed if phase noise is not compensated

136

by over-fitting.

The optimization methods described are sufficiently generic to be applied to any new estimator which may be implemented. Then, for sure there is room for improvement in this topic.

- **Exploit the current dual polarimetric database.**

  Taking a look at Table 1.1, there is a huge dual polarimetric data archive nowadays. We find TerraSAR-X, TanDEM-X and Cosmo-skymed constellation at X-band and Envisat, Sentinel-1A and Sentinel-1B at C-band.

  This thesis had provided an internal comparison using narrowed down fully polarimetric data-sets, with acceptable performances. So for sure it deserves further attention, considering this amount of data available.

  Another interesting aspect, related to dual polarimetic data, is the appearance of compact polarimetry [43]. It basically consist in emitting a 45 degrees oriented linear polarization or a circular polarization and then receiving with the usual vertical and horizontal polarization. This technique has the potential to emulate certain characteristics of fully polarimetric data. Nowadays it is only available in some satellites, such as ALOS-2, as an experimental mode. In any case, compact polarimetry may be simulated using fully polarimetric data. Thus, an assessment of its performance in phase quality optimization techniques is possible. This would be an interesting topic for future operative missions including compact polarimetry modes.

- **Characterize the polarimetric component in the interferometric phase.**

  As stated in section 5.1, there is one of the mandatory conditions to apply phase quality optimization in a multi-temporal analysis. This is to preserve the same polarimetric transformation throughout the whole PolSAR data stack. This way, the phase component related to changes in the phase center of the targets is canceled. If this is not accomplished, a random variation in time of the phase center would surely impact on the estimation of the motion and topographic residual components. Then, it would become a new source of decorrelation.

  This is currently the only way to exploit optimization techniques for PSI analysis. An interesting research topic would be trying to characterize this polarimetric component. If this issue is resolved, it would be possible to apply the DSM approach, in a single-baseline approach, to further increase the performance of the optimization.

  Moreover, the implications of polarimetric stability should be analyzed. Real changes in the scattering component over time are currently treated as a source of decorrelation, as stated in section 2.2.4. The availability of PolSAR data should provide

137

the means, considering the characterization of the polarimetric component proposed above, to further analyze this decorrelation and compensate for it.

A

PHASE QUALITY OPTIMIZATION RESULTS OVER SPECIFIC AOI

This appendix is devoted to extend the analysis of the phase quality optimization results over additional areas. Different locations presenting subsidence have been detected, see chapter 3. In particular, the following areas are described:

- Barcelona-El Prat airport access road: Area B in Fig. 3.2.

- Port de Barcelona: The harbor contains different areas with motion, including the breakwaters (area C), the Energy Bay (area D) and W Barcelona hotel (area E), all shown in Fig. 3.3.

In the following sections, the results obtained for both coherence stability and amplitude dispersion estimators are provided.

A.0.1 Coherence stability optimization results

This section shows the low resolution results over the areas described. The 9 lines by 5 samples multi-look window has been selected, with a mean coherence threshold of 0.68 (10 degrees of phase standard deviation).
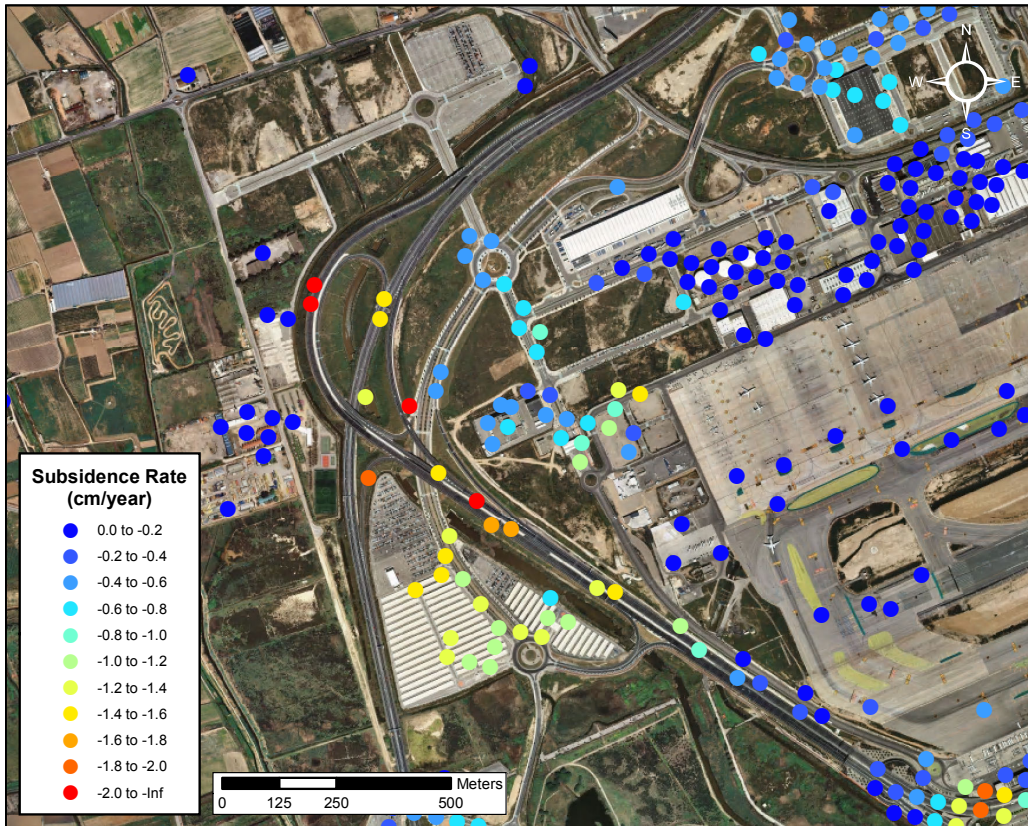
Figure A.1: Displacement rate results obtained using the ESM-MB optimization on the coherence stability estimator over the Airport main access road.

A.0.1.1 Barcelona-El Prat Airport access road

This section present the results obtained area B, the Barcelona-El Prat airport main road access to the facilities. The scale selected is between 0 and 2 cm/year. This area is not favorable for its monitoring, for several reasons. The main structures present are the highways. There are also big parking areas which are bound to be affected by high temporal decorrelation. Moreover, the natural surroundings are either vegetated or cultivated, since scarce measurement points will be retrieved.

The zone around the parking area presents subsidence. The PSs coverage is rather poor, as expected. Some points are found over the highways, as far as the resolution provided by the coherence stability allows. The parking area present points mostly on the zones with parapets, since there the temporal stability is more preserved. Mean displacements up to 2 cm/year are detected in some spots.

A comparison between the the original channels results and the optimized one using the
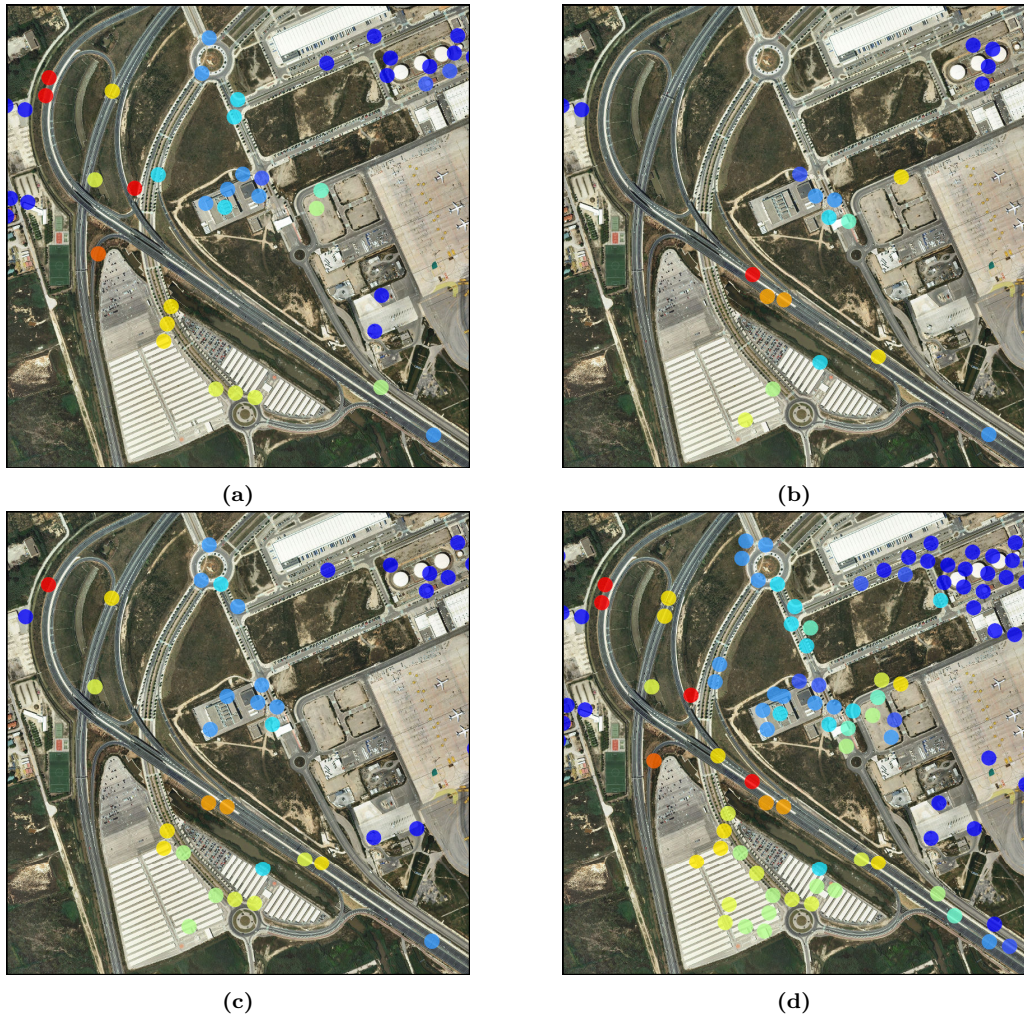
Figure A.2: Displacement rate results obtained using the coherence stability estimator over the Airport access road: HH (a), HV (b), VH (c) and ESM-MB (d).

ESM-MB method is provided in Fig. A.2. Due to the temporal decorrelation which affects this area in general, the improvement provided by the ESM-MB method is low. This example shows how the optimization methods do not provide new information, it simply reduces the noise. When only noise is present, the optimization is useless.
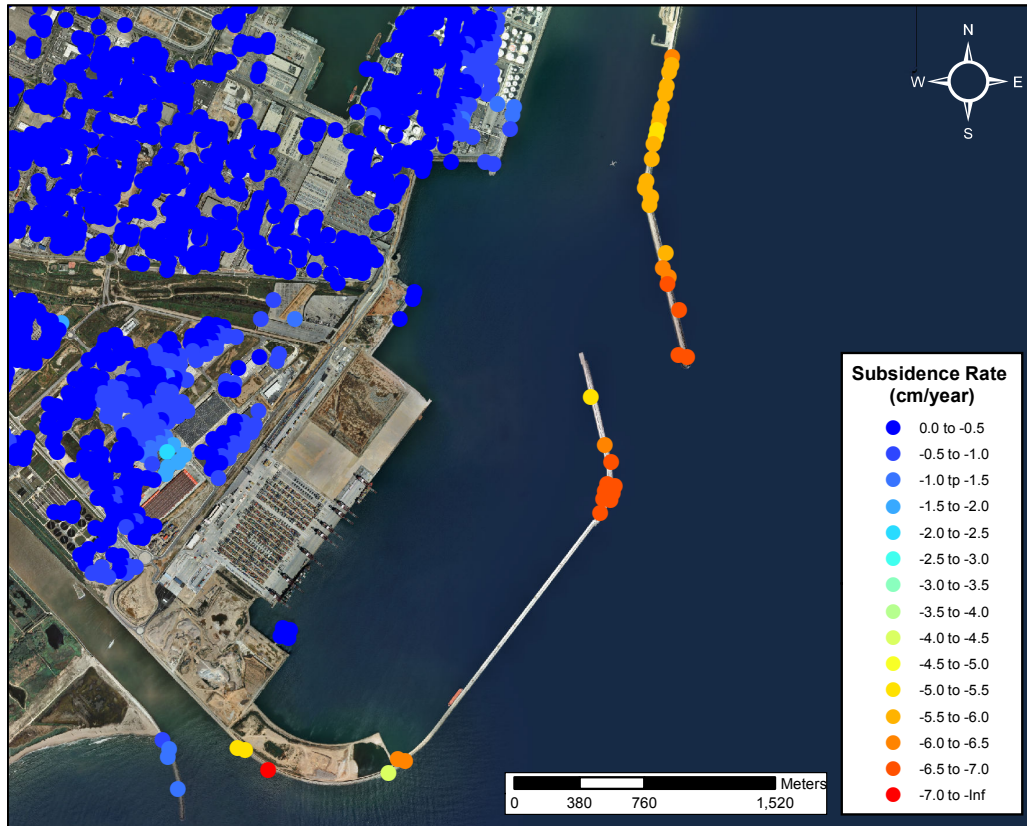
Figure A.3: Displacement rate results obtained using the ESM-MB optimization on the coherence stability estimator over the harbor breakwaters.

A.0.1.2   Port de Barcelona

This section will provide the subsidence phenomenon detected in the zones selected over the Barcelona main port area: the breakwaters, the Energy Bay and W barcelona hotel. Due to the high displacement detected, the former area is given in a scale between 0 and 7 cm/year. The last two zones are given both in a scale between 0 a 1 cm/year.

Fig. A.3 presents the general results over the most critical area in the main breakwaters. This is the zone presenting the highest displacement in the whole area under monitoring. On the one hand, the North breakwater has a good PSs sampling which allows to appreciate a gradient towards the end of the structure, ranging from 5 to almost 7 cm/year. On the other hand, the South breakwater present a poorer sampling probably due to the orientation of the structure. This hypothesis is being reinforced for the fact that the main accumulation of points is located towards the end, where, the orientation changes to better match the North breakwater. The bending area in the South breakwater present similar displacements of almost 7 cm/year. This results agree quite well with the one
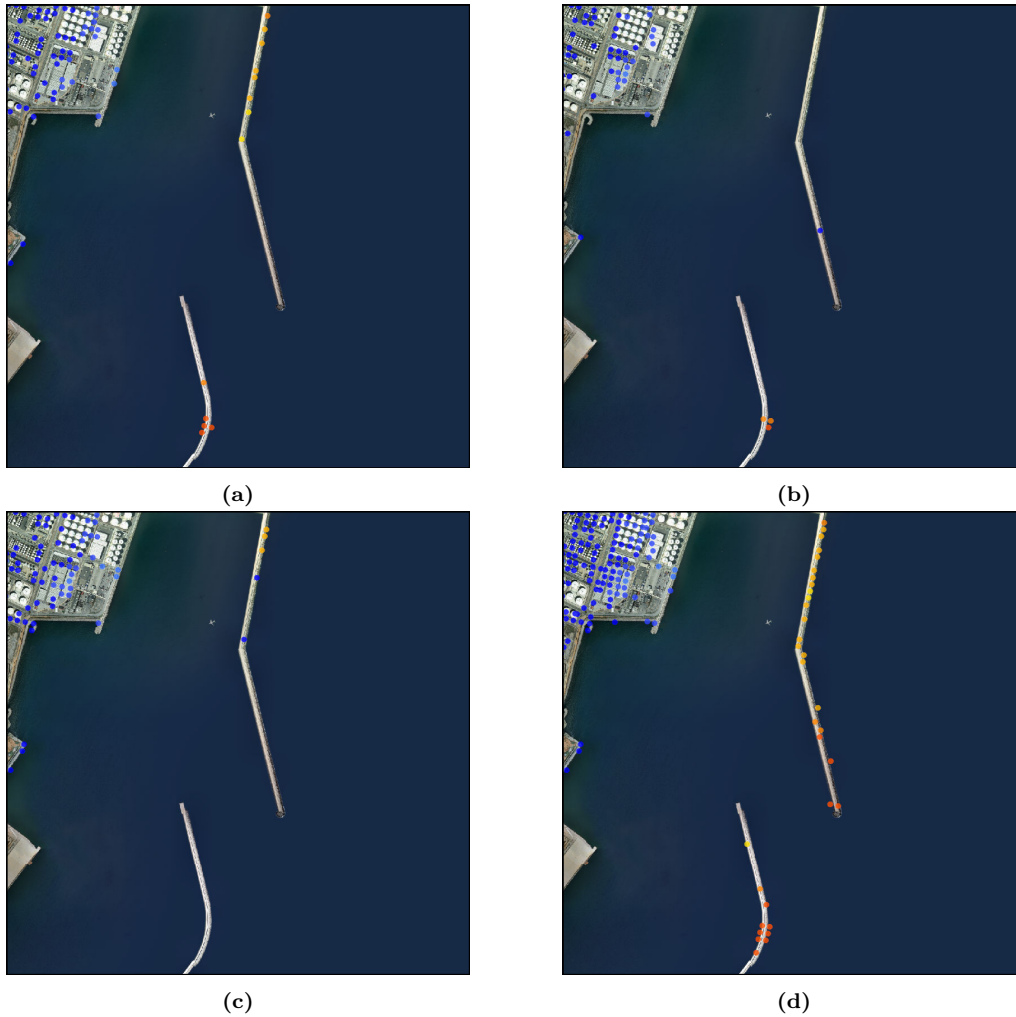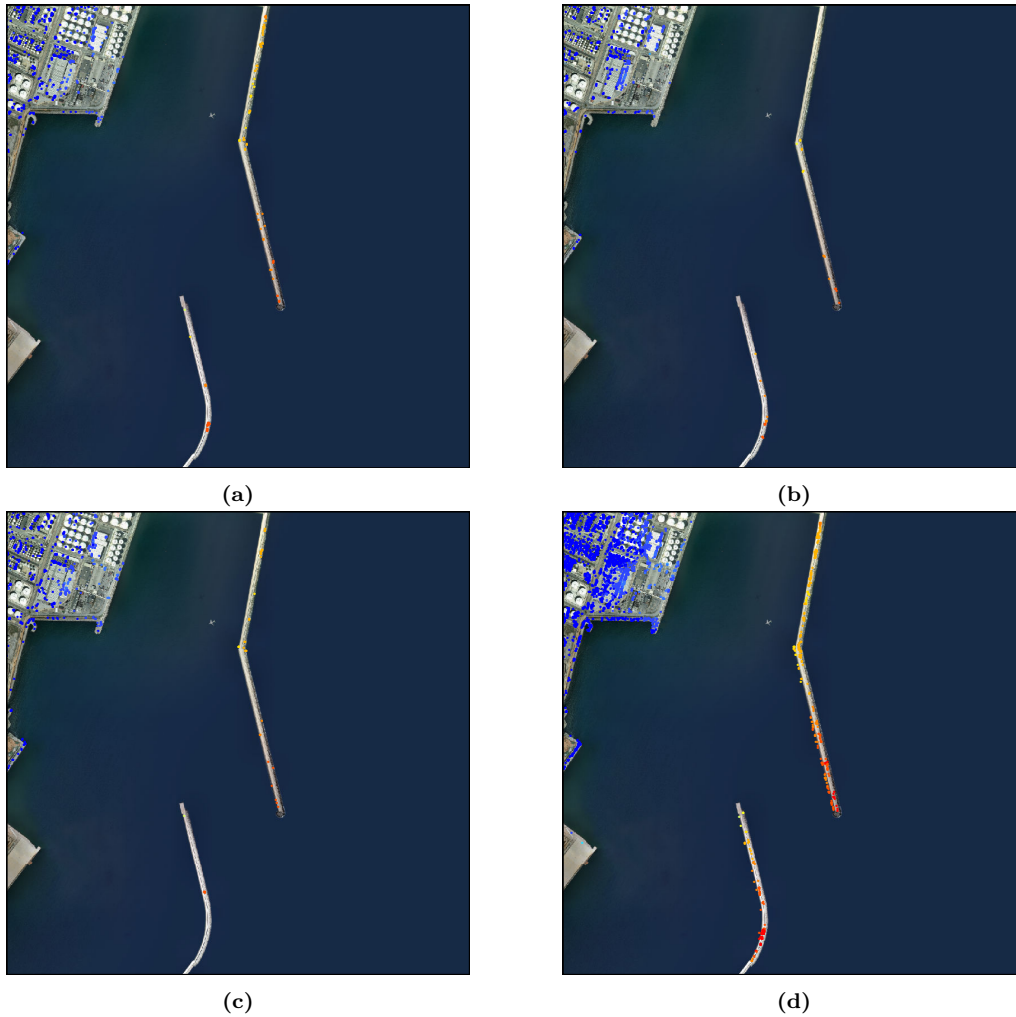
Figure A.4: Displacement rate results obtained using the coherence stability estimator over the harbor breakwaters: HH (a), HV (b), VH (c) and ESM-MB (d).

provided in [33] using a TerraSAR-X data-set.

Fig. A.4 shows the comparison between the results obtained using the original channels and the ESM-MB optimized one. As it may be appreciated, this area is quite critical due to its morphology. The alignment of the points hampers the good retrieval of the displacement when the PSs sampling is poor. For instance, the results for the HH channel in Fig. A.4a does not provide any point on the final section of the North breakwater. Even worse, the HV and VV channels also are affected by phase wrapping issues, since the points detected in this area do not present any subsidence. This is a clear example where the density and quality provided by the optimization methods is almost mandatory to achieve a good displacement detection.
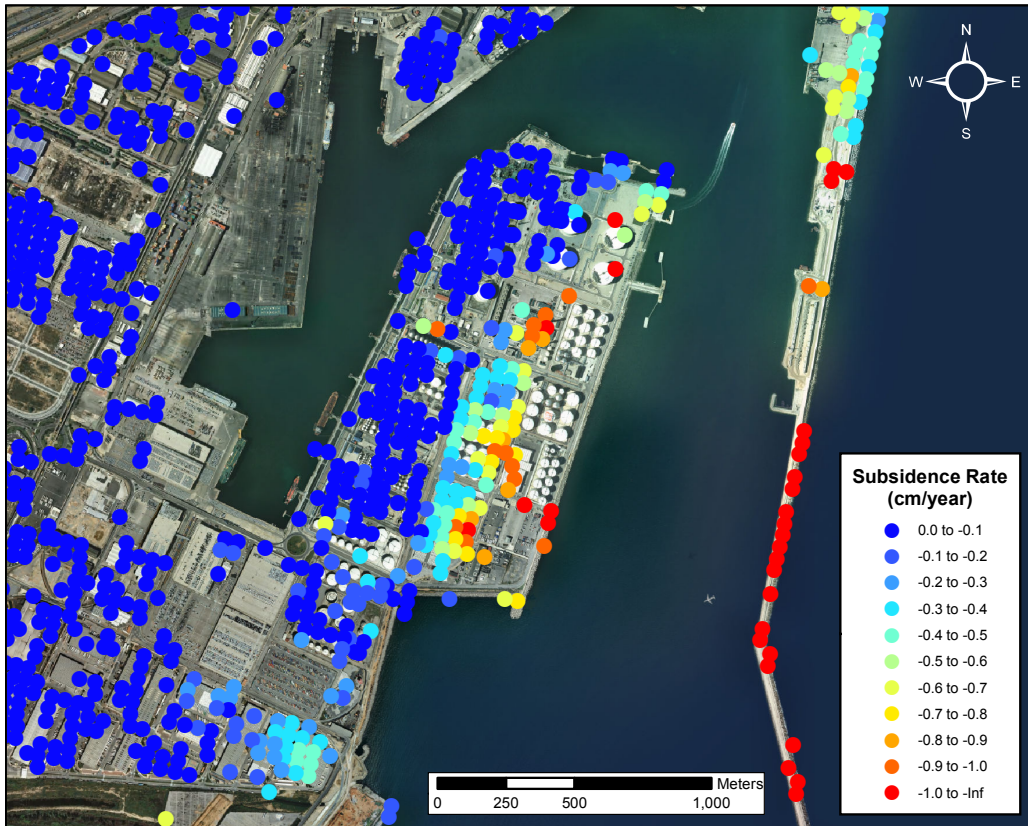
Figure A.5: Displacement rate results obtained using the ESM-MB optimization on the coherence stability estimator over the harbor Energy bay.

The Energy Bay is located at the main harbor premises, inside the area closed by the breakwaters. Fig. A.5 present the general results in this zone. A subsidence gradient is observed in whole area, increasing towards the sea, suggesting a possible tilt of the artificial peninsula. The western section of the area presents stability, except some small localized spots. The maximum displacement detected is around 1 cm/year. Notice how in the figure also appear the results over the breakwaters. Since the color bar sensitivity has been adapted to better appreciate the results over the Energy Bay AOI, the results over the breakwaters appear completely saturated.

Fig. A.6 presents the comparison between the original channels and the optimized channel. While the PSs density increases when using optimization techniques, the improvement in this area is not drastic, since the overall quality of the interferometric phase for each channel is already high. In any case, the characterization of the displacement is easier in the optimized case. Moreover, the localized spots, which appear separately on each individual channel, are collected altogether in the optimum results with improved quality.
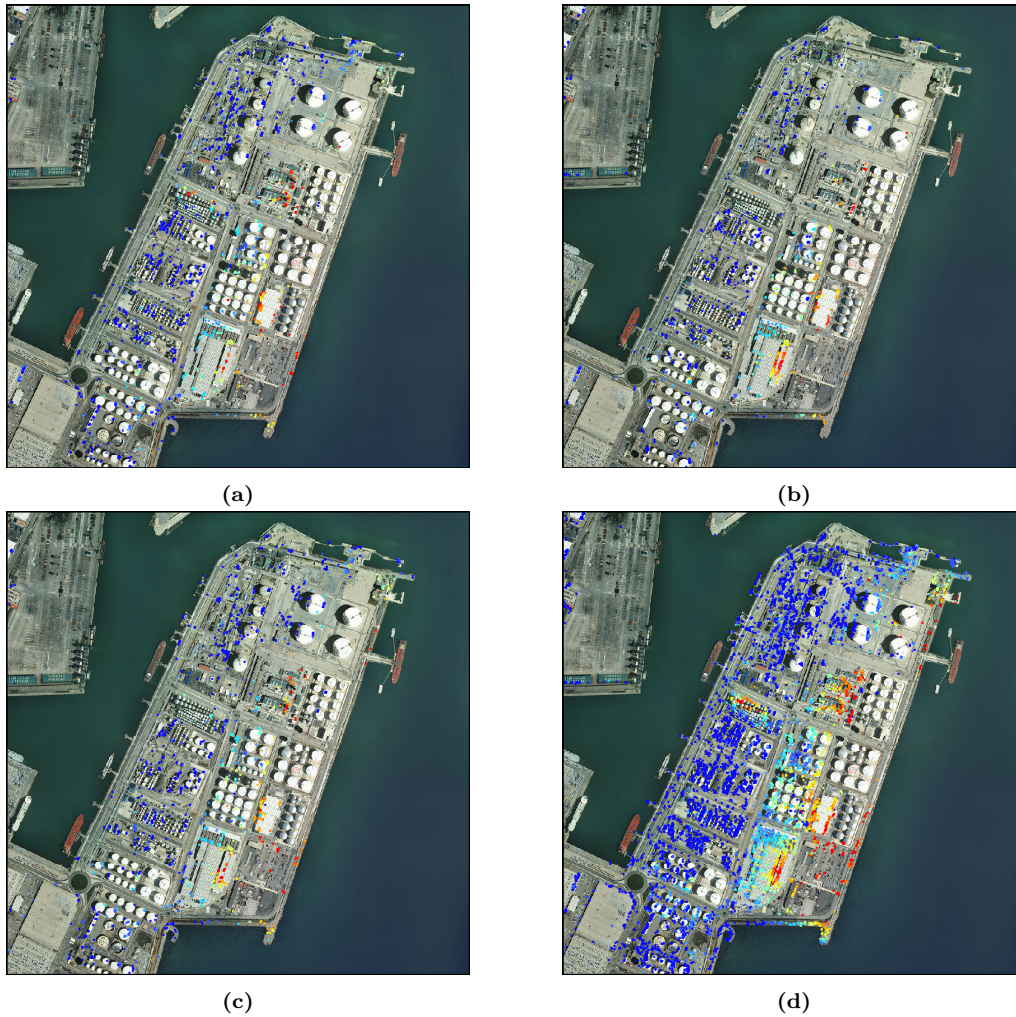
144
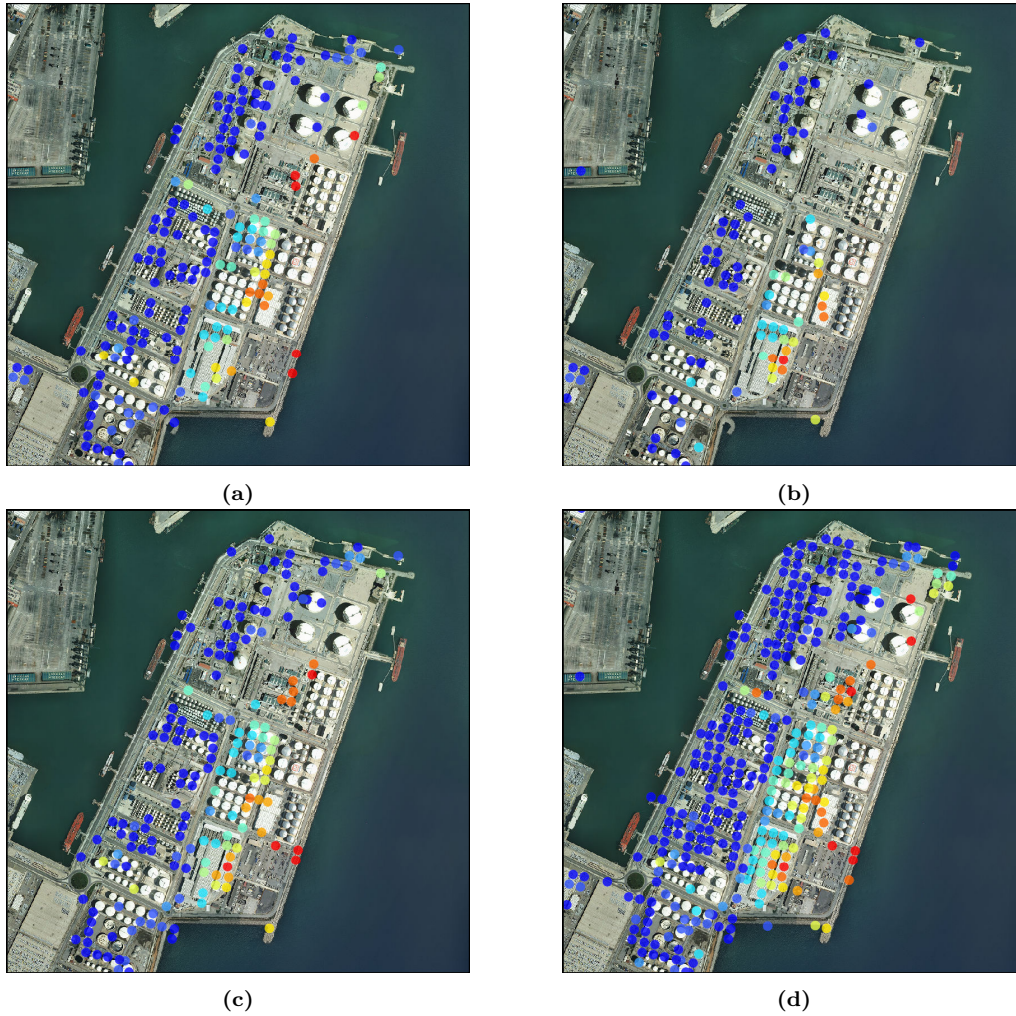
Figure A.6: Displacement rate results obtained using the coherence stability estimator over the harbor Energy bay: HH (a), HV (b), VH (c) and ESM-MB (d).
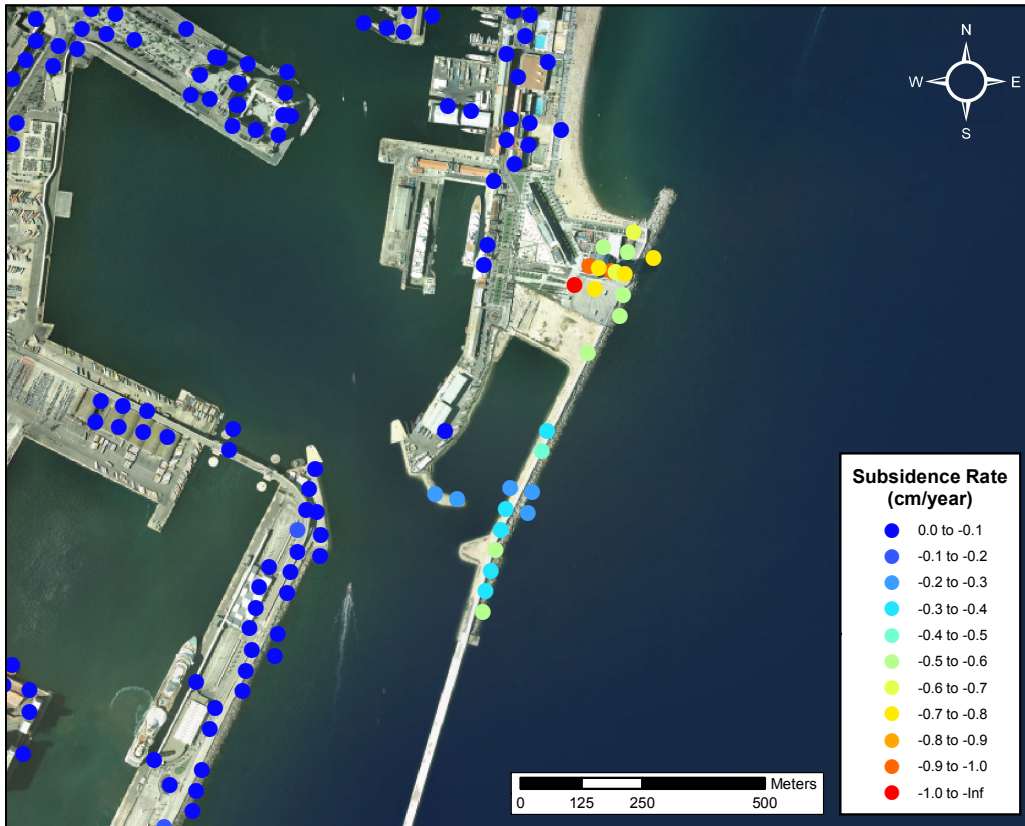
Figure A.7: Displacement rate results obtained using the ESM-MB optimization on the coherence stability estimator over Hotel Vela.

Fig. A.7 shows the results over the W Barcelona hotel area. This is a rather localized zone, so PSs sampling issues are expected due to the multilook applied. In any case, some specific spots are obtained in the area around the building, presenting displacement rates below 1 cm/year. A little far from the hotel, a small motion spot is also appreciated at the first section of the breakwaters, with displacement rates not higher than 0.6 cm/year.

In this case the density of measurement points is not much high in any case. Not as the results for each original polarimetric channel are rather poor. The optimized one is slightly better, since it provides the means to discriminate clearly between areas affected by motion from the ones presenting stability. In this case, probably due to the geometric characteristics of the elements in the AOI, it is easy to identify several measurement points in the optimized results which where not present in any of the original polarimetric channels.
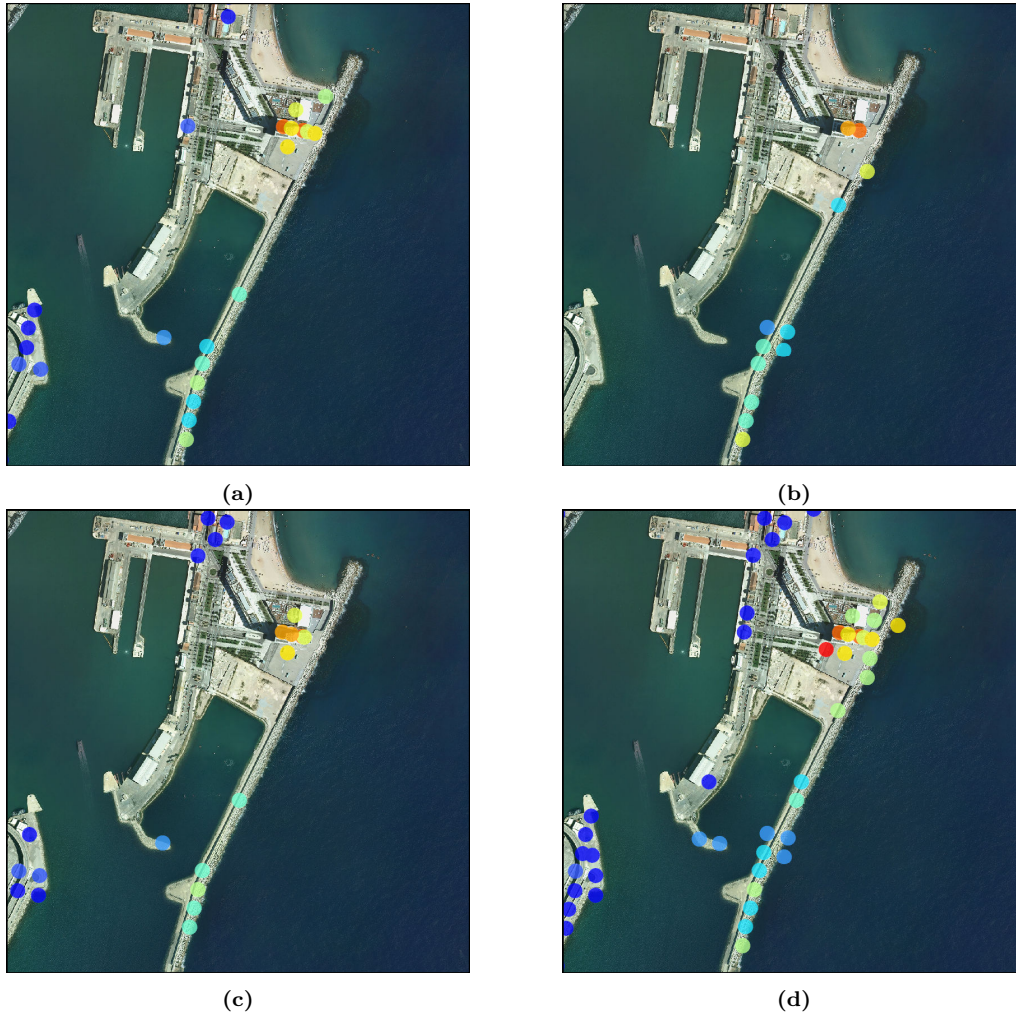
Figure A.8: Displacement rate results obtained using the coherence stability estimator over Hotel Vela: HH (a), HV (b), VH (c) and ESM-MB (d).
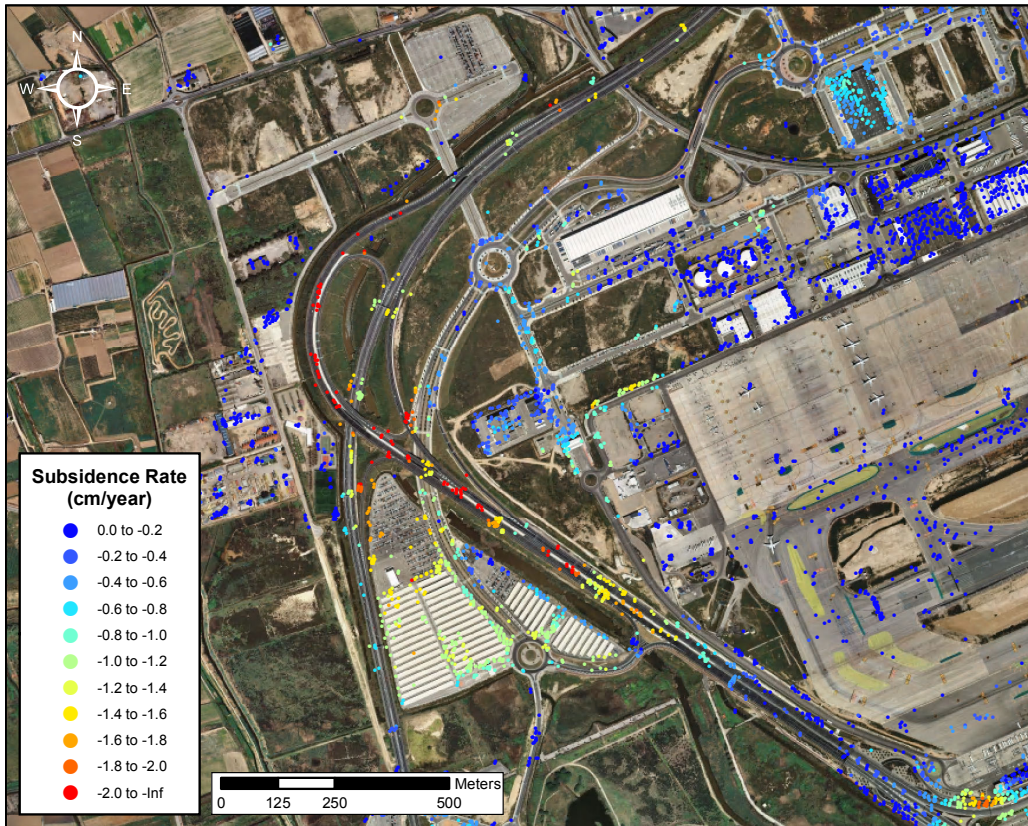
Figure A.9: Displacement rate results obtained using the ESM-MB optimization on the dA estimator over the Airport main access road.

A.0.2 Amplitude dispersion optimization results

This section present the high resolution motion maps over the additional AOIs. The dA threshold set is 0.25, which is equivalent to 15 degrees of phase standard deviation.

A.0.2.1 Barcelona-El Prat Airport access road

Fig. A.9 shows the motion results obtained in the airport main road access using the dA esimator over the ESM-MB optimized data-set. As ususal, the scale selected for this area is between 0 a 2 cm/year. The results presented in Fig. A.1 where rather poor in density, since the area under monitoring present high temporal decorrelation. As it may be observed, most of the area is surrounded by vegetation and cultivated fields.

In this case, measurement points are located mainly in the structures, specially the main
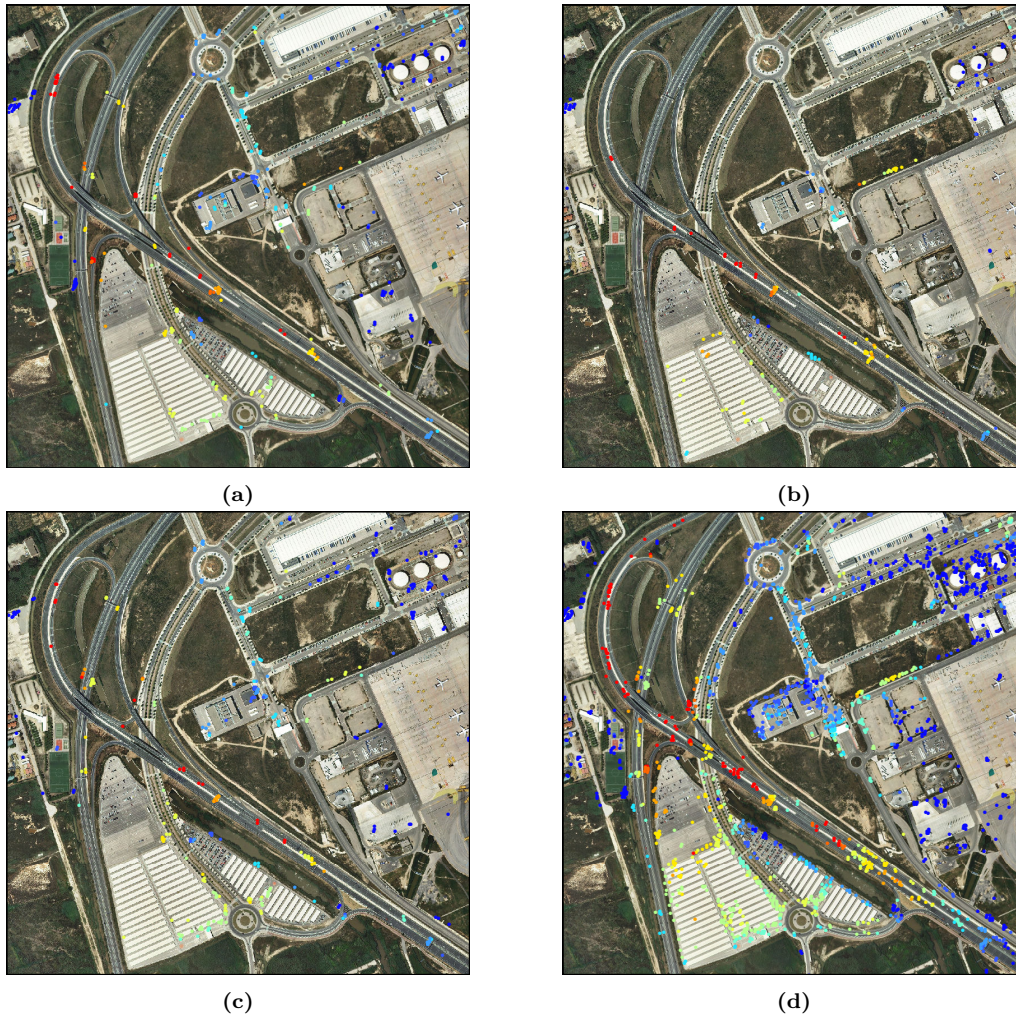
Figure A.10: Displacement rate results obtained using the dA estimator over the Airport access road: HH (a), HV (b), VH (c) and ESM-MB (d).

road. An increasing subsidence trend is observed from south to North, finding the values up to 2 cm/year on the curve in the western part. The parking area, specially in the parapets part, also contains several PSs presenting motion.

Looking at the comparison in Fig. A.10, the PSs density is is still rather poor. The analysis of the subsidence in the original channels results could be complicated, since the sparsity of the points do not allow for the identification of any spatially correlated phenomena. However, the higher density provided by the optimized results allows to characterize almost the totality of the road section with ease, identifying several areas with consistent displacement.
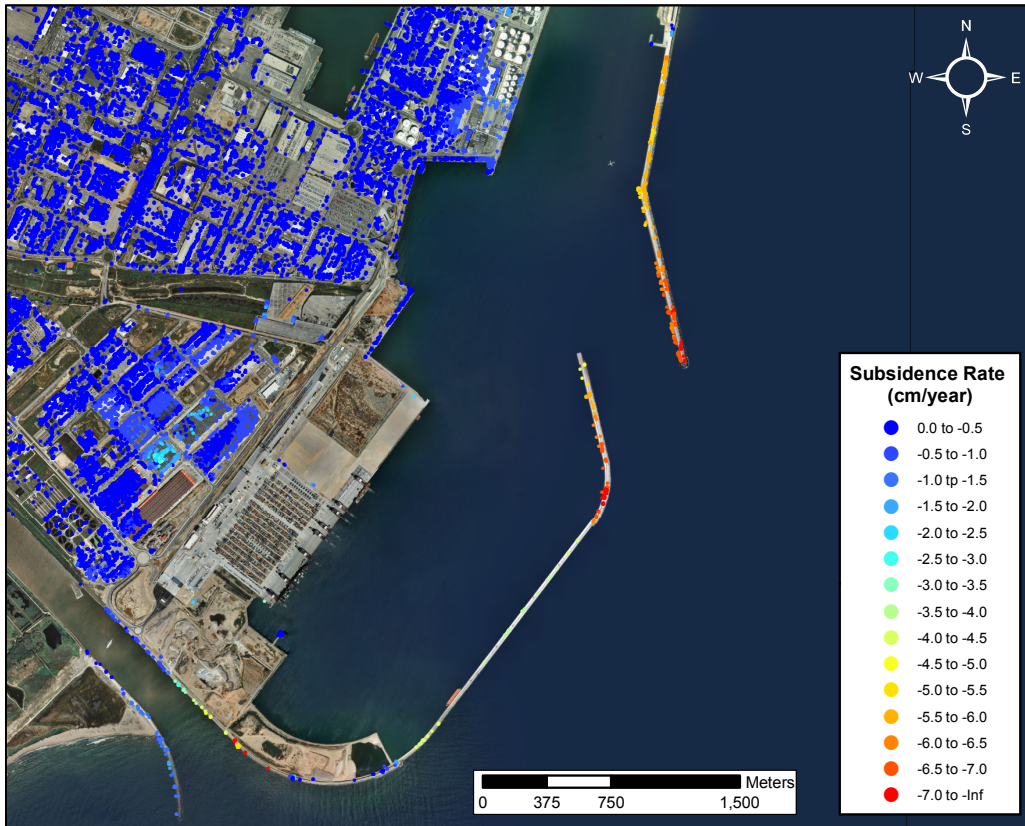
Figure A.11: Displacement rate results obtained using the ESM-MB optimization on the dA estimator over the harbor breakwaters.

A.0.2.2 Port de Barcelona

This section is devoted to present the subsidence results obtained in the harbor area using the dA estimator. As for the coherence stability, the breakwaters scale is between 0 and 7 cm/year. The Energy bay and the W Barcelona hotel are given in a scale between 0 and 1 cm/year.

The first area analyzed is the harbor breakwaters, presented in Fig. A.11. In comparison with the coherence stability results in Fig. A.3, the sampling along the breakwater structure is better but the characterization for the latter was already quite good. This is probably a coincidence, since the orientation of most of the structure matches the heading of the descending orbit used to acquire the PolSAR data-set. In this case, even if the structure is narrow, the good backscattering conditions allow for a good sampling even in the coherence stability case. The southern breakwater main linear structure has no points also for the dA estimator. This may be caused by either lack of sensitivity or by high non-linear motion patterns. The existing PS suggest an increase in potion towards

150

Figure A.12: Displacement rate results obtained using the dA estimator over the harbor breakwaters: HH (a), HV (b), VH (c) and ESM-MB (d).

the central part of the linear structure.

The maximum displacement rate detected for the dA results is above 7 cm/year, in the far end of the North breakwater and in the curve of the South breakwater. As in the coherence stability case, this results also perfectly agree with the ones obtained in [33].

Fig. A.12 presents the comparison between the original and the ESM-MB optimized results. As in the coherence stability case in Fig. A.4, the scarce sampling in the HH, VV and HV channels is clearly overcome in the optimized results, providing a good detection of the gradient along the breakwaters structure.
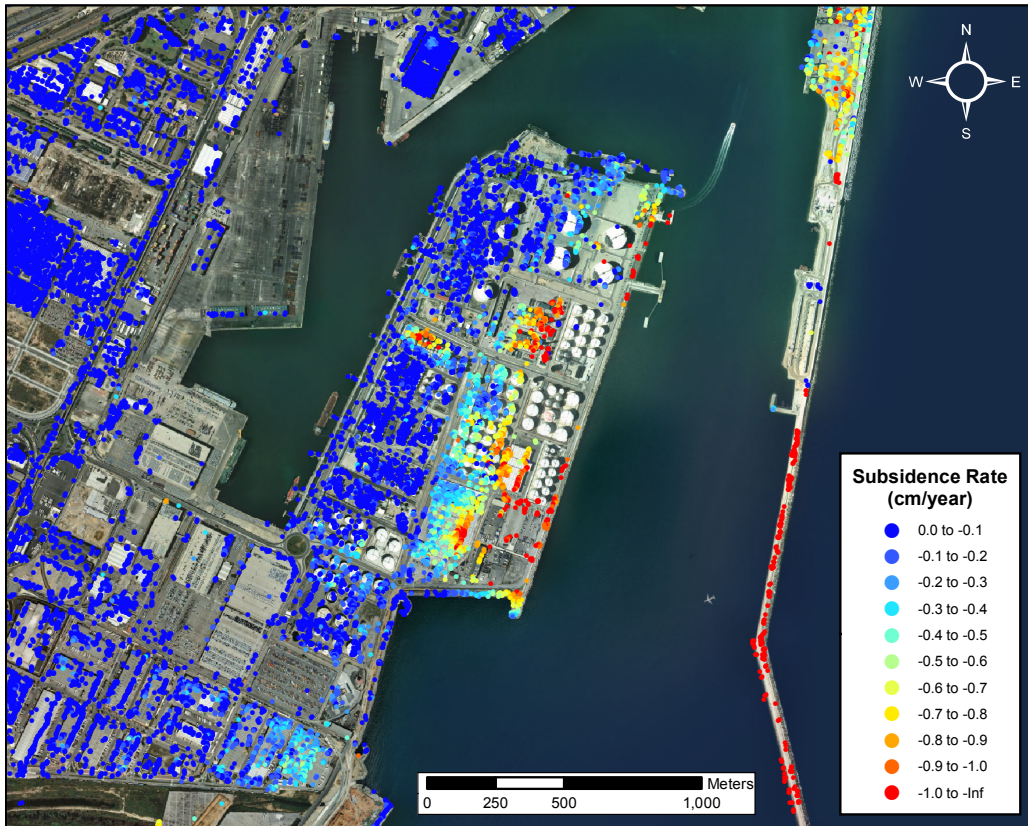
Figure A.13: Displacement rate results obtained using the ESM-MB optimization on the dA estimator over the harbor Energy bay.

Fig. A.13 displays the results over the harbor Energy bay using the ESM-MB opitimized data-set with the dA estimator. The PSs density was already high using the coherence stability estimator. The enhancement provided by the dA estimator in this case is in terms of resolution. For instance, notice the small isolated subsidence area located at the middle west part of the bay. This phenomenon was characterized by only two measurement points for the coherence stability estimator. Meanwhile, the dA estimator provides enough information to perfectly identify and localize the area affected, giving enough samples to characterize the displacement gradient.

Several small focuses are detected, mostly located at the east portion of the bay, save from the small focus already mentioned in the previous paragraph. The maximum displacement rate detected is around 1 cm/year. The motion detected suggests a general tilt of the area from West to East.

Fig. A.14 shows the comparison of results of the original channels with the ESM-MB optmized ones. A denser coverage of measurement points is observes, which eases the detection and analysis of the aforementioned subsidence areas on the Energy bay. For

Figure A.14: Displacement rate results obtained using the dA estimator over the harbor Energy bay: HH (a), HV (b), VH (c) and ESM-MB (d).

instance, the small focus located at the western part is hard to detect in any of the original channels results.

The last section analyzed in the harbor premises is the location of W Barcelona hotel. Fig. A.15 present the results using the ESM-MB optimized results using the dA estimator. This AOI covers the actual location of the hotel as well as the short breakwater attached to this area. The main subsidence detected is around the hotel building, presenting maximum displacement rate values around 1 cm/year. The breakwater presents PSs coverage in the widest part, characterized by a motion gradient towards the tip with displacement rates less than 8 mm/year.
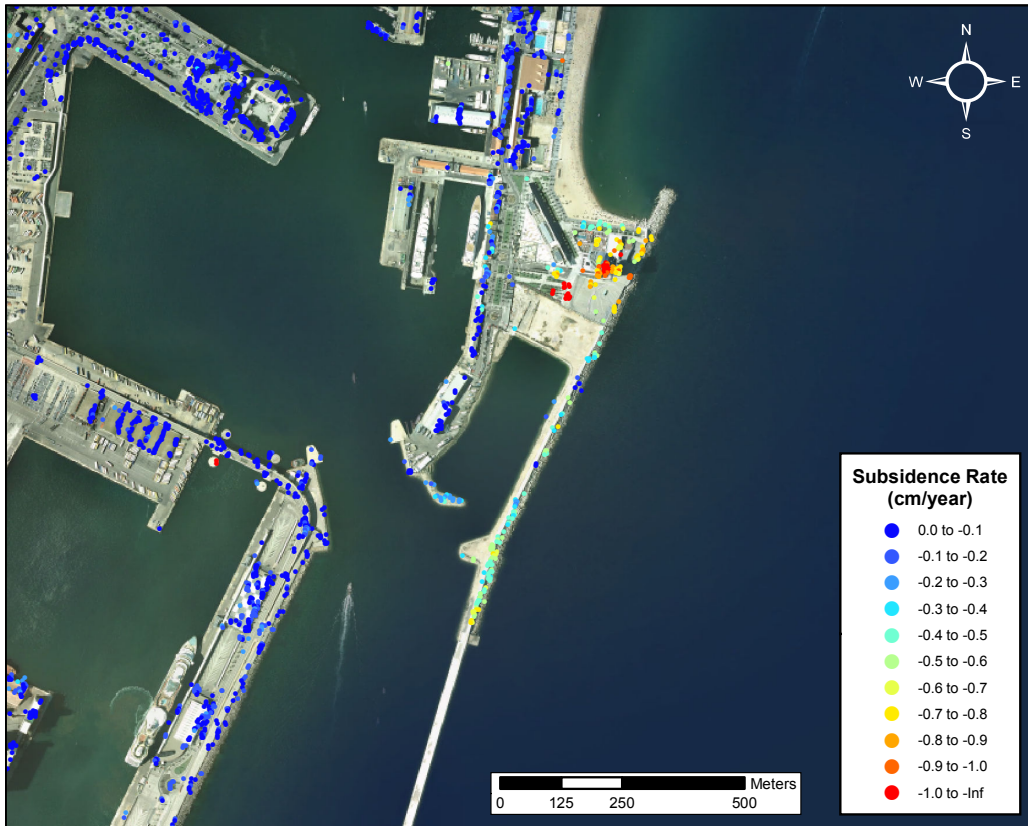
Figure A.15: Displacement rate results obtained using the ESM-MB optimization on the dA estimator over Hotel Vela.

Fig. A.16 shows the comparison of the original channels results with the optimized ones. In this case, the initial density of PSs using the original channels is rather poor. The optimized results are not spectacular either, but notice how the main structures are well characterized. For instance, notice the interior breakwater, which presents general stability, presents a decent density of measurement points all along its structure.
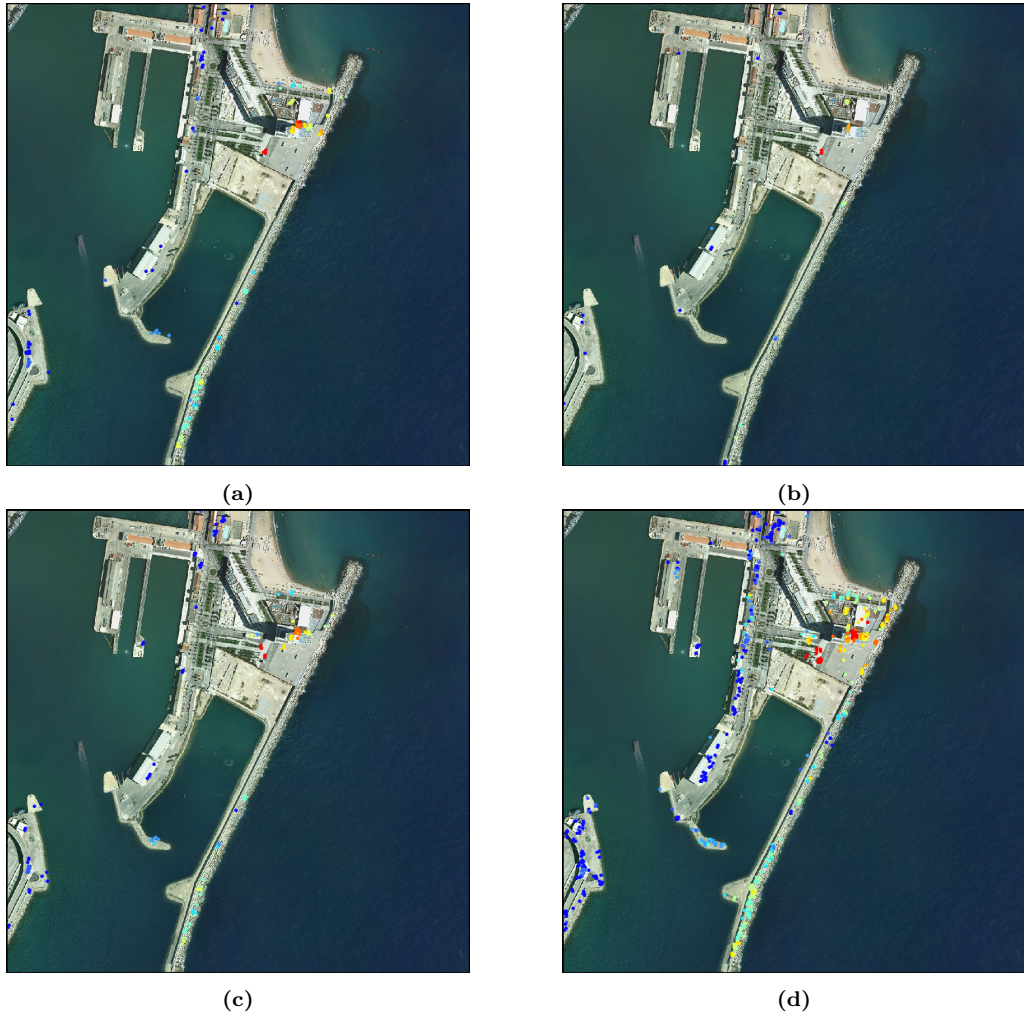
Figure A.16: Displacement rate results obtained using the dA estimator over Hotel Vela: HH (a), HV (b), VH (c) and ESM-MB (d).

Acronyms

RAR Real Aperture Radar

SAR Synthetic Aperture Radar

InSAR SAR Interferometry

DInSAR Differential SAR Interferometry

PolSAR Polarimetric SAR

PolDInSAR Polarimetric Differential SAR Interferometry

PS Persistent Scatterers

PSC Persistent Scatterers Candidates

PSI Persistent Scatterers Interferometry

SLC Single Look Complex

DEM Digital Elevation Model

LOS Line of Sight

ECEF Earth Centered Earth Fixed

UTM Universal Transverse Mercator

SNR Signal to Noise Ratio

CPT Coherent Pixel Technique

CSA Canadian Space Agency

LEO Low Earth Orbit

WGS-84 World Geodetic System 84

AOI Area Of Interest

SRTM Shuttle Radar Topographic Mission

TSC Temporal Sublook Coherence

dA Amplitude Dispersion

PRF Pulse Repetition Frequency

MAF Model Adjustment Function

LMC Linear Model Coherence

CGM Conjugate Gradient Method

SVD Singular Value Decomposition

APS Atmospheric Phase Screen

SLP Spatial Low-Pass

SHP Spatial High-Pass

TLP Temporal Low-Pass

THP Temporal High-Pass

DSM Different Scattering Mechanism

ESM Equal Scattering Mechanism

ESM-MB Multi-Baseline Equal Scattering Mechanism

SOM Sub-optimum Scattering Mechanism

SOM-MB Multi-Baseline Sub-optimum Scattering Mechanism

LIST OF FIGURES

List of Tables

Bibliography

[1] L. C. Graham, "Synthetic interferometer radar for topographic mapping," *Proceedings of the IEEE*, vol. 62, no. 6, pp. 763–768, 1974. (Cited on page 2.)

[2] H. A. Zebker and R. M. Goldstein, "Topographic mapping from interferometric synthetic aperture radar observations," *Journal of Geophysical Research: Solid Earth*, vol. 91, no. B5, pp. 4993–4999, 1986. (Cited on page 2.)

[3] T. G. Farr, P. A. Rosen, E. Caro, R. Crippen, R. Duren, S. Hensley, M. Kobrick, M. Paller, E. Rodriguez, L. Roth, D. Seal, S. Shaffer, J. Shimada, J. Umland, M. Werner, M. Oskin, D. Burbank, and D. Alsdorf, "The Shuttle Radar Topography Mission," *Reviews of Geophysics*, vol. 45, no. 2, pp. 1–33, may 2007. (Cited on page 2.)

[4] C. Rossi and M. Eineder, "TanDEM-X mission: raw DEM generation," in *Proc. 8th European Conference on Synthetic Aperture Radar (EUSAR'10)*, Aachen (Germany), 2010. (Cited on page 2.)

[5] J. C. Curlander and R. N. McDonough, *Synthetic aperture radar : Systems and Signal Processing.* New York: John Wiley & Sons, 1991. (Cited on pages 9 and 13.)

[6] I. G. Cumming and F. H.-C. Wong, *Digital Signal Processing of Synthetic Aperture Radar Data: Algorithms and Implementation.* Artech House, 2005. [Online]. Available: http://books.google.es/books/about/Digital{_}Signal{_}Processing{_}of{_}}Synthetic{_}A.html?id=e9xxQgAACAAJ{&}pgis=1 (Cited on page 10.)

[7] A. Cardama, L. Jofre, J. M. Rius and J. Romeu, *Antenas.* Edicions UPC, 1993. [Online]. Available: http://books.google.es/books/about/Antenas.html?hl=es{&}id=AlQ8p2C4sCoC{&}pgis=1 (Cited on page 11.)

[8] J. Curlander, "Interferometric synthetic aperture radar for terrain mapping," in *1995 International Conference on Acoustics, Speech, and Signal Processing*, vol. 5. IEEE, 1995, pp. 2801–2804. [Online]. Available: http://ieeexplore.ieee.org/lpdocs/epic03/wrapper.htm?arnumber=479427 (Cited on page 15.)

[9] D. Carrasco Díaz, "SAR Interferometry for digital elevation model generation and differential applications," Ph.D. dissertation, Universitat Politecnica de Catalunya, 1998. (Cited on pages 19 and 20.)

[10] R. M. Goldstein, H. A. Zebker, and C. L. Werner, "Satellite radar interferometry: Two-dimensional phase unwrapping," *Radio Science*, vol. 23, no. 4, pp. 713–720, 1988. (Cited on page 20.)

[11] D. C. Ghiglia and L. A. Romero, "Robust two-dimensional weighted and unweighted phase unwrapping that uses fast transforms and iterative methods," *Journal of the Optical Society of America A*, vol. 11, no. 1, pp. 107–117, 1994. (Cited on page 20.)

[12] U. Spagnolini, "2-D phase unwrapping and instantaneous frequency estimation," *IEEE Transactions on Geoscience and Remote Sensing*, vol. 33, no. 3, pp. 579–589, may 1995. (Cited on page 20.)

[13] G. Fornaro, G. Franceschetti, and R. Lanari, "Interferometric SAR phase unwrapping using Green's formulation," *IEEE Transactions on Geoscience and Remote Sensing*, vol. 34, no. 3, pp. 720–727, may 1996. (Cited on page 20.)

[14] A. Reigber and J. Moreira, "Phase unwrapping by fusion of local and global methods," in *Proc. IEEE International Geoscience and Remote Sensing Symposium (IGARSS'97)*, Singapore (Singapore), 1997. (Cited on page 20.)

[15] M. Costantini, "A novel phase unwrapping method based on network programming," *IEEE Transactions on Geoscience and Remote Sensing*, vol. 36, no. 3, pp. 813–821, may 1998. (Cited on page 20.)

[16] I. G. Cumming, "A region-growing algorithm for InSAR phase unwrapping," *IEEE Transactions on Geoscience and Remote Sensing*, vol. 37, no. 1, pp. 124–134, 1999. (Cited on page 20.)

[17] C. W. Chen and H. A. Zebker, "Two-dimensional phase unwrapping with use of statistical models for cost functions in nonlinear optimization," *Journal of the Optical Society of America A*, vol. 18, no. 2, pp. 338–351, 2001. (Cited on page 22.)

[18] R. Hanssen, *Radar Interferometry: Data Interpretation and Error Analysis*. Kluwer Academic Publishers, 2001. (Cited on pages 25, 26, 38, and 39.)

[19] R. Touzi, A. Lopes, J. Bruniquel, and P. W. Vachon, "Coherence estimation for SAR imagery," *IEEE Transactions on Geoscience and Remote Sensing*, vol. 37, no. 1, pp. 135–149, 1999. (Cited on page 25.)

[20] M. Seymour and I. Cumming, "Maximum likelihood estimation for SAR interferometry," in *Proceedings of IGARSS '94 - 1994 IEEE International Geoscience*

and Remote Sensing Symposium, vol. 4. IEEE, 1994, pp. 2272–2275. [Online]. Available: http://ieeexplore.ieee.org/lpdocs/epic03/wrapper.htm?arnumber=399711 (Cited on page 25.)

[21] F. Gatelli, A. Guamieri, F. Parizzi, P. Pasquali, C. Prati, and F. Rocca, "The wavenumber shift in SAR inferometry," *IEEE Transactions on Geoscience and Remote Sensing*, vol. 32, no. 4, pp. 855–865, jul 1994. [Online]. Available: http://ieeexplore.ieee.org/xpls/abs{_}all.jsp?arnumber=298013http://ieeexplore.ieee.org/lpdocs/epic03/wrapper.htm?arnumber=298013 (Cited on page 26.)

[22] E. Sansosti, P. Berardino, M. Manunta, F. Serafino, and G. Fornaro, "Geometrical SAR image registration," *IEEE Transactions on Geoscience and Remote Sensing*, vol. 44, no. 10, pp. 2861–2870, oct 2006. [Online]. Available: http://ieeexplore.ieee.org/lpdocs/epic03/wrapper.htm?arnumber=1704979 (Cited on page 28.)

[23] B. Delaunay, "Sur la sphère vide," *Bulletin of Academy of Sciences of the USSR*, no. 6, pp. 793 – 800, 1934. (Cited on pages 29 and 34.)

[24] P. Blanco-Sánchez, "SAR Differential Interferometry for deformation monitoring under a multi-frequency approach," Ph.D. dissertation, Universitat Poltecnica de Catalunya, 2009. (Cited on page 29.)

[25] O. Mora, J. Mallorqui, and A. Broquetas, "Linear and nonlinear terrain deformation maps from a reduced set of interferometric SAR images," *IEEE Transactions on Geoscience and Remote Sensing*, vol. 41, no. 10, pp. 2243–2253, oct 2003. [Online]. Available: http://ieeexplore.ieee.org/lpdocs/epic03/wrapper.htm?arnumber=1237386 (Cited on pages 29, 31, and 34.)

[26] P. Blanco-Sánchez, J. J. Mallorquí, S. Duque, and D. Monells, "The Coherent Pixels Technique (CPT): An Advanced DInSAR Technique for Nonlinear Deformation Monitoring," *Pure and Applied Geophysics*, vol. 165, no. 6, pp. 1167–1193, aug 2008. [Online]. Available: http://link.springer.com/10.1007/s00024-008-0352-6 (Cited on pages 29 and 34.)

[27] A. Ferretti, C. Prati, and F. Rocca, "Permanent Scatterers in SAR interferometry," *IEEE Transactions on Geoscience and Remote Sensing*, vol. 39, no. 1, pp. 8–20, 2001. (Cited on pages 31 and 32.)

[28] R. Iglesias, J. J. Mallorqui, and P. Lopez-Dekker, "DInSAR Pixel Selection Based on Sublook Spectral Correlation Along Time," *IEEE Transactions on Geoscience and Remote Sensing*, vol. 52, no. 7, pp. 3788–3799, jul 2014. [Online]. Available: http://ieeexplore.ieee.org/lpdocs/epic03/wrapper.htm?arnumber=6620942 (Cited on pages 32 and 33.)

[29] M. Hestenes and E. Stiefel, "Methods of Conjugate Gradients for Solving Linear Systems," *Journal of Research of the National Bureau of Standards*, vol. 49, no. 6, pp. 409 – 436, 1952. (Cited on pages 36, 37, and 91.)

[30] O. Alter, P. O. Brown, and D. Botstein, "Singular value decomposition for genome-wide expression data processing and modeling," *Proceedings of the National Academy of Sciences*, vol. 97, no. 18, 2000. (Cited on page 40.)

[31] Y. Yamaguchi, T. Moriyama, M. Ishido, and H. Yamada, "Four-component scattering model for polarimetric SAR image decomposition," *IEEE Transactions on Geoscience and Remote Sensing*, vol. 43, no. 8, pp. 1699–1706, aug 2005. [Online]. Available: http://ieeexplore.ieee.org/stamp/stamp.jsp?tp=&arnumber=1487628&isnumber=32001 (Cited on pages 45 and 63.)

[32] S. Cloude and K. Papathanassiou, "Polarimetric SAR interferometry," *IEEE Transactions on Geoscience and Remote Sensing*, vol. 36, no. 5, pp. 1551–1565, 1998. [Online]. Available: http://ieeexplore.ieee.org/lpdocs/epic03/wrapper.htm?arnumber=718859 (Cited on pages 46, 89, and 93.)

[33] F. Pros, S. Gonzalez-Lopez, J. J. Martinez-Benjamin, V. Palau, and J. Duro, "Breakwater settlement monitoring with InSAR data," in *2014 IEEE Geoscience and Remote Sensing Symposium.* IEEE, jul 2014, pp. 414–417. [Online]. Available: http://ieeexplore.ieee.org/lpdocs/epic03/wrapper.htm?arnumber=6946446 (Cited on pages 51, 143, and 151.)

[34] "Barcelona hit with heaviest snowfall in 25 years," 2010. [Online]. Available: http://www.telegraph.co.uk/news/worldnews/europe/spain/7401422/Barcelona-hit-with-heaviest-snowfall-in-25-years.html (Cited on pages 54 and 113.)

[35] L. Sagues, J. Lopez-Sanchez, J. Fortuny, X. Fabregas, A. Broquetas, and A. Sieber, "Indoor experiments on polarimetric SAR interferometry," *IEEE Transactions on Geoscience and Remote Sensing*, vol. 38, no. 2, pp. 671–684, mar 2000. [Online]. Available: http://ieeexplore.ieee.org/lpdocs/epic03/wrapper.htm?arnumber=841997 (Cited on pages 88 and 91.)

[36] E. Colin, C. Titin-Schnaider, and W. Tabbara, "An interferometric coherence optimization method in radar polarimetry for high-resolution imagery," *IEEE Transactions on Geoscience and Remote Sensing*, vol. 44, no. 1, pp. 167–175, jan 2006. [Online]. Available: http://ieeexplore.ieee.org/lpdocs/epic03/wrapper.htm?arnumber=1564406 (Cited on pages 89, 90, 93, and 94.)

[37] G. Watson, "Computing the numerical radius," *Linear Algebra and its Applications*, vol. 234, pp. 163–172, feb 1996. [Online]. Available: http://www.sciencedirect.com/science/article/pii/0024379594000972http://linkinghub.elsevier.com/retrieve/pii/0024379594000972 (Cited on page 89.)

[38] V. D. Navarro-Sanchez, J. M. Lopez-Sanchez, and F. Vicente-Guijalba, "A Contribution of Polarimetry to Satellite Differential SAR Interferometry: Increasing the Number of Pixel Candidates," *IEEE Geoscience and Remote Sensing Letters*, vol. 7, no. 2, pp. 276–280, apr 2010. [Online]. Available: http://ieeexplore.ieee.org/lpdocs/epic03/wrapper.htm?arnumber=5299098 (Cited on pages 89, 92, and 136.)

[39] R. Iglesias, D. Monells, X. Fabregas, J. J. Mallorqui, A. Aguasca, and C. Lopez-Martinez, "Phase Quality Optimization in Polarimetric Differential SAR Interferometry," *IEEE Transactions on Geoscience and Remote Sensing*, vol. 52, no. 5, pp. 2875–2888, 2013. (Cited on page 89.)

[40] M. Neumann, L. Ferro-Famil, and A. Reigber, "Multibaseline Polarimetric SAR Interferometry Coherence Optimization," *IEEE Geoscience and Remote Sensing Letters*, vol. 5, no. 1, pp. 93–97, jan 2008. [Online]. Available: http://ieeexplore.ieee.org/xpls/abs{_}all.jsp?arnumber=4382931http://ieeexplore.ieee.org/lpdocs/epic03/wrapper.htm?arnumber=4382931 (Cited on page 90.)

[41] V. D. Navarro-Sanchez and J. M. Lopez-Sanchez, "Subsidence monitoring using polarimetric persistent scatterers interferometry," in *2011 IEEE International Geoscience and Remote Sensing Symposium*. IEEE, jul 2011, pp. 1083–1086. [Online]. Available: http://ieeexplore.ieee.org/lpdocs/epic03/wrapper.htm?arnumber=6049384 (Cited on pages 92 and 136.)

[42] ——, "Improvement of Persistent-Scatterer Interferometry Performance by Means of a Polarimetric Optimization," *IEEE Geoscience and Remote Sensing Letters*, vol. 9, no. 4, pp. 609–613, jul 2012. [Online]. Available: http://ieeexplore.ieee.org/lpdocs/epic03/wrapper.htm?arnumber=6119193 (Cited on pages 92 and 136.)

[43] J. Souyris, P. Imbo, R. Fjortoft, S. Mingot, and J.-s. Lee, "Compact polarimetry based on symmetry properties of geophysical media: the pi/4 mode," *IEEE Transactions on Geoscience and Remote Sensing*, vol. 43, no. 3, pp. 634–646, mar 2005. [Online]. Available: http://ieeexplore.ieee.org/stamp/stamp.jsp?tp=&arnumber=1396337&isnumber=30375 (Cited on page 137.)

LIST OF PUBLICATIONS

Journal Articles

[JA1] R. Iglesias, A. Aguasca, X. Fabregas, J. J. Mallorqui, D. Monells, C. López-Martínez, and L. Pipia, "Ground-Based Polarimetric SAR Interferometry for the Monitoring of Terrain Displacement Phenomena - Part I: Theoretical Description," *IEEE Journal of Selected Topics in Applied Earth Observations and Remote Sensing*, vol. 8, no. 3, pp. 980–993, Mar. 2015. (Not cited.)

[JA2] ——, "Ground-Based Polarimetric SAR Interferometry for the Monitoring of Terrain Displacement Phenomena - Part II: Applications," *IEEE Journal of Selected Topics in Applied Earth Observations and Remote Sensing*, vol. 8, no. 3, pp. 994–1007, Mar. 2015. (Not cited.)

[JA3] R. Iglesias, D. Monells, C. López-Martínez, J. J. Mallorqui, X. Fabregas, and A. Aguasca, "Polarimetric Optimization of Temporal Sublook Coherence for DInSAR Applications," *IEEE Geoscience and Remote Sensing Letters*, vol. 12, no. 1, pp. 87–91, Jan. 2015. (Not cited.)

[JA4] R. Iglesias, J. J. Mallorqui, D. Monells, C. López-Martínez, X. Fabregas, A. Aguasca, J. A. Gili, and J. Corominas, "PSI Deformation Map Retrieval by Means of Temporal Sublook Coherence on Reduced Sets of SAR Images," *Remote Sensing*, vol. 7, no. 1, pp. 530–563, Jan. 2015. (Not cited.)

[JA5] R. Iglesias, D. Monells, X. Fabregas, J. J. Mallorqui, A. Aguasca, and C. López-Martínez, "Phase Quality Optimization in Polarimetric Differential SAR Interferometry," *IEEE Transactions on Geoscience and Remote Sensing*, vol. 52, no. 5, pp. 2875–2888, May 2014. (Not cited.)

[JA6] D. Di Martire, R. Iglesias, D. Monells, G. Centolanza, S. Sica, M. Ramondini, L. Pagano, J. J. Mallorqui, and D. Calcaterra, "Comparison between Differential SAR interferometry and ground measurements data in the displacement moni-

toring of the earth-dam of Conza della Campania (Italy)," *Remote Sensing of Environment*, vol. 148, pp. 58–69, May 2014. (Not cited.)

[JA7] A. Yerro, J. Corominas, D. Monells, and J. J. Mallorqui, "Analysis of the evolution of ground movements in a low densely urban area by means of DInSAR technique," *Engineering Geology*, vol. 170, pp. 52–65, Feb. 2014. (Not cited.)

[JA8] P. Blanco, J. J. Mallorqui, S. Duque, and D. Monells, "The Coherent Pixels Technique (CPT): an Advanced DInSAR Technique for Non-linear Deformation Monitoring," *Pure and Applied Geophysics*, vol. 165, pp. 1167–1193, Jun. 2008. (Not cited.)

Conference Articles

[CA1] J. Duro, R. Iglesias, P. Blanco-Sánchez, D. Albiol, and F. Koudogbo, "PSI Wide Area Product (WAP) for measuring Ground Surface Displacements at regional level for multi-hazards studies," in *Proc. EGU General Assembly (EGU'15)*, Vienna (Austria), Apr. 2015. (Not cited.)

[CA2] J. Duro, R. Iglesias, P. Blanco-Sánchez, D. Albiol, T. Wright, N. Adam, F. Rodriguez-Gonzalez, R. Brcic, A. Parizzi, F. Novali, and P. Bally, "Strategies for Measuring Large Scale Ground Surface Deformations: PSI Wide Area Product Approaches," in *Proc. 9th International Workshop on Advances in the Science and Applications of SAR Interferometry (FRINGE'15)*, Frascati (Rome, Italy), Mar. 2015. (Not cited.)

[CA3] J. Duro, R. Iglesias, P. Blanco-Sánchez, and D. Albiol, "Improved PSI Performance for Landslide Monitoring Applications," in *9th International Workshop on Advances in the Science and Applications of SAR Interferometry (FRINGE'15)*, Frascati (Rome, Italy), Mar. 2015. (Not cited.)

[CA4] R. Iglesias, D. Monells, G. Centolanza, J. J. Mallorqui, X. Fabregas, and A. Aguasca, "Down-slope Combination of Orbital and Ground-Based DInSAR for the Efficient Monitoring of Slow-Moving Landslides," in *Proc. 10th European Conference on Synthetic Aperture Radar (EUSAR'14)*, Berlin (Germany), Jun. 2014. (Not cited.)

[CA5] D. Monells, R. Iglesias, G. Centolanza, and J. J. Mallorqui, "Iterative Solution to Temporal Phase Wrapping in Differential SAR Interferometry for High Displacement Rate Phenomena," in *Proc. 10th European Conference on Synthetic Aperture Radar (EUSAR'14)*, Berlin (Germany), Jun. 2014. (Not cited.)

[CA6] R. Iglesias, D. Monells, X. Fabregas, J. J. Mallorqui, A. Aguasca, and C. López-

Martínez, "Phase Quality Optimization Techniques and Limitation in Polarimetric Differential SAR Interferometry," in *Proc. 6th International Workshop on Science and Applications of SAR Polarimetry and Polarimetric Interferometry (POLInSAR'13)*, Frascati (Rome, Italy), Jan. 2013. (Not cited.)

[CA7] D. Monells, R. Iglesias, and J. J. Mallorqui, "Performance Comparison Between Dual Polarimetric and Fully Polarimetric Data for Differential SAR Interferometry Subsidence Monitoring," in *Proc. 6th International Workshop on Science and Applications of SAR Polarimetry and Polarimetric Interferometry (POLInSAR'13)*, Frascati (Rome, Italy), Jan. 2013. (Cited on page 114.)

[CA8] R. Iglesias, D. Monells, G. Centolanza, J. J. Mallorqui, X. Fabregas, and A. Aguasca, "Landslide Monitoring with Spotlight TerraSAR-X DATA," in *Proc. IEEE International Geoscience and Remote Sensing Symposium (IGARSS'12)*, Munich (Germany), Jul. 2012. (Not cited.)

[CA9] D. Monells, R. Iglesias, J. J. Mallorqui, X. Fabregas, and C. López-Martínez, "Phase quality Optimization in Orbital Differential SAR Interferometry with Fully Polarimetric Data," in *Proc. IEEE International Geoscience and Remote Sensing Symposium (IGARSS'12)*, Munich (Germany), Jul. 2012. (Not cited.)

[CA10] R. Iglesias, D. Monells, G. Centolanza, J. J. Mallorqui, X. Fabregas, A. Aguasca, and C. López-Martínez, "Application of High Resolution Spotlight TerraSAR-X Data to Landslide Monitoring," in *Proc. 9th European Conference on Synthetic Aperture Radar (EUSAR'12)*, Nuremberg (Germany), Apr. 2012. (Not cited.)

[CA11] G. Centolanza, R. Iglesias, D. Monells, and J. J. Mallorqui, "A New Approach to DInSAR Pixel Selection with a Combined Multi Resolution Selection Method," in *Proc. 9th European Conference on Synthetic Aperture Radar (EUSAR'12)*, Nuremberg (Germany), Apr. 2012. (Not cited.)

[CA12] R. Iglesias, D. Monells, G. Centolanza, J. J. Mallorqui, and P. López-Dekker, "A New Approach to DInSAR Pixel Selection with Spectral Correlation Along Time Between Sublooks," in *Proc. European Conference on Synthetic Aperture Radar (EUSAR'12)*, Nuremberg (Germany), Apr. 2012. (Not cited.)

[CA13] R. Iglesias, D. Monells, G. Centolanza, and J. J. Mallorqui, "DInSAR Pixel Selection Based on Spectral Correlation Along Time Between Sublooks," in *Proc. 7th International Workshop on Advances in the Science and Applications of SAR Interferometry (FRINGE'11)*, Frascati (Rome, Italy), Sep. 2011. (Not cited.)

[CA14] G. Centolanza, R. Iglesias, D. Monells, and J. J. Mallorqui, "A New Approach in DInSAR Pixel Selection with a Combined Multi Resolution Selection Method," in *Proc. 7th International Workshop on Advances in the Science and Applications of SAR Interferometry (FRINGE'11)*, Frascati (Rome, Italy), Sep. 2011. (Not cited.)

CONFERENCE ARTICLES

[CA15] J. J. Mallorqui, A. Aguasca, A. Broquetas, X. Fabregas, C. López-Martínez, A. Alonso-Gonzalez, G. Centolanza, R. Iglesias, and D. Monells, "Differential SAR Interferometry with Orbital, Airborne and Ground-Based Sensors," in *Proc. SAR Technologies and Applications Congress*, Madrid (Spain), May 2011. (Not cited.)

[CA16] P. Blanco, S. Duque, J. J. Mallorqui, and D. Monells, "Optimizing interferogram generation, pixel selection and data processing for high non-linear deformation monitoring with Orbital DInSAR," in *Proc. IEEE International Geoscience and Remote Sensing Symposium (IGARSS-07)*, Barcelona (Spain), Jul. 2007, pp. 1163–1166. (Not cited.)

[CA17] ——, "Analysis of highly non-linear deformations due to mining activity with Din-SAR: PSIC4 test-site," in *Proc. ENVISAT Symposium 2007 (CD-ROM)*, Montreux (Switzerland), Apr. 2007. (Not cited.)

[CA18] ——, "Optimal data generation for Multiple Images DInSAR techniques: Minimum Cost Flow interferograms and Region Growing pixel selection," in *Proc. FRINGE 2007 (CD-ROM)*, Frascatti (Italy), Apr. 2007. (Not cited.)

[CA19] S. Duque, J. J. Mallorqui, P. Blanco, and D. Monells, "Application of the Coherent Pixels Technique (CPT) to urban monitoring," in *Proc. URBAN 2007 (CD-ROM)*, Paris (France), Apr. 2007. (Not cited.)